TOWARDS HIGH BEAM BRIGHTNESS FROM PHOTOCATHODES

A Dissertation

Presented to the Faculty of the Graduate School

of Cornell University

in Partial Fulfillment of the Requirements for the Degree of

Doctor of Philosophy

by

Christopher Morrison Pierce

December 2022

TOWARDS HIGH BEAM BRIGHTNESS FROM PHOTOCATHODES

Christopher Morrison Pierce, Ph.D.

Cornell University 2022

Bright electron beams, as well as the technologies they power, are among the most powerful probes of matter at atomic length and time scales. Many of these systems and techniques, however, are limited in performance by the achievable brightness of modern particle accelerators. This thesis first investigates the factors that limit the final brightness of electron beams. These results suggest that research into better photocathode technologies is a viable path toward improving brightness in contemporary accelerator systems. The remainder of this thesis is dedicated to exploring a diverse set of ideas on how to improve the quality of photocathodes. First, brightness from Cs-Te (a common semiconductor photocathode) is measured near the photoemission threshold. Tuning the photon energy of the driving laser close to the threshold is expected to limit the energy imparted to the emitted electrons and improve the beam's initial brightness. Instead, it is revealed that low workfunction impurities likely present in cathodes of this type may be a barrier to high brightness. Next, we investigate a novel method of emitting electrons from unoccupied states with low transverse momentum. Electrons are first excited within a semiconductor and then ejected in a pump-prove style experiment. By adding a delay between the two processes, the electrons may relax and lose energy which may result in better brightness. Finally, the fabrication of nanoscale patterns on the surface of metal cathodes is investigated as a way to improve their nonlinear yield and source size. Future directions in research on the brightness of electron sources are discussed.

BIOGRAPHICAL SKETCH

Christopher Pierce grew up along the 18-mile stretch of land that is New Hampshire's seacoast. After high school, he attended Worcester Polytechnic Institute to study physics. There, he took his first steps into research. Chris investigated methods of improving numerical partial differential equation solvers with a specific focus on high-accuracy solutions of the Schrödinger equation. He obtained his Bachelor of Science degree in the spring of 2017

After college, Chris began graduate school in the department of physics at Cornell University. There, he fell in love with experimental physics and began his work on particle accelerators and photocathode materials. In 2021, he moved across the country to perform research at Lawrence Berkeley National Lab. This work involved studying the properties of nanopatterned metal photocathodes. At the end of the year, he returned to Cornell to finish his doctoral research. He obtained his Ph.D. from Cornell in the fall of 2022.

To my parents, for their love and support.

ACKNOWLEDGEMENTS

Before beginning this thesis I would like to take the time to acknowledge everyone that has helped me along my academic journey. I will begin with my parents for instilling a love of science in me when I was younger and whose support and encouragement have enabled me to take it this far. My partner, friends, family, and cat all deserve recognition for keeping me sane through the completion of this work.

I would like to thank my advisors at Cornell, Ivan Bazarov and Jared Maxson, for their mentorship and guidance throughout my Ph.D. I would not have been able to complete this thesis without them. Thank you to Colwyn Gulliford, Adam Bartnik, and Tobey Moore for teaching me about the practical side of science as well as how to have some fun in the lab. To my labmates, William Li, Jai Kwan Bae, and Cameron Duncan, thank you for your support and our shared time together. I will always have fond memories of foosball and Mario Kart at the conferences we went to together. I would like to thank everyone who I have worked with during my research at Cornell for their assistance. There are too many to name here.

Moving across the country to work in a new state during the pandemic was quite a challenge and I had a lot of help to make this happen. I would like to express my gratitude to Daniele Filippetto for being my mentor at Lawrence Berkeley Lab (LBL) and supporting my research while I was there. Thank you to everyone that I interacted with at LBL in the course of my work there: Dan Durham, Eric Cropp, Fabrizio Riminucci, Howard Padmore, the Molecular Foundry staff, and BELLA laser support staff among others.

Lastly, I would like to acknowledge US NSF Award PHY-1549132, the Center for Bright Beams and the US DOE SCGSR program for funding this work.

CONTENTS

LIST OF TABLES

LIST OF FIGURES

CHAPTER 1

INTRODUCTION

Electron beams have become an essential tool for those seeking to study nature at the scale of the atom. At the energies achievable in electron microscopes and university scale diffraction apparatus (~100 keV), the electron's de Broglie wavelength is only 3.7 pm. Being small compared to the distance between atoms in solid state systems (~100 pm), this value suggests the utility of using electrons as a direct probe of matter. Electron beams also play an important indirect role in the study of atomic-scale systems due to their use in the production of intense x-ray radiation. The synchrotrons and free electron lasers of the world are powered by these beams and the radiation they generate forms an important complementary tool to electron beams.

In this thesis, we seek to improve the performance of this broad family of techniques by increasing the quality of the electron beams that power them. Before we begin, however, we must settle on a suitable definition of "quality" in this context.

1.1 The Brightness of Charged Particle Beams

To simplify our work in forming a metric of quality on particle beams, let's consider only a single spatial dimension in the transverse plane of the beam. We will call this direction x and it will turn out that this simple system has all of the essential features needed to define quality in the full three dimensions. Quality should be a property of the beam itself and not depend on its environment.

Since we would like to imagine this metric as describing a fundamental limit on where the electron beam may be used, it should also be difficult to improve the quality of the beam by conventional means. This motivates us to begin by considering quantities that are conserved during beam transport in a particle accelerator.

Two quantities that are conserved during transport are the occupied area, and density of the beam in phase-space[1] (x, $\tilde{p}_x$); termed emittance and (microscopic) brightness respectively. If we approximate the particles in the beam as non-interacting, then we can talk about the system as an ensemble in 2D phase-space (see example in Fig. 1.1). For the trajectories of particles during transport in an accelerator, Liouville's theorem guarantees these two metrics are conserved [136]. This satisfies our original goal for a definition of quality. However, we are left wondering how to quantitatively talk about the area of a beam which is described by a continuous density function in two dimensions: $\rho(x, \tilde{p}_x)$. In particular, many analytical distributions that describe particle beams (such as the normal distribution) have a non-zero density over all of phase-space, but we do not wish to say that they occupy an infinite area.

A solution to this problem is to consider an RMS, statistical definition of emittance [81]. Once normalized, the beam's density, $\rho(x, \tilde{p}_x)$, can be considered as a probability distribution function describing the statistics of two random variables: the phase-space coordinates x and $\tilde{p}_x$. The first two central moments of this distribution are the mean,

$$\vec{\mu} = [E[x], E[\tilde{p}_x]]\,, \tag{1.1}$$

[1]For the sake of convenience, momentum here is unitless and is equal to the relativistic momentum divided by the electron's mass and the speed of light. To avoid confusion we note this as $\tilde{p}_x = p_x/(m_e c)$ with $p_x = m_e c\beta_x\gamma$.

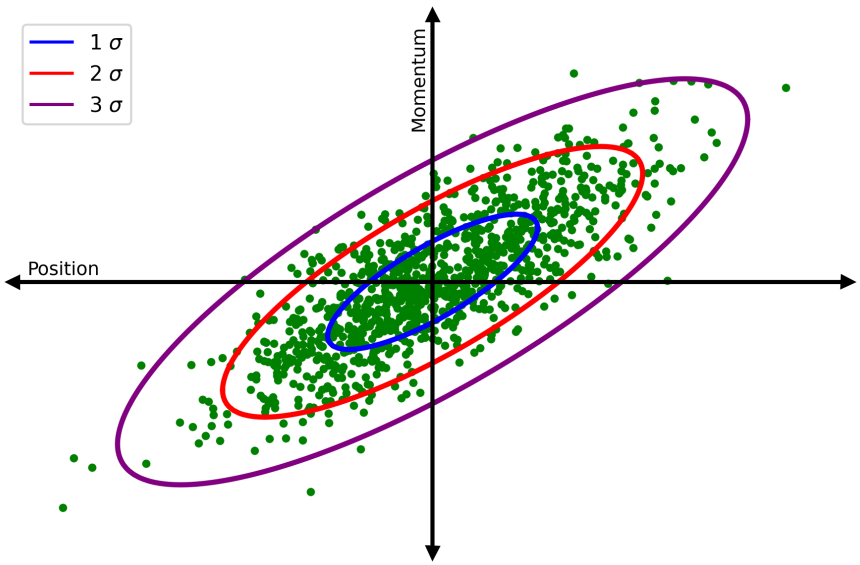

Figure 1.1: A sample of electrons (green dots) in transverse phase-space with the distribution's covariance shown as colored ellipses. The emittance of the beam corresponds to the area occupied by the ellipse labeled "1 σ".

and the variance-covariance matrix,

$$\hat{\Sigma} = \begin{bmatrix} E[x \cdot x] & E[x \cdot \tilde{p}_x] \\ E[\tilde{p}_x \cdot x] & E[\tilde{p}_x \cdot \tilde{p}_x] \end{bmatrix} - \vec{\mu}^T \cdot \vec{\mu}, \tag{1.2}$$

where $E[\xi]$ is the expectation value of the quantity ξ. Ignoring the remaining higher moments, we can show that the determinant of $\hat{\Sigma}$ (written as $|\hat{\Sigma}|$) is related to an area occupied by the now normally distributed phase-space variables.

In particular, the curves of equal probability density for the 2D normal distribution are ellipses (see Fig. 1.1). The ellipse such that the density is equal to e^{-1} of its peak value has squared axis lengths equal to the eigenvalues of $\hat{\Sigma}$. Since the determinant of a matrix is equal to the product of its eigenvalues, $\sqrt{|\hat{\Sigma}|}$ represents, up to a scaling factor, the area of that ellipse. There are different conventions for the scaling used in emittance. However, for simplicity, we take it as one. Therefore, we may define emittance[2] as $\varepsilon_{\text{RMS}} = \sqrt{|\hat{\Sigma}|} =$

[2]Technically, this is a "normalized" emittance. It is conventional for accelerator problems to

$\sqrt{E[x^2] \cdot E[\tilde{p}_x^2] - E[x \cdot \tilde{p}_x]^2}$.

Average brightness also follows from this definition as the total charge in the beam divided by the phase-space area. However, when calculating transverse brightness it is conventional to use an area in the 4D phase-space describing the whole transverse plane of the beam. Fortunately, our RMS emittance definition naturally generalizes to higher dimensions by evaluating the 4×4 matrix $\hat{\Sigma}$ on all of the phase-space dimensions and taking the square root of its determinant. When the x and y planes of the beam are not correlated, we can also write separate emittance for each direction and the full 4D area is equal to the product $\varepsilon_{4D} = \varepsilon_x \cdot \varepsilon_y$. The beam's brightness is then: $B = \frac{Q}{\varepsilon_x \varepsilon_y}$. It is this brightness that is commonly pointed to as a metric of quality useful for the applications of electron beams.

Before discussing how high-brightness beams are generated, one quick aside is that while the RMS definition of emittance is simple and easy to use, it is no longer a conserved quantity in all cases. For linear transport, we are fine[3] because when an initial phase-space point $\vec{r}_i = [x_i, \tilde{p}_{x,i}]$ is transformed to a final position $\vec{r}_f = \hat{M} \cdot \vec{r}_i$, the matrix $\hat{M}$ must be symplectic due to the equations of motion and it will have unit determinant. The squared final emittance is then $|\hat{\Sigma}_f| = |\hat{M} \cdot \hat{\Sigma}_i \cdot \hat{M}^T| = |\hat{\Sigma}_i|$. This is true for any number of dimensions. However, nonlinearities in the beam may distort phase-space and increase the area as evaluated by the second moments. Similarly, it may be possible to improve the beam's quality by "undoing" nonlinearities with magnetic elements in an

define the momentum variable as an angle $\theta = \tilde{p}_x/\tilde{p}_z$ ($\tilde{p}_z$ pointed down the accelerator) and write the emittance in these variables instead. However, this is less convenient for work on electron sources where $\tilde{p}_z$ changes greatly during the beam's evolution.

[3]This isn't completely true when magnetic fields are present as the conjugate momenta in this system will differ from the mechanical momenta by the magnetic vector potential. However, comparing emittances far away from magnetic elements is still fine.

accelerator.

These issues with the RMS brightness metric may be solved with other proposed measures of beam quality. Core brightness is the phase-space density at the beam's centroid and should not change in circularly symmetric systems [14]. Differential entropy (or continuous entropy) is $h = E[-\log(\delta A \cdot \rho(x, \tilde{p}_x)/Q)]$, where δA represents a small "reference area" and removes units from the inside of the logarithm [82]. Its value is chosen for convenience in the same way that measuring signal amplitude with decibels requires the selection of a reference level. This arbitrariness may be avoided by instead defining an "entropic emittance" [77] as $\varepsilon = \delta A \cdot \exp(h)$ that no longer depends on δA. The entropy is guaranteed to be conserved by all physical motion in the 2D/4D/6D phase-space, but may grow due to particle-particle interactions. Despite their potential utility in defining fundamental limits on the use of beams, calculating these metrics tends to be difficult and work is ongoing to simplify their use.

Now that we have a sense of what quality means for electron beams, we can proceed to investigate how bright beams are supplied in applications. Since brightness is, at least approximately, conserved in beam transport, our focus should be on the generation of electron beams, commonly achieved with photoemission.

1.2 Photocathodes as a "High Quality" Source of Electrons

Photoinjectors are a popular method of generating bright electron beams. Under vacuum, light is allowed to illuminate a small spot on the surface of a material called the photocathode (commonly a metal or semiconductor). Electrons

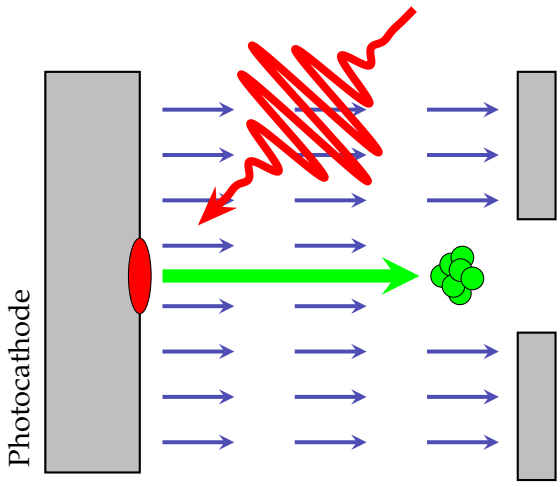

Figure 1.2: Diagram of a DC photoinjector. Light (red line) enters and hits the photocathode material to the left. Electrons (green circles) are ejected and accelerated out of a hole in the anode to the right by an electric field. The electric field here is represented as the force felt by the electrons (opposite of the field vector due to the electrons' negative charge) for clarity.

are ejected in this area due to the photoelectric effect. Once in vacuum, these electrons can be accelerated with a constant electric field (DC photoinjector) or the on-peak field of an RF cavity containing the photocathode (RF photoinjector). See Fig. 1.2 for a schematic of this process. We are highly motivated to understand how the properties of the cathode and photoinjector influence the brightness of the emitted beam.

First, we note that, for emission from uniform materials, the correlation term in the emittance vanishes at the cathode: $E[x \cdot \tilde{p}_x] = 0$. This allows us to separate the emittance into a product of the initial spot size and momentum spread. This gives us $\varepsilon = \sigma_x \cdot \sigma_{\tilde{p}_x}$. However, it is more typical to write the momentum spread as an energy. The "Mean Transverse Energy" (MTE) is defined as[4],

$$\text{MTE} = \frac{E[p_\perp^2]}{2m_e} = \frac{\sigma_{p_x}^2}{m_e} = m_e c^2 \sigma_{\tilde{p}_x}^2, \tag{1.3}$$

[4]We must be careful here to distinguish our normalized momentum from the actual momentum of the particles: $p_x = m_e c \tilde{p}_x$

where $p_\perp$ represents the momentum projected into the plane perpendicular to the direction of the beam and we have assumed that $\sigma_{\tilde{p}_x} = \sigma_{\tilde{p}_y}$. The emittance can now be written in terms of the MTE as $\varepsilon = \sigma_x \cdot \sqrt{\frac{\mathrm{MTE}}{mc^2}}$ [16].

For conventional photocathodes, the initial spot size (σ_x) is determined by the optics used to illuminate the material and is limited to something like 1 to 10 µm. The MTE, however, depends on several factors including photon energy of the illuminating source, the choice of cathode material, and the geometry of the cathode's surface. To better understand how these factors influence the emitted beam's MTE, we must first learn more about the physics of photoemission.

One of the dominant descriptions of photoemission is called the three-step model [19, 151]. As advertised, the photoemission process is split into three separate steps: excitation of an electron within the bulk of the material, transport of the electron from the excitation site to the photocathode's surface, and then emission of the electron through the surface barrier. By modeling each of these steps, the important cathode parameters can be estimated. Here, we will concern ourselves with MTE and also the quantum efficiency (QE), which is the (fractional) number of electrons emitted from the cathode per incident photon.

Fortunately, these properties can be calculated analytically for metallic cathodes under suitable approximation [39]. The chance of a photon with energy $h\nu$ exciting an electron in the photocathode with initial energy E is the transition probability $[1 - f_{\mathrm{FD}}(E + h\nu)] f_{\mathrm{FD}}(E)$, where f_{FD} represents the Fermi-Dirac distribution function. Here the first and second terms represent the density of the final and initial states of the electron. This, however, must be multiplied by $(1 - R(h\nu))$ where $R(h\nu)$ is the reflectivity to account for the fact that not all incident photons

make it into the metal.

Electron-electron scattering is predominantly responsible for the loss of particles in transport in metals. This effect only depends on photon energy and can be modeled by the ratio of the optical absorption length and an experimentally measured electron-electron scattering length. We write this as $F_{\text{e-e}}(h\nu) = 1/(1 + \lambda_{\text{opt}}(h\nu)/\lambda_{\text{e-e}}(h\nu))$. These lengths are approximately constant when only considering near-threshold photoemission.

When an electron escapes the material, the transverse momentum is conserved, but the momentum component normal to the surface shrinks to satisfy energy conservation across the barrier. In particular, when we reference the energy to the Fermi level, the particle must lose energy equal to the work function (ϕ). This means that there is a maximum angle beyond which electrons no longer have enough longitudinal momentum to escape the material. The momenta of the internally excited electrons tend to be distributed randomly in orientation. This lets us calculate the probability of escape as the area of the unit sphere contained in the cone defined by the maximum escape angle divided by the total area of the unit sphere.

With these values for the rates in the three-step model, the QE and MTE can be estimated. The QE is the probability of a photon being absorbed and the resulting electron being able to escape divided by the probability of a photon being absorbed at all. This can be found by integrating a product of the rates over all states in the metal. For near threshold photoemission and taking the cathode's temperature as zero we have,

$$\text{QE}(h\nu) = \frac{1 - R(h\nu)}{1 + \lambda_{\text{opt}}(h\nu)/\lambda_{\text{e-e}}(h\nu)} \frac{(h\nu - \phi)^2}{8\phi(E_F + \phi)}, \tag{1.4}$$

where ϕ is the Fermi energy. The MTE can be evaluated similarly by evaluating

an expectation value of the squared transverse momentum over the escaped electrons. We have the surprisingly simple result,

$$\text{MTE} = \frac{h\nu - \phi}{3}. \tag{1.5}$$

Here we see the tradeoffs inherent in photocathode-based electron sources. Mean transverse energy should go down when the wavelength of the driving laser is tuned close to the photoemission threshold. However the quantum efficiency also decreases and $\text{MTE}(h\nu) \propto \sqrt{\text{QE}(h\nu)}$. Unfortunately, the theory of MTE dropping off to zero as long as you have a powerful enough drive laser doesn't seem to be true in practice either. In reality, it drops off to a value near 25 meV for many materials [15]. Why this happens may be due to several effects. This includes surface roughness which may inflate the transverse momentum of the emitted electrons [76]. Variation of the work function across the surface can cause similar issues [60]. The limiting value is also close to the energy $k_B T$ at room temperature and so thermal effects such as the Fermi tail may be at play.

1.3 Structure of the Thesis

This thesis encompasses a line of research into increasing the brightness of electron beams. With the existing popularity of photoinjectors as a way of generating high-brightness electron beams, improvements to these sources and the photocathode materials which power them are a promising method of accomplishing this goal.

As discussed in the previous section, the two areas a serious attempt at increasing photocathode brightness should look at are initial spot size and mo-

mentum spread. Shrinking either improves the quality of the generated beam. Fortunately, there does seem to be room for improvement over existing cathode technologies. Although the source size is typically restricted by optics to 1 μm, manipulation of the surface with nanopatterning shows promise as a way of beating this limit. The initial momentum spread is determined by both the photocathode material and the wavelength of the driving laser (typically shrinking at a longer wavelength). Both parameters have interesting areas of exploration. Common photocathode materials exist that have not been measured at long wavelengths and could yield new bright sources of electrons. Additionally, there are semiconductors whose electronic bandstructure naturally restricts the momentum of electrons in the crystal. Perhaps these could be leveraged to also limit the transverse energy of the emitted beam. Each of these starting points suggests a fruitful area of research that could improve the brightness of electron beams.

Unfortunately, it isn't clear that this line of research, even if successful, would have an impact on the brightness of electron beams delivered to users in the real world. There is a lot that can go wrong from the point where the beam is generated to the point where it is used. In particular, many applications require a high bunch charge. The nonlinear space charge forces that may be present in this regime of operation can have a serious effect on the brightness in transport. Even in the case of low current, nonlinearities in beamline elements and projected effects such as slice mismatch in phase-space may inflate the emittance of the cathode. These issues might hide any gains made in the photoinjector. It is therefore important to understand the magnitude of these effects and their relation to the brightness offered by photocathode improvements before spending too much effort on that research.

To this end, we begin the thesis in Chapter 2 with numerical work aimed at understanding the conservation of brightness in realistic photoinjectors. Optimizations were performed on particle tracking simulations of a diverse set of accelerators. We evaluated the best achievable emittance that is obtained with contemporary photocathodes and that which can be achieved using photocathodes with zero MTE. We find that these systems can still benefit from higher quality photocathodes and define a metric on each system for the value of MTE one would have to reach before the effects of transport blur the cathode's contribution to brightness.

In Chapter 3, an investigation into the near-threshold MTE of Cs-Te (a common semiconductor photocathode) is presented. We believe this is the first work reporting this data. Interestingly, instead of the MTE decreasing monotonically as the photon energy is reduced, it first decreases and then shoots up close to the threshold before shrinking again. We were able to explain this feature as being caused by low work function compounds that form in thermodynamic equilibrium with main semiconductor Cs_2Te in the cathode. When the laser is tuned near threshold those impurities begin emitting electrons with greater efficiency than the bulk and it is these electrons that are responsible for the higher-than-expected MTE. These results show that for systems such as Cs-Te, it is not enough to simply turn down the photon energy of the driving laser when seeking high brightness. Instead, more complex features with local minima may be present that require consideration when optimizing your photoinjector.

Chapter 4 describes measurements from a low effective mass (small momentum spread) semiconductor involving an unconventional method of emitting electrons from the unoccupied conduction band states. Instead of using sin-

gle photons to rip the electrons from the photocathode, this concept involved exciting electrons into the conduction band of GaAs with a laser pulse of low-energy photons. Then after a delay, which allows the electrons to thermalize and lose transverse momentum as they settle into the conduction band minimum, a pulse of higher energy photons would kick these electrons out of the material. Previous work did observe small MTE in a narrow energy-resolved set of emitted electrons. We present here the first measurements of momentum spread over the full distribution in an attempt to develop a new high-brightness source of electrons.

In Chapter 5, a nanopatterning concept on the path to a smaller source size is explored. Metal photocathodes are durable and easy to prepare, but their low QE and high work function make them difficult to use. The requirement of UV light can be relaxed when these cathodes are driven with intense ultrafast laser pulses into nonlinear photoemission. However, the achievable photoemission yield tends to be small. In this work, we explore how patterning the surface of the metal can locally enhance the optical field and improve the nonlinear yield by six orders of magnitude. We also perform the first MTE measurements on this system and demonstrate how these cathodes may be used in future high-brightness photoinjectors.

CHAPTER 2

CONSERVATION OF CATHODE BRIGHTNESS IN THE REAL WORLD

This chapter was originally published as reference [121][1].

2.1 Abstract

Reducing the intrinsic emittance of photocathodes is one of the most promising routes to improving the brightness of electron sources. However, when emittance growth occurs during beam transport (for example, due to space-charge), it is possible that this emittance growth overwhelms the contribution of the photocathode and, thus, in this case source emittance improvements are not beneficial. Using multi-objective genetic optimization, we investigate the role intrinsic emittance plays in determining the final emittance of several space-charge dominated photoinjectors, including those for high repetition rate free electron lasers and ultrafast electron diffraction. We introduce a new metric to predict the scale of photocathode emittance improvements that remain beneficial and explain how additional tuning is required to take full advantage of new photocathode technologies. Additionally, we determine the scale of emittance growth due to point-to-point Coulomb interactions with a fast tree-based space-charge solver. Our results show that in the realistic high brightness photoinjector applications under study, the reduction of thermal emittance to values as low as $50\,\mathrm{pm}\,\mu\mathrm{m}^{-1}$ (1 meV MTE) remains a viable option for the improvement of beam brightness.

[1]The following acknowledgment appeared in the original manuscript: This work was supported by the U.S. National Science Foundation under Award PHY-1549132, the Center for Bright Beams. We thank the US-Japan Science and Technology Cooperation Program in High Energy Physics for providing additional travel funding.

2.2 Introduction

Improving the brightness of space-charge dominated electron sources will unlock a wealth of next generation accelerator physics applications. For example, the largest unit cell that may be studied with single shot ultrafast electron diffraction (UED) is limited by the beam's transverse coherence length, which is determined by transverse emittance, at a high enough bunch charge to mitigate the effects of shot noise in data collection. The study of protein dynamics with UED requires producing >1 nm scale coherence lengths at more than 10^5 electrons and sub-picosecond pulse lengths at the sample location [150, 43]. In another example, the intensity of coherent radiation available to the users of free electron lasers (FELs) is, in part, limited by beam brightness. Beam brightness affects the efficiency, radiated power, gain length, and photon energy reach of FELs [137, 35].

Photoinjectors equipped with low intrinsic emittance photocathodes are among the brightest electron sources in use today. Peak brightness at the source is limited by two factors: the electric field at the cathode and the photocathode's transverse momentum spread. Several short-pulse Child-Langmuir-like charge density limits have been derived for the photoemission regimes of relevance to practical photoinjectors. These current density extraction limits make explicit the dependence of peak brightness on photocathode parameters and the electric field [16, 49, 149]. Depending on the aspect ratio of the bunch, the brightness limit is super-linear in the electric field and motivates the push towards high accelerating gradient photoinjectors. Contemporary DC, normal-conducting RF (NCRF), and superconducting RF (SRF) photoelectron guns have peak accelerating fields of order $10\,\mathrm{MV\,m^{-1}}$ [125, 41, 38, 7]

with very high repetition rates (well above 1 MHz). At the cost of duty factor, state of the art NCRF electron guns can offer even higher fields of order 100 MV m^{-1} [47] and recent experimental results suggest the possibility of pushing peak fields to nearly 500 MV m^{-1} for cryogenically cooled accelerating structures [139, 23, 161, 138, 95, 144, 111, 56, 34, 63, 37, 90].

In this work, we characterize the intrinsic emittance at the photocathode source via the Mean Transverse Energy (MTE):

$$\varepsilon_{\mathrm{C}} = \sigma_x \sqrt{\frac{\mathrm{MTE}}{mc^2}}, \tag{2.1}$$

where σ_x is the laser spot size, and m is the mass of the electron. Here, it is clear that MTE plays the role of an effective temperature of emission.

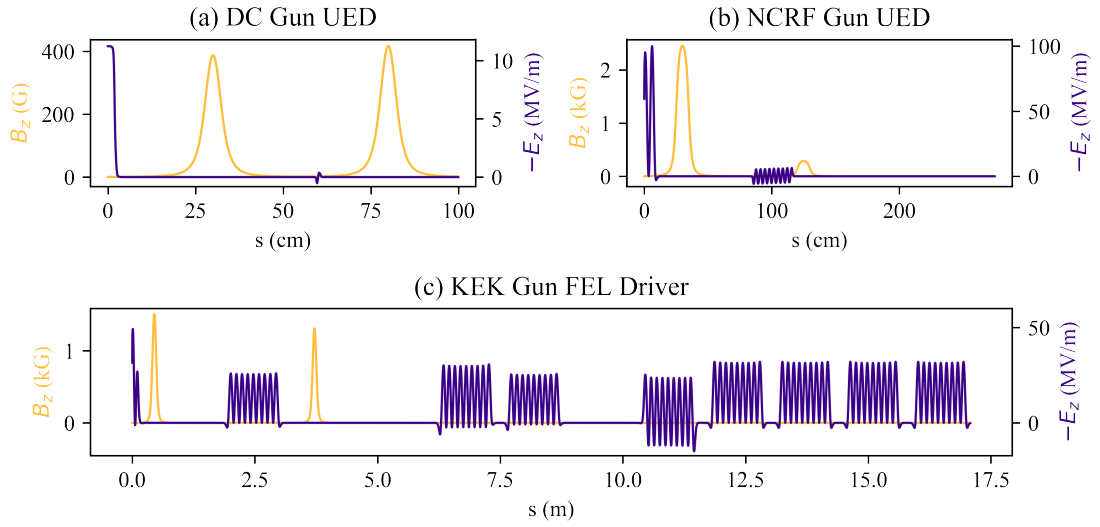

Figure 2.1: The on-axis electric and magnetic field as seen by a reference particle in the center of the electron bunch. In each sub-figure, the cavity and magnet parameters are taken from an individual along the 0 meV Pareto front of the respective beamline. Fields are output directly from General Particle Tracer. In the case of the FEL, fields are computed from the energy change ($\mathrm{d}E/\mathrm{d}s$) and Larmor angle output from ASTRA as a function of position.

Great progress is being made in the discovery of low MTE photocathodes which are expected to improve the usable brightness of photoinjectors. Due to

the practical tradeoffs involved with photocathode choice, most photoinjectors today use materials with an MTE of around 150 meV [163, 167, 36, 94]. At the cost of QE, this MTE may be reduced by tuning the driving laser's wavelength. For example, in Cs_3Sb and Cs:GaAs photocathodes, the lowest MTE that may be achieved via wavelength tuning at room temperature is nearly 35 meV and 25 meV respectively, but at 10^{-6} - 10^{-5} QE [118, 29, 103]. Recent work has shown that the cryogenic cooling of photocathodes emitting at threshold can reduce MTE even further, potentially down to single digit meV MTEs [74]. However, a natural question arises amidst this progress in MTE reduction: in modern space-charge dominated applications, to what extent does MTE reduction actually improve the final emittance?

Even in the case of linear transport, 3D space-charge effects lead to a transverse position-angle correlation which varies along the longitudinal coordinate and leads to an inflation of projected emittance that requires compensation [24, 55, 134, 147]. The residual emittance after compensation is due to non-linear forces, either from space-charge or beamline elements. Scaling laws exist to help estimate their effects [25, 17]. In some cases, non-linearity can cause phase space wave-breaking in unevenly distributed beams that is a source of irreversible emittance growth [5, 6]. Another irreversible cause of emittance growth is disorder induced heating (DIH) and other Coulomb scattering effects which are expected to become important in the cold dense beams of future accelerator applications [93]. Avoiding these emittance growth mechanisms requires the advanced design and tuning of photoinjector systems.

Multi-objective genetic algorithm (MOGA) optimization is a popular technique for the design and tuning of realistic photoinjectors [11, 114, 70, 115, 133,

44, 117]. Photoinjectors often have to balance several key design parameters or objectives that determine the usefulness of the system for a given application. MOGA is a derivative free method for computing the Pareto front, or family of highest performing solutions, in a parallel and sample efficient manner [32]. Elitist genetic algorithms are known to converge to the global optima of sufficiently well-behaved fitness functions given enough evaluations [141]. This makes them well suited for problems involving many local extrema. Practical problems often require optimizations to be performed over a constrained search space and there exist techniques of incorporating these constraints into existing genetic algorithms without sacrificing efficiency [18].

In this work, we examine the limits beam transport places on the ability of photoinjectors to take advantage of low MTE photocathodes in a diverse set of realistic simulated photoinjectors that have been tuned by a MOGA for ultimate performance. This article begins with a discussion of our results involving the simulations of beamlines with idealized zero emittance photocathodes. These simulations are performed on three important examples of high brightness electron beam applications: high repetition rate FELs, as well as single-shot DC and RF-based UED devices. Using zero cathode emittance simulations, we introduce a new metric called the characteristic MTE to help understand the scale of photocathode MTE which is relevant to final beam quality. It is shown that, depending on the properties of the beamline, system parameters need to be re-optimized to take full advantage of photocathode improvements. We present a method of estimating when re-optimization needs to be performed and the magnitude of its effect on final emittance. Finally, we set the scale for the magnitude of emittance growth due to point-to-point Coulomb interactions using a stochastic space-charge algorithm.

2.3 Optimizations with a 0 meV MTE Photocathode

To understand the contribution of photocathode MTE towards the final emittance of high brightness photoinjectors, we directly compare injector performance with a contemporary ~150 meV MTE photocathode to what would be achievable with a perfect 0 meV counterpart. To cover the wide range of existing and near future accelerator technologies, we chose three realistic beamlines with significantly different energies as a representative set of high brightness photoinjector applications. A DC and NCRF electron gun based single shot UED beamline reflect the two predominant energy scales of electron diffraction with single nanometer scale emittance at 10 to 100 fC bunch charge: order of magnitude 100 keV and 1 MeV. At higher bunch charge, we select an SRF photoinjector under development at KEK expected to be capable of sub-μm scale emittance at 100 pC bunch charge for simulations representative of FEL driver applications. We consider these beamlines to be space-charge dominated based off of their expected applications which are anticipated to push their machine settings into a range where space-charge forces become important.

The ultimate performance of each system is evaluated on the basis of the particle tracking codes General Particle Tracer [158] and ASTRA [54] with optimization carried out in the framework of MOGA. Particle tracking simulations have been shown to have good correspondence with the dynamics of real beamlines [65]. Children were generated with simulated binary crossover and polynomial mutation [31]. Selection was performed with SPEA-II [173] in the case of both UED examples and with NSGA-II [32] in the case of the FEL example. Emittance preservation is known to depend strongly on the initial transverse and longitudinal distribution of the beam. To this end, the optimizer is

given the power to change parameters controlling the initial particle distribution. In particular, the optimizer may change the size and length of the beam while preserving cylindrical symmetry. The shape of the beam along the radial and longitudinal axes is interpolated between the set of four distributions described in [17]. Example initial distributions taken from one individual for each beamline are shown in Fig. 2.2.

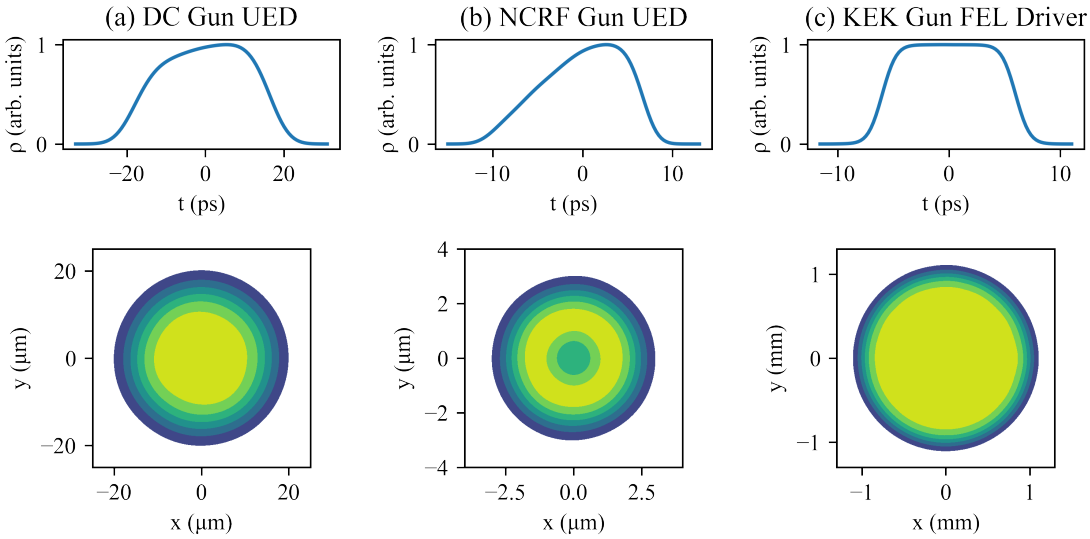

Figure 2.2: An example of the initial longitudinal and transverse spatial distribution of the beam for each system. These examples were selected from the 0 meV Pareto front and are the same individuals plotted in Fig. 2.5.

The DC UED beamline is modeled after a similar system under development at Cornell University using the cryogenically cooled photoemission source described in [85]. The performance of this system under different conditions than presently considered is discussed in [64] where a detailed description of the layout and simulation methodology is also provided. On-axis fields for this beamline are shown in Fig. 2.1a. The beamline consists of two solenoids that surround an NCRF single cell bunching cavity and aid in transporting the high brightness beam to the sample located at $s = 1$ m. The optimizer is given control over all magnet and cavity settings to minimize the RMS emittance at the

sample while maximizing bunch charge. Only solutions that keep the final spot size smaller than 100 µm RMS and the final beam length less than 1 ps RMS are considered. These constraints were chosen based on common sample sizes used in diffraction [163] and the timescale of lattice vibration dynamics [88, 152]. For a complete description of the decisions, objectives, and constraints used for this system, refer to Tab. 2.1.

The high gradient NCRF UED beamline is driven by a 1.6 cell 2.856 GHz gun capable of 100 MV m^{-1} and based on a design currently in use at a number of labs [163, 104, 172, 171, 50]. Samples are located at s = 2.75 m and the optimizer is given full control over two solenoids which surround a nine cell bunching cavity that is modeled after the first cell of the SLAC linac described in [108]. A discussion of our previous optimization experience with this beamline under a different set of constraints can be found in [66]. As in the case of the DC UED beamline, the optimizer was configured to minimize final RMS emittance while maximizing delivered bunch charge under the constraint of keeping the final spot size less than 100 µm RMS and the final length shorter than 1 ps RMS. The decisions, objectives, and constraints of this optimization are detailed in Tab. 2.2 and an example of the on-axis fields from an optimized individual is shown in Fig. 2.1b.

Our FEL driver example includes a 1.5 cell 1.3 GHz SRF gun in development at KEK for use in a CW ERL light source coupled with a photoinjector lattice aimed at use in the LCLS-II HE upgrade [78]. The gun energy is controlled by the optimizer, but is in the range 1.5 to 3.5 MeV. Immediately after the gun is a 1.3 GHz 9 cell capture cavity surrounded by two solenoids. The remaining cavities, of the same design as the capture cavity, are shown in the plot of ex-

Decision	**Range**
Bunch Charge	0 to 160 fC
Initial RMS Beam Size	0 to 1 mm
Intitial RMS Beam Length	0 to 50 ps
MTE	0, 150 meV
Gun Voltage	225 kV
Solenoid Current 1 and 2	0 to 4 A
Buncher Voltage	0 to 60 kV
Buncher Phase	90°

Objective	**Goal**
RMS Emittance	Minimize
Delivered Bunch Charge	Maximize

Constraint	**Value**
Final RMS Spot Size	<100 µm
Final RMS Bunch Length	<1 ps

Table 2.1: Optimizer configuration for the DC gun UED beamline

ternal fields in Fig. 2.1c and accelerate the beam to its final energy of roughly 100 MeV. Accelerating cavity number three was kept off during optimization as a planned backup for cavity failure in the real machine. The bunch charge was fixed to 100 pC, and optimizations were performed to minimize both RMS emittance and bunch length at the end of the injector system. Energy constraints were tailored for the injector's use in the LCLS-II HE upgrade, and so we required valid solutions to have an energy greater than 90 MeV, an energy spread below 200 keV, and a higher order energy spread less than 5 keV. The full set of decisions, objectives, and constraints is compiled in Tab. 2.3.

Initial generations of the genetic optimization were evaluated with a small number of macroparticles to develop a good approximation of the global optima before moving on to the more accurate simulations involving 10^5 macroparticles

Decision	Range
Bunch Charge	0 to 300 fC
Initial RMS Beam Size	0 to 50 µm
Intitial RMS Beam Length	0 to 50 ps
MTE	0, 150 meV
Gun Phase	−90 to 90°
Peak Gun Field	100 MV m^{-1}
Beam Energy	4.5 MeV
Solenoid Current 1 and 2	0 to 4 A
Buncher Peak Power	0 to 25 MW
Buncher Phase	90°

Objective	Goal
RMS Emittance	Minimize
Delivered Bunch Charge	Maximize

Constraint	Value
Final RMS Spot Size	<100 µm
Final RMS Bunch Length	<1 ps

Table 2.2: Optimizer configuration for the NCRF UED beamline

for the UED examples and 10^4 macroparticles for the FEL driver. The optimization stopping condition was that improvement of the Pareto front with each successive generation fell below a threshold of approximately 10% relative change. The products of these optimizations are shown in Fig. 2.4.

Both UED beamlines show a factor of between 10 and 100 improvement in brightness when the 150 meV photocathode is replaced by its 0 meV counterpart. The degree of improvement is slightly greater in the case of the DC gun UED beamline. As seen in Fig. 2.3, the optimizer chooses a smaller initial spot size for the NCRF gun individuals than for the DC gun individuals. We conjecture that this is enabled by the higher accelerating gradient of the NCRF gun lim-

[2]Gun energy is computed from gradient and phase and not directly controlled by optimizer

Decision	Range
Bunch Charge	100 pC
Initial RMS Beam Size	0.05 to 10 mm
Initial RMS Beam Length	5 to 70 ps
MTE	0, 130 meV
Gun Gradient	20 to 50 MV m^{-1}
Gun Phase	−60 to 60°
Gun Energy [2]	1.5 to 3.5 MeV
Solenoid 1 Field	0 to 0.4 T
Capture Cavity Gradient	0 to 32 MV m^{-1}
Capture Cavity Phase	−180 to 180°
Capture Cavity Offset	0 to 2 m
Solenoid 2 Field	0 to 0.3 T
Solenoid 2 Offset	0 to 2 m
Cryomodule Offset	0 to 3 m
Accel. Cavity 1, 2, and 4 Field	0 to 32 MV m^{-1}
Accel. Cavity 1, 2, and 4 Phase	−90 to 90°

Objective	Goal
RMS Emittance	Minimize
Final RMS Bunch Length	Minimize

Constraint	Value
Final Energy	>90 MeV
Energy Spread	<200 keV
Higher Order Energy Spread	<5 keV

Table 2.3: Optimizer configuration for the KEK gun FEL driver example.

iting the effects of space-charge emittance growth. Due to the fact that initial emittance depends on both the photocathode's MTE and the initial spot size, a smaller initial spot size can mitigate the effects of a high thermal emittance photocathode. The NCRF beamline also outperforms the DC beamline for emittance in absolute terms at similar bunch charges further suggesting a benefit with higher gradients on the cathode. There is a sharp rise in slice emittance

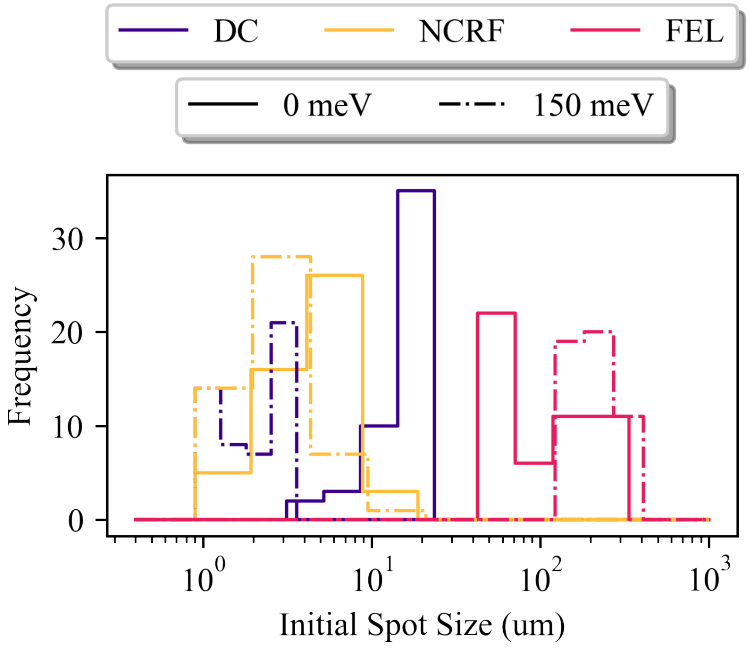

Figure 2.3: The probability distribution of initial spot sizes among the optimized individuals. The three example beamlines are labeled by color and individuals from the ~150 meV fronts are in dashed lines while the individuals from the 0 meV fronts are represented by solid lines.

while the beam is still inside the gun and at low energy seen in Fig. 2.5a and 2.5b. This suggests that non-linear space-charge forces play a role in the residual emittance and the higher gradient and energy of the NCRF example could explain why it outperforms the DC example. We observed that the brightness improvement from the 0 meV photocathode was limited to a factor of ten in the case of the FEL driver. The higher bunch charge of this application is expected to increase the role of space-charge forces in transport and could be a cause of this more modest improvement.

At the end of every beamline and for each individual we calculated the parameter

$$\rho = \frac{I}{I_0} \cdot \frac{\sigma_x^2}{\beta\gamma\varepsilon^2},$$

where I_0 is the Alfven current, I is the average current, and β and γ have their typical definitions in special relativity. This represents the ratio of the space-charge and emittance pressure terms in the beam envelope equation. It was greater than one in all cases which confirms that all of the beamlines operating with optimized settings are space-charge-dominated. The ratio ρ was larger by at least an order of magnitude for individuals from the 0 meV Pareto fronts than for individuals from the 150 meV / 130 meV fronts for comparable bunch charge or length.

2.4 The Characteristic MTE Metric

As long as the beam dynamics of the system do not change significantly with the introduction of a new photocathode, we can use the heuristic relationship that non-zero initial emittance will add roughly in quadrature with the emittance due to beam transport and the final emittance will be

$$\varepsilon^2 \approx \varepsilon_{\mathrm{T}}^2 + \sigma_{x,i}^2 \frac{MTE}{mc^2}, \tag{2.2}$$

where ε_{T} is the emittance gained in beam transport, $\sigma_{x,i}$ is the initial spot size, and $\varepsilon_{\mathrm{C}} = \sigma_{x,i}\sqrt{\frac{MTE}{mc^2}}$ is the initial emittance due to the photocathode and initial spot size. To understand when the photocathode's MTE is important in the final emittance, we define a characteristic MTE that would result in the emittance contribution of the photocathode and beam transport being equal as

$$\mathrm{MTE}_C = mc^2 \left(\frac{\varepsilon_{\mathrm{T}}}{\sigma_{x,i}} \right)^2 . \tag{2.3}$$

The characteristic MTE is a beamline specific quantity that sets the scale for when photocathodes play a significant role in determining the final emittance

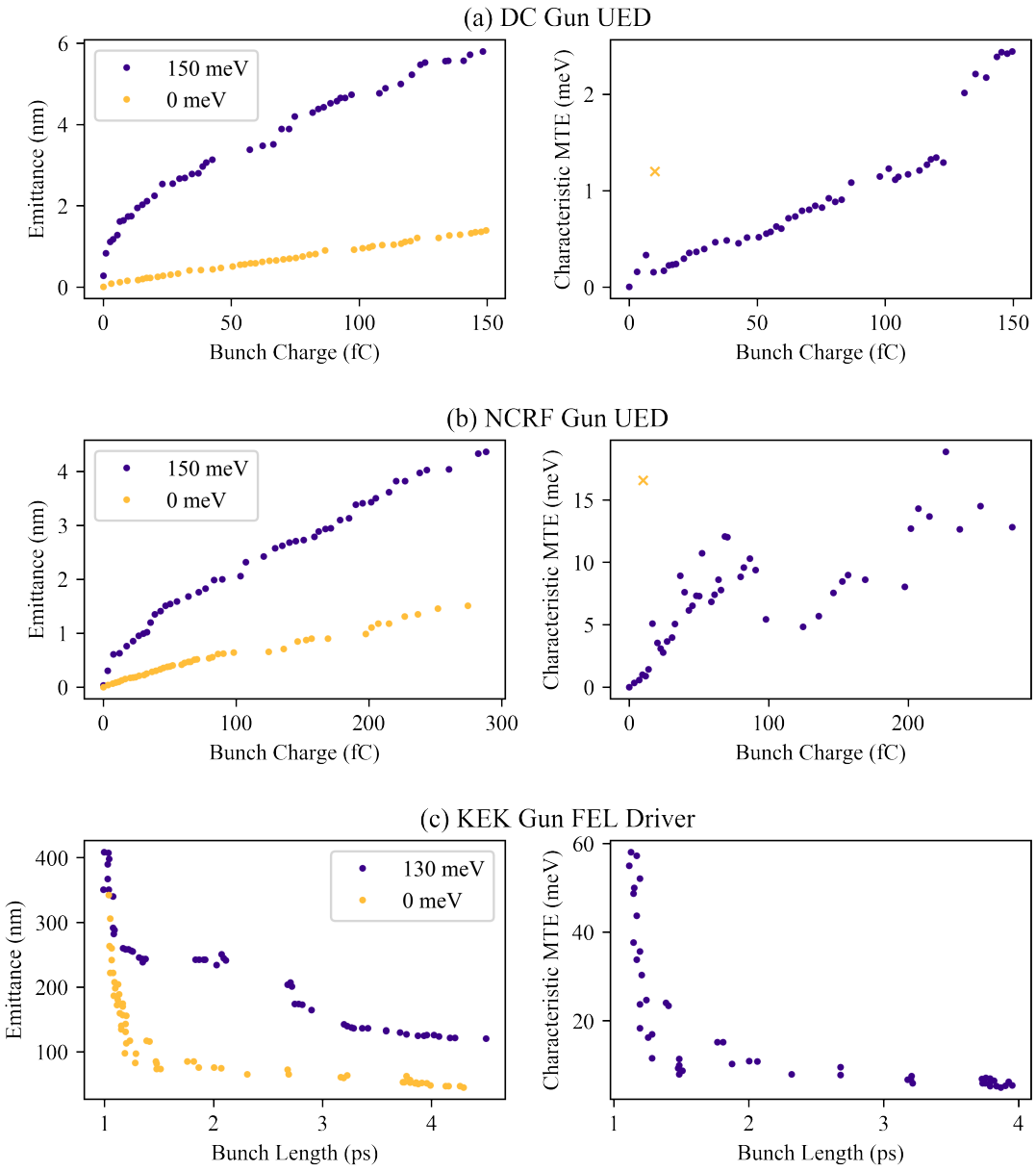

Figure 2.4: The Pareto fronts of each beamline for the ~150 meV and 0 meV MTE photocathodes and their characteristic MTE. The UED examples show between a factor of 10 and 100 improvement in brightness between the two Pareto fronts. The characteristic MTE calculated from a simulation including the effects of Coulomb scattering is included for the DC and NCRF Gun UED examples as a yellow cross.

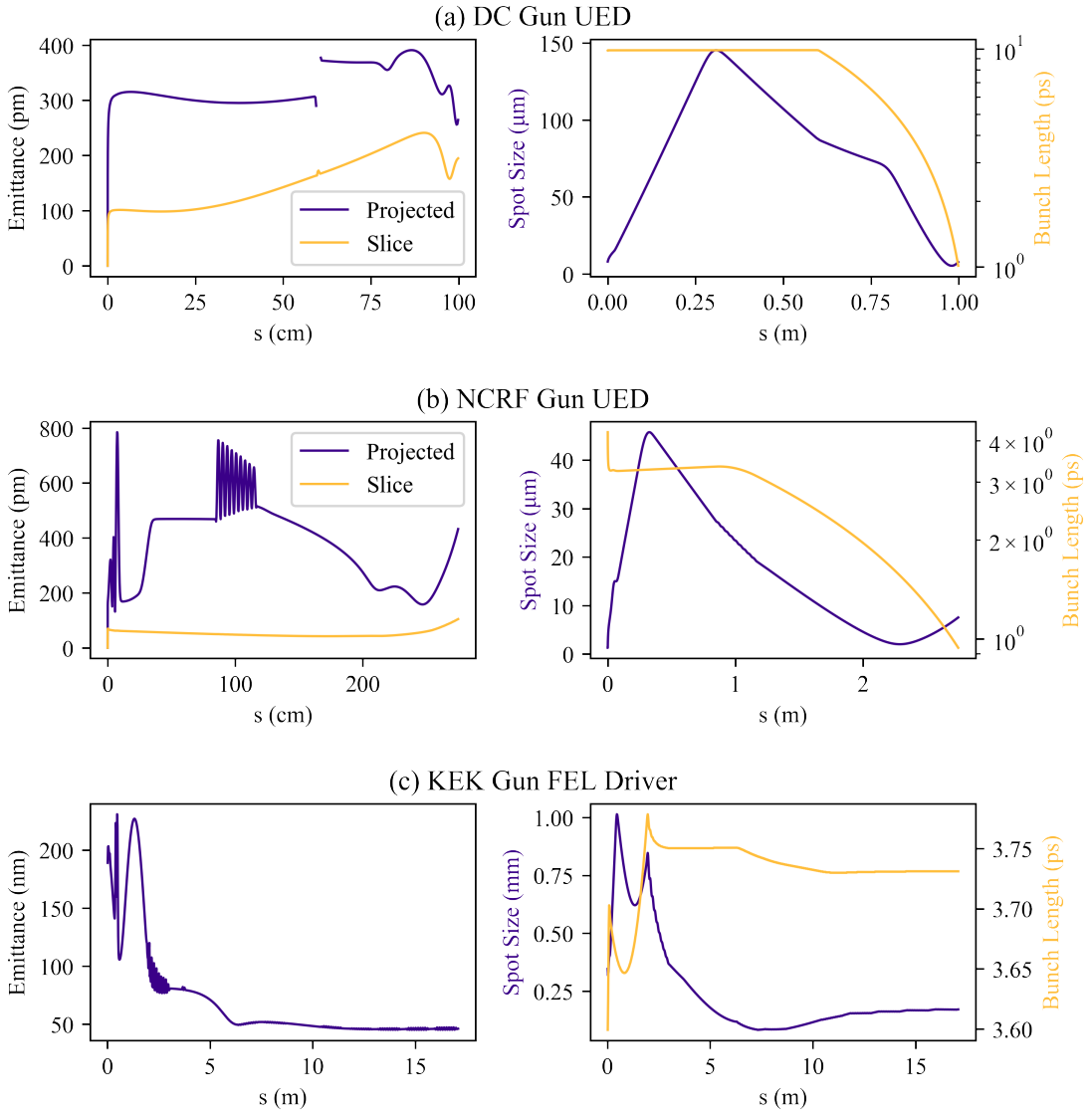

Figure 2.5: Emittance and beam sizes for an individual along the 0 meV Pareto front of each example. The UED individuals were selected at 16 fC bunch charge. The projected emittance is the typical RMS normalized transverse emittance and the slice emittance is the average of the emittance evaluated over 100 longitudinal slices. Beam width and length are also plotted for reference. The total projected emittance in Fig. a is clipped at 500 pm for clarity.

of a photoinjector. Photocathode improvements down to the characteristic MTE are likely to translate into increased usable brightness.

The characteristic MTE of each example is shown in Fig. 2.4. Photocathode improvements down to the level of single meV MTE do affect the final emittance of each photoinjector application studied here. The characteristic MTE of the NCRF UED and FEL driver examples increases to roughly 15 meV and 50 meV at high bunch charge and short bunch length respectively. The larger characteristic MTE of the NCRF UED example is likely due to the smaller initial spot size of the individuals. This can be seen in Fig. 2.3. That smaller spot size will increase the characteristic MTE for the same emittance because the initial emittance is less sensitive to photocathode parameters. Characteristic MTE at short bunch lengths in the FEL example are primarily limited by large emittance growth in beam transport.

To test the validity of the heuristic argument that initial and transport emittance should add in quadrature, we simulated each individual from the 0 meV Pareto fronts with a photocathode whose MTE is the characteristic MTE. The final emittance is expected to grow by a factor of $\sqrt{2}$ and we observe the ratio to be close but slightly larger than that value. The frequency of ratios for each beamline is plotted in Fig. 2.6. For our investigation, we assume that the insertion of a new photocathode does not significantly change beam transport. However, this condition will be violated to some extent and could explain why the ratio observed is slightly larger than $\sqrt{2}$.

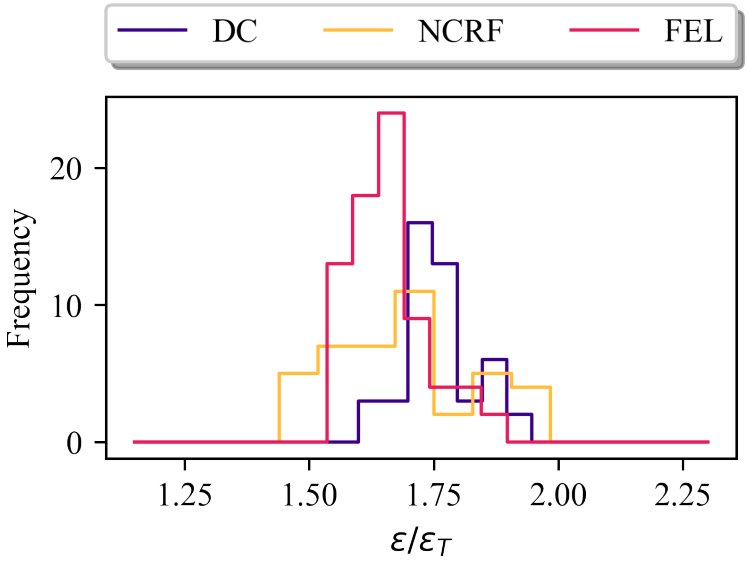

Figure 2.6: Individuals from the 0 meV beamline were re-simulated with a photocathode MTE equal to their characteristic MTE. The probability distribution of the ratio of the new final emittance to the original final emittance is plotted.

2.5 Re-Optimization for New Photocathodes

Our optimization experience showed that taking full advantage of the initial emittance improvements afforded by a new low MTE photocathode required the re-optimization of beamline parameters. In particular, when individuals from the 150 meV Pareto fronts of the UED beamlines are re-simulated with a 0 meV photocathode and no changes to beamline parameters, their emittance is more than fifty percent larger than the emittance of individuals in the 0 meV Pareto front at comparable bunch charge. This can be understood by considering the sensitivity of the transport emittance optimum to small changes in the initial spot size.

The characteristic MTE analysis does not take into account the fact that if shrinking the initial spot size from its optimal value reduces the initial emittance more than it increases emittance growth in transport, then the overall emittance

will still go down. The initial emittance, as in Eq. 2.1, can be reduced by using a smaller initial spot size. However, if the system was already at the initial spot size which minimizes emittance growth in transport, as is the case of individuals along the 0 meV Pareto front, then changing it will negatively affect beamline performance. Since the final emittance is roughly the quadrature sum of the initial emittance and the growth during transport, there will be a trade-off in minimizing both the initial emittance and emittance growth. If the system was previously optimized with a high MTE photocathode, then the optimal spot size will not be at the minimum transport emittance possible and new low MTE photocathodes can unlock strategies the optimizer avoided due to their larger spot sizes which increase initial emittance. In this case, re-optimization will be required upon the insertion of a new low MTE photocathode.

This trade-off is represented graphically in Fig. 2.7 by plotting emittance as a function of initial spot size. Initial emittance is linear in the initial spot size and is represented by a line whose slope depends on photocathode MTE. Close to the optimum, the emittance due to transport may be expressed as a polynomial expansion in $\sigma_{x,i}$ which, to lowest order, is quadratic. The final emittance is roughly the quadrature sum of both terms and has an optima at a smaller spot size than for transport emittance alone. Characteristic MTE can also be represented in this plot since the initial emittance for a photocathode with an MTE equal to the characteristic MTE will pass through the vertex of the transport emittance parabola.

By using the second order expansion of beam transport's contribution to the emittance (ε_{T}) as a function of initial spot size ($\sigma_{x,i}$) around the optimum,

$$\varepsilon_{\mathrm{T}}(\sigma_{x,i}) = A(\sigma_{x,i} - \sigma_{x,i,0})^2 + \varepsilon_{\mathrm{T},0}, \tag{2.4}$$

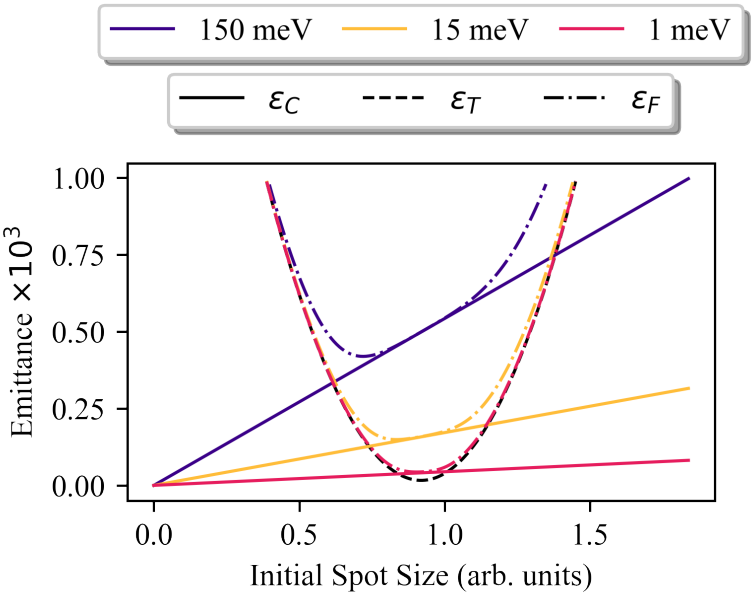

Figure 2.7: An illustration of how re-optimization may be required upon insertion of a new photocathode. In black is the emittance due to transport (ε_{T}) as a function of the initial spot size. Around the optimal spot size, $\sigma_{x,i,0}$, this is approximately quadratic. The sensitivity in this example is roughly $x \approx 0.001$. The solid lines represent the initial emittance (ε_{C}) for three different thermal emittances. The dashed lines are the final emittance (ε_{F}), or the quadrature sums of initial and transport emittance. The optimal spot size with the 150 meV photocathode is significantly smaller than with a 0 meV or even 1 meV photocathode.

we can find the new optimal emittance with non-zero MTE. Here $\sigma_{x,i,0}$ is the optimal spot size and $\varepsilon_{\mathrm{T},0}$ is the optimal emittance. To simplify our discussion, we consider the case of optima that are highly sensitive to changes in initial spot size. Define the unitless parameter $x = \varepsilon_{\mathrm{T},0}/(A\sigma^2_{x,i,0})$ to measure the optimum's sensitivity. In the limit of sensitive optima ($x \ll 1$) the new smallest emittance when the initial spot size is allowed to vary is

$$\varepsilon^2_{\mathrm{opt}} = \varepsilon^2_{\mathrm{T},0} + \varepsilon^2_{\mathrm{C}}\left[1 - \frac{x}{2}\frac{\mathrm{MTE}}{\mathrm{MTE}_C}\right] \quad (x \ll 1). \tag{2.5}$$

The new optimal initial spot size will be smaller for the non-zero MTE photocathode and, in the limit of small x, is approximately

$$\sigma^2_{x,i,opt} = \sigma^2_{x,i,0}\left[1 - x\frac{\mathrm{MTE}}{\mathrm{MTE}_C}\right] \quad (x \ll 1). \tag{2.6}$$

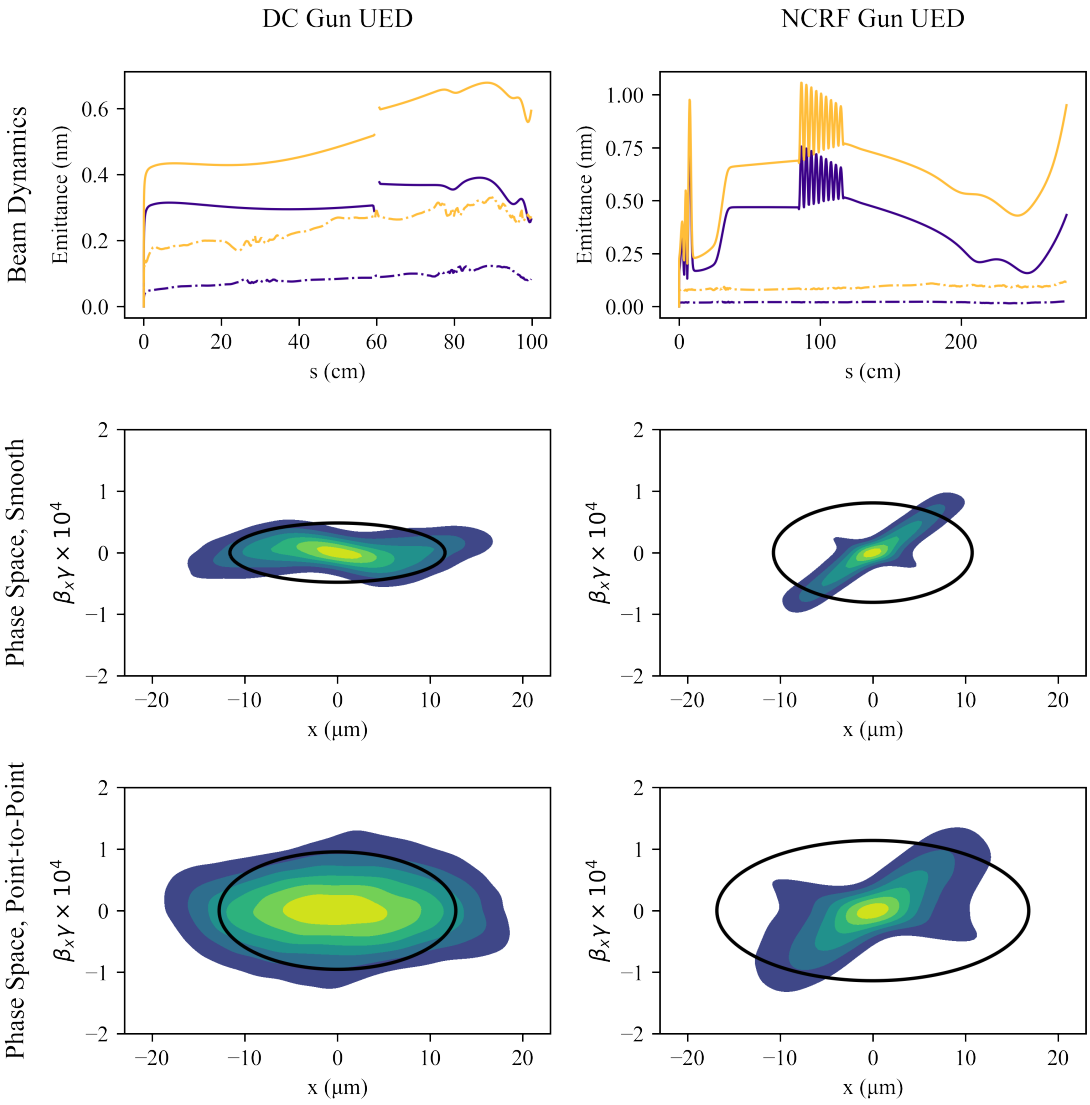

Figure 2.8: The RMS and core emittance of an individual with 10^5 electrons per bunch from the DC gun UED and NCRF gun UED 0 meV MTE Pareto fronts. In the row labeled "Beam Dynamics", the yellow lines were computed with the point-to-point space-charge algorithm and the blue lines with smooth space-charge. The solid lines are the RMS normalized emittance and the dashed lines are the core emittance. Below, are plots of the beam's transverse phase space at the sample location computed with the smooth and point-to-point methods. Linear x-p_x correlation have been removed and the ellipse of phase space second moments is plotted in addition to the particle density.

In practice, we observe the tendency of the optimizer to choose smaller initial spot sizes for beamlines with non-zero photocathode MTE. In Fig. 2.3 we plot the frequency of initial spot sizes from the 0 meV and ~150 meV Pareto fronts of each beamline. For the UED examples, the initial spot sizes for individuals in the 150 meV Pareto front are universally smaller than for those in the 0 meV Pareto front. There is less of an impact on the FEL example, which could be due to the optima being highly sensitive to changes in initial spot size.

Systems with insensitive optima (large x) will tolerate higher MTE photocathodes than the original characteristic MTE metric implies. Likewise, systems where the emittance grows rapidly for small changes in $\sigma_{x,i}$ (small x) cannot afford to decrease the initial spot size to compensate for any increase in the photocathode MTE. The second term in the square brackets of Eq. 2.5 is the relative scale for how much changing the initial spot size can improve emittance and can provide a rough guide to experimentalists for determining when a new photocathode technology requires re-optimization of the beamline. The MTE for which the transport and photocathode contributions to the final emittance are the same even when allowing the initial spot size to vary is

$$\mathrm{MTE}'_C = \mathrm{MTE}_C \left[1 + \frac{x}{2}\right] \quad (x \ll 1). \tag{2.7}$$

Although analytical formulas for the optimal emittance and spot size which are accurate to all order in x may be found, they do not lend themselves to efficient analysis and numerical methods may be better suited for investigating the properties of systems with insensitive optima.

For each system, we can use the Pareto fronts obtained for the 0 meV and ~150 meV MTE photocathodes to estimate the sensitivity parameter x and calculate the correction to the characteristic MTE. These Pareto fronts give us a

value of the optimal emittance from Eq. 2.5 for two different values of ε_C and from there we can solve for x. This operation was performed on each system and the sensitivity parameter was used to calculate the corrected characteristic MTE. The correction in all cases was at the single percent level indicating that our optima are sensitive to initial spot size. Consequently, the uncorrected characteristic MTE, for the three realistic photoinjectors studied here, does a good job at predicting the scale at which photocathode improvements no longer improve brightness.

2.6 Stochastic Space Charge

Disorder induced heating (DIH) is known to play a role in degrading the emittance of cold and dense electron beams. When the distance between particles falls below the Debye length of the one component plasma, inter-particle collisions can become important and can affect the momentum distribution of the bunch in a stochastic manner. This effect will show up prominently when the average kinetic energy of particles in the transverse direction is of the same scale as the potential energy due to the Coulomb repulsion of the particle's neighbors. The result is that the nascent momentum spread grows above its initial value by an amount $\Delta kT[eV] = 1.04 \times 10^{-9}(n_0[m^{-3}])^{1/3}$ [93, 157]. Using the electron number density (n_0) at the beginning of each optimized example, the scale of DIH expected for all three beamlines is 1 meV. Beyond DIH, Coulomb scattering after the cathode can lead to continuous irreversible emittance growth, but these effects are difficult to estimate analytically. We expect DIH to be important in our simulations with 0 meV MTE photocathode due to the cold dense beams inside the guns.

To determine how much of an effect Coulomb scattering has on final emittance in our systems, one example from each of the DC and NCRF UED 0 meV Pareto fronts was chosen and simulated using a stochastic space-charge model. The new algorithm for efficiently computing the effects of stochastic space-charge is based off of the Barnes-Hut tree method and will be discussed in detail in a forthcoming publication by M. Gordon, J. Maxson, et al. Both the NCRF and DC UED individuals had a bunch charge of 10 fC. Simulations were performed with GPT's smooth space-charge model discussed in [130] and with the tree-code method. The RMS projected and core emittance [13] along each beamline and with each space-charge model are shown in Fig. 2.8. Coulomb scattering contributes a factor of two increase in final emittance for both cases.

2.7 Conclusion

We have shown that characteristic MTE can be a useful tool in understanding the scale of MTE at which photocathode improvements translate to an increase in usable brightness. These beamlines, which are representative of high brightness photoinjector applications, have characteristic MTEs on the scale of single to tens of meV, well below the 150 meV MTE of today's commonly used photocathodes. Improvements in photocathode technology down to the level of 1 meV and below stands to improve the brightness of practical photoinjectors by an impressive two orders of magnitude. However, it is not enough to simply insert a low MTE photocathode into an electron gun to achieve low final emittance.

To achieve this level of photoinjector performance, advanced optimization

techniques like MOGA will need to be integrated into the design and tuning of future accelerators. With the use of new photocathode technologies, further optimization may be required to take full advantage of low MTE. The sensitivity of the optima to changes in initial spot size provides a guide for when it is necessary to re-optimize. In addition, when in the regime of single meV photocathodes, existing models of smooth space-charge break down and the effects of Coulomb scattering become important in determining ultimate brightness. Although the results of the present work are not affected by this problem because we are only concerned with order of magnitude changes in emittance, design tools for future accelerators may need to move to high performance point-to-point space-charge models to obtain good agreement with reality.

With the continued improvement of photocathode based electron sources and, in particular, the reduction of MTE in photocathode materials, bright beams will open up new possibilities for accelerator physics applications. Notably, an increase in brightness would enable the time resolved characterization of biological macromolecules with UED [145] as well as benefit X-ray FELs with a corresponding increase in total pulse energy benefiting a wide variety of x-ray scattering experiments in fields ranging from condensed matter physics, to chemistry, to biology [3]. Work is already underway in understanding and beating the effects which limit photocathode MTE and in making existing low MTE photocathodes more practical for accelerator facility use [76, 72, 46]. Additionally, structured particle emitters have already been predicted to mitigate the emittance growth observed from disorder induced heating in the present simulations [101]. If these photocathode improvements can be realized, then their results could provide as much as to two order of magnitude improvement in the final brightness of realistic modern photoinjectors.

CHAPTER 3

IMPURITIES AS A BARRIER TO LOW MEAN TRANSVERSE ENERGY

This chapter was originally published as reference [122][1].

3.1 Abstract

We describe measurements of the mean transverse energy (MTE) of Cs-Te photocathodes near the photoemission threshold. The MTE displays an unexpected non-monotonic behaviour as the drive laser's wavelength is tuned to threshold and changes significantly as the photocathode is cooled to cryogenic temperatures. We show that a simple analytical model of photoemission from multiple compounds with a workfunction below that of pure Cs_2Te may describe this behavior. We identify the additional compounds as Cs_5Te_3 and metallic Cs, and by calculating the MTE numerically within the three step model, we reproduce both the wavelength and temperature dependence of the observed MTE. In our model, the MTE changes with temperature arise from realistically small changes in the workfunctions of both compounds and Cs_5Te_3's bandgap energy. These results suggest the existence of an illumination wavelength which is optimal for beam brightness and show that even trace impurities can dominate the MTE for near- threshold photoemission.

[1]The following acknowledgment appeared in the original manuscript: The authors wish to thank Kevin Nangoi and Tomás Arias for valuable discussions. This work was supported by the U.S. National Science Foundation under Award PHY-1549132, the Center for Bright Beams.

3.2 Introduction

The demand for robust photocathodes has made Cs-Te a popular choice for driving free electron lasers (FELs), as it combines the high quantum efficiency (QE) of a semiconductor photocathode with durability that approaches that of some metals [155, 1, 132]. High QE is particularly important for high average current applications where the power demanded of the UV driving laser may be impractically large for metal photocathodes. At 260 nm (4.7 eV), where Cs-Te is commonly used, the QE is reliably in excess of 10% compared to 10^{-5} - 10^{-4} for copper [124]. The durability of Cs-Te has been measured through its operational lifetime, which is routinely in the hundreds of hours in high charge RF photoinjectors [69, 164, 28]. Some Cs-Te photocathodes have been successfully used for over 100 days in a photoinjector with minimal degradation of the QE [20]. Besides traditional photocathode applications, these properties have caused thin films of Cs-Te to be investigated for activating GaAs photocathodes [10, 9, 80, 135] as well as for use in superconducting RF photoinjectors [168, 162, 165].

In spite of its success in terms of durability and QE, Cs-Te's modest mean transverse energy (MTE) in the UV can limit achievable photoinjector emittance. Most measurements place the MTE of Cs-Te at 260 nm (4.7 eV) between 150 meV and 300 meV [100, 132, 148, 165]. While this MTE is acceptable for present high repetition rate, soft x-ray FEL injectors, planned upgrades to existing facilities such as LCLS-II HE have an emittance requirement as low as ~100 nm at ~100 pC bunch charge, and may directly benefit from reduced intrinsic emittance. [86, 121]. Driving photocathodes near threshold is a well known strategy in reducing their MTE at the cost of QE. Dowell and Schmerge [39] showed that

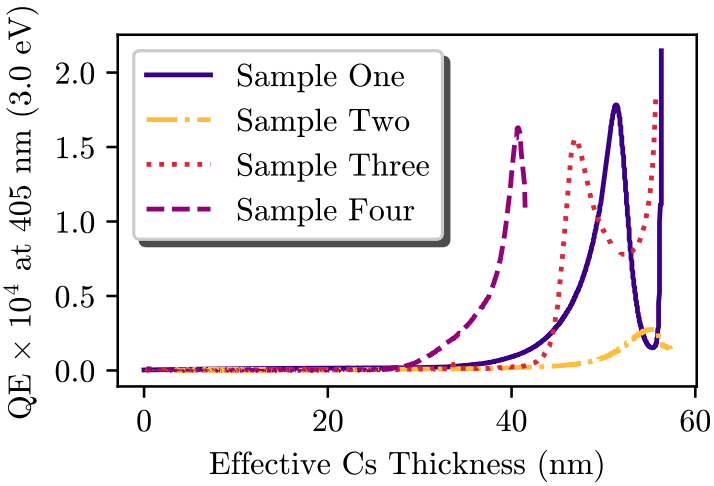

Figure 3.1: Sequential deposition growth of Cs-Te photocathodes. Samples one and three (cesium rich) were grown until a peak was observed in the QE and then deposition was continued to a second peak. In samples two and four (low cesium), deposition was stopped at the first peak.

the three step model predicts a linear rise in MTE with respect to photon energy for ideal photocathodes and the MTE for near threshold photoemission has been shown to be limited by temperature in some cases (MTE = $k_B T$) [46, 75, 29]. This motivates the present measurement of the MTE of Cs-Te near threshold at both room and cryogenic temperatures.

Cs-Te photocathodes, for which the bulk of photoemission comes from Cs_2Te, often exhibit a "shoulder" in their spectral response that consists of low QE ($< 10^{-5}$) photoemission at visible wavelengths. Excess Cs was blamed for the shoulder throughout the 1960s based on photomultiplier tube measurements [154, 26, 27]. However, Fisher et al. [53] and later Powell et al. [131] contradicted this claim and argued that another phase of Cs_xTe other than Cs_2Te must be present in the cathode along with elemental Cs. They found that the shoulder vanished when adding Cs followed by heating and failed to decrease when Te was deposited along with more heating which should have reacted

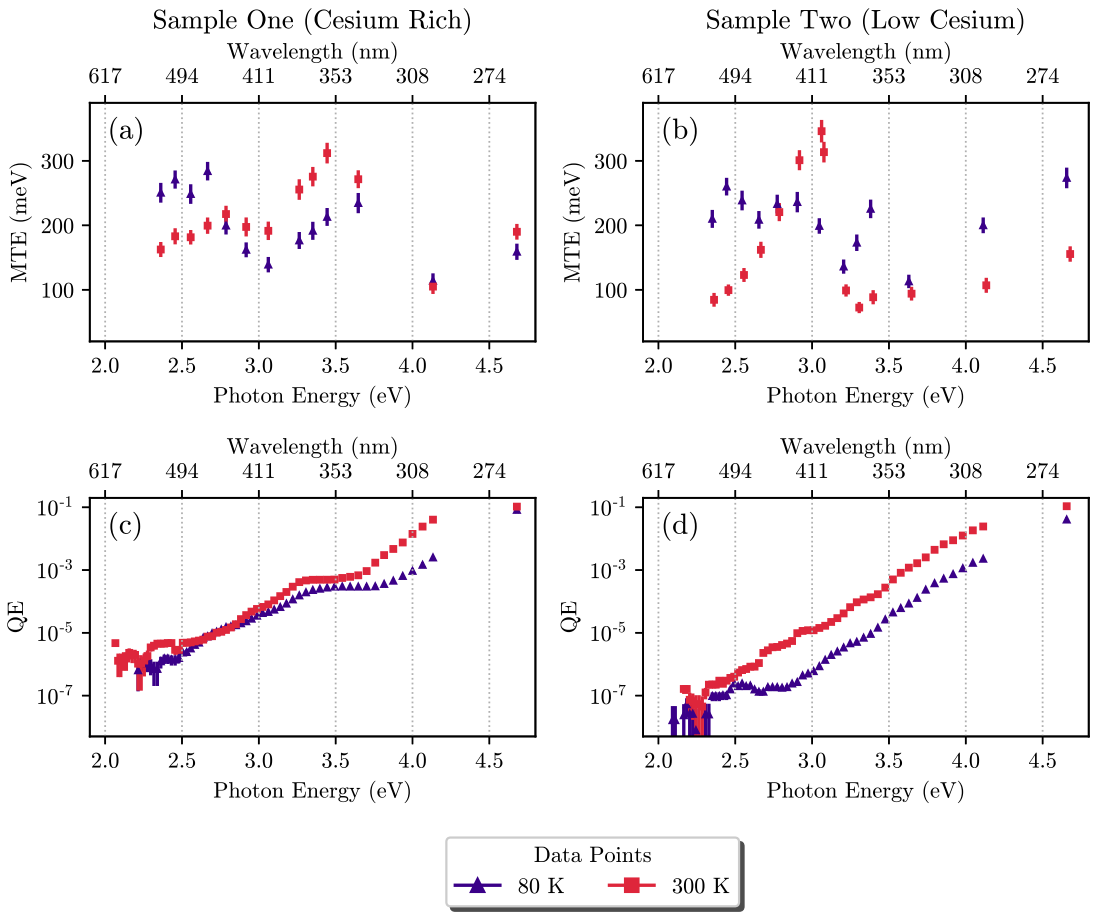

Figure 3.2: The QE and MTE of sample one (panels a and c) and sample two (panels b and d). Measurements were taken at room temperature (red squares) and with the instrument's sample holder filled with liquid nitrogen (blue triangles).

the excess Cs into Cs_2Te. Additional data from UV photoemission spectroscopy failed to line up with that of elemental Cs or elemental Te alone [131].

Direct confirmation of a second phase of Cs_xTe that coexists with Cs_2Te first came from x-ray diffraction data which identified that phase as Cs_5Te_3 [30]. However, a lack of photoemission measurements prevents confirmation that this phase is correlated with observed photoemission properties. Later work using Auger electron spectroscopy (AES) and x-ray photoemission spectroscopy (XPS) during the growth of Cs-Te photocathodes identified impurities of the

form Cs_xTe with $x = 1.2$ and $x = 0.9$ [99, 98]. Recently, real time in-situ x-ray characterization of Cs_2Te growth was also able to observe the production of a Cs_xTe in their photocathodes, but found that it could be eliminated in diffraction measurements by using a codeposition growth technique [58]. However, x-ray fluorescence spectra of the codeposited samples indicated that the photocathode was not fully stoichiometric Cs_2Te [58].

In this paper, we present measurements of the MTE of Cs-Te photocathodes for near threshold photoemission. First, our growth technique is discussed and results of our measurements are presented for both room and cryogenic temperatures. We observe a sharp increase in MTE as the driving laser's wavelength approaches the photoemission threshold of pure Cs_2Te. Two models are posited which help to explain this behavior as pollution of the photoemitted electron distribution by emission from low workfunction compounds present alongside Cs_2Te. Our results indicate the need for phase-pure Cs_2Te photocathodes in order to achieve the low near threshold MTE desired for future accelerator physics applications.

3.3 Cathode Growth and Characterization

Two Cs-Te photocathodes were grown with sequential deposition on commercial Si substrates: one which is expected to be representative of typical growth procedures (here, called "sample one" or "cesium rich" growth) and one where the growth was terminated early to reduce the level of cesium on the surface ("sample two" or "low cesium" growth). The substrates were both cleaned at 600 °C for 12 hours under ultra high vacuum and then held at ~120 °C while a

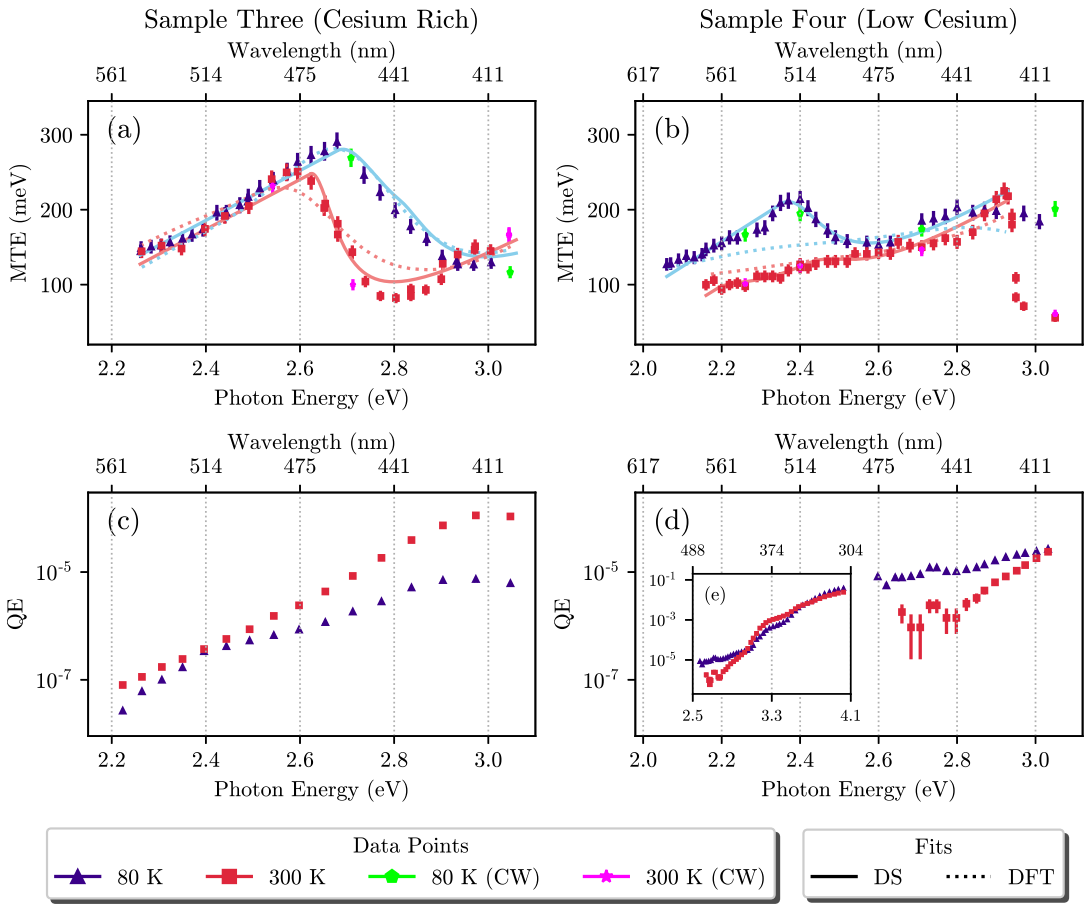

Figure 3.3: The QE and MTE of samples three (panels a and c) and four (panels b, d, and e) at room temperature (red) and liquid nitrogen temperatures (blue). MTE was also measured at select wavelengths using CW light sources (lime pentagons and fuchsia stars). Lines of best fit for three components with Dowell-Schmerge MTE ("DS") and MTE computed using DFT ("DFT") are shown. Not included are additional points taken in the UV: The QE of sample three was 15% at 260 nm / 4.7 eV (room temp.). Sample four had a QE of 10% (room temp.) and 23% (cryo. temp.) at 260 nm / 4.7 eV. The MTE of sample three at 260 nm / 4.7 eV was (170 ± 19) meV (300 K) and for sample four was (263 ± 24) meV (300 K), (173 ± 20) meV (80 K). At 343 nm / 3.6 eV the MTE of sample four was (43 ± 9) meV (300 K) and (63 ± 11) meV (80 K).

20 nm layer of tellurium was deposited (chosen to be a common thickness used in photoinjector facilities). The QE at 405 nm (3.0 eV) was monitored while cesium was evaporated into the chamber as in Fig. 3.1. For sample one, evaporation was terminated after the QE reached a second peak. For sample two, the

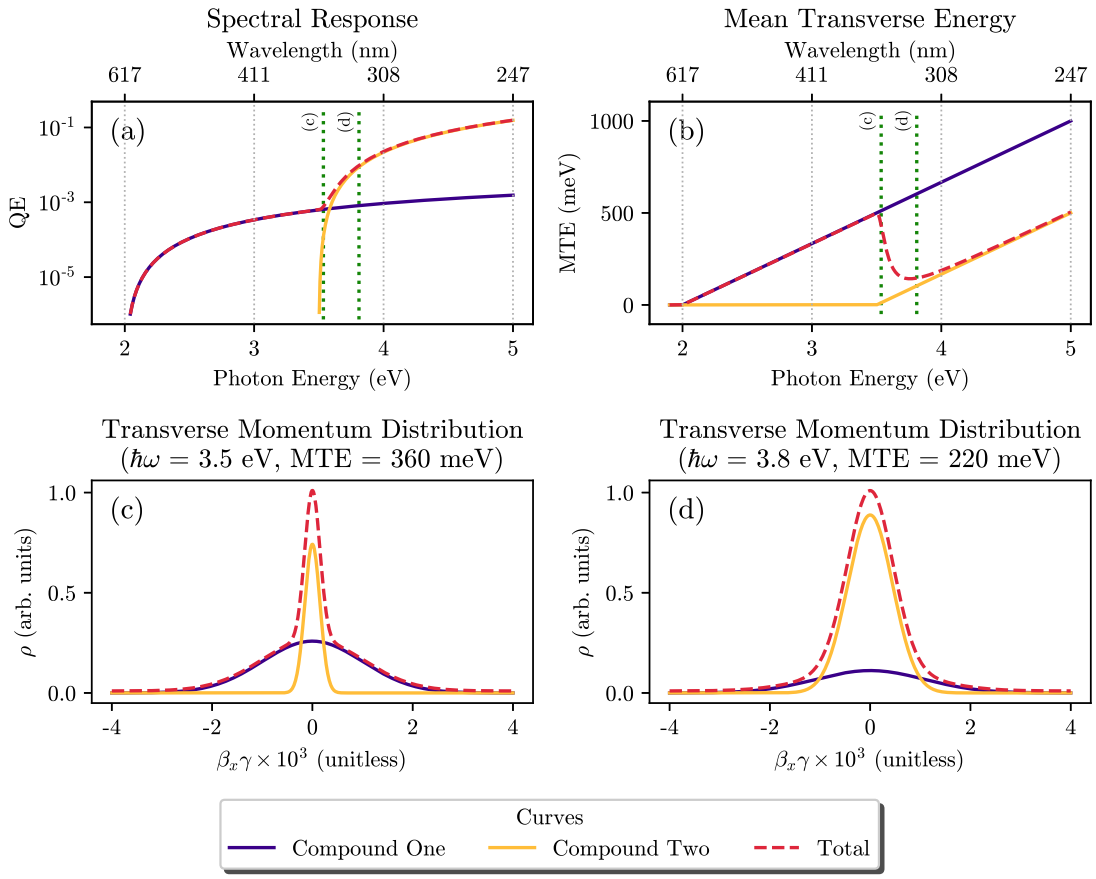

Figure 3.4: The effect of multiple compounds with different photoemission threshold on MTE. In this example, the sample is weighted to be 0.1% compound one and 99.9% compound two. Both are modeled using Eqs. 3.2 and 3.3 with the totals calculated using Eq. 3.1. The QE and MTE of each component as well as the combined results are shown in panels a and b. The transverse momentum distribution sampled at two different photon energies is shown in panels c and d. It can be clearly seen how even small amounts of a low threshold compound may "pollute" the transverse momentum distribution and inflate the low MTE of the second compound near its threshold.

deposition was stopped at the first peak in QE at 405 nm (3.0 eV). The reported "effective Cs thickness" is derived from a quartz crystal microbalance and may have varying accuracy with process parameters. It is used here only to illustrate the growth procedure.

Both samples were transferred into the MTE meter described in Ref. [84] and

their QE was measured at room temperature and ~80 K, using liquid nitrogen, as shown in Fig. 3.2. MTE was measured as a function of wavelength using the voltage scan technique with a cathode voltage that ranged from −3 to −10 kV. Uncertainty in the measurements is shown as the vertical bars in the plot or, when not visible, is smaller than the data points shown. Both measurements were made with the cathodes illuminated by a monochromated arc-lamp based light source. At long wavelengths, measurement of the MTE was hindered by the low QE of the photocathodes and the low power of the light source used.

To better investigate the non-monotonic behaviour of the photocathodes at visible wavelengths, another set of samples was grown using the typical procedure ("sample three") and early termination ("sample four"). MTE and QE were measured using an NKT Photonics SuperK Extreme monochromated supercontinuum light source, with comparatively greater power. This data is plotted in Fig. 3.3. Additional points at short wavelength were collected using the arc-lamp based light source, the third harmonic of an Amplitude Systems Tangerine fiber laser (343 nm or 3.6 eV) and a set of UV LEDs. The low energy nature of the voltage scan measurements and the pulsed output of the supercontinuum light source makes this data susceptible to the effects of space charge. Additionally, high intensity illumination on the cathode may cause multiphoton photoemission which affects the MTE [8]. We confirm that these sources of error are avoided by checking for agreement with measurements at select wavelengths using low intensity (but similar average power to the supercontinuum light source) CW diode lasers (plotted in Fig. 3.3).

3.4 Modeling the Near-Threshold MTE

The non-monotonic behaviour of Cs-Te's MTE suggests that multiple compounds contribute to photoemission for wavelengths below the threshold of Cs_2Te. Because the MTE is the variance of the momentum distribution of the electrons off the cathode, the MTE of a combined distribution (here, from multiple photoemitting materials) will be a weighted sum of individual MTE's, where the weights are determined by the QE and abundance of each source. We express this as,

$$\mathrm{MTE}(\hbar\omega) = \frac{\sum_i w_i \mathrm{QE}_i(\hbar\omega)\mathrm{MTE}_i(\hbar\omega)}{\sum_i w_i \mathrm{QE}_i(\hbar\omega)}, \tag{3.1}$$

where the index i runs over all of the components of the photocathode and the weights w_i account for the prevalence of each component. For a two (or more) compound system where the QE is dominated by the higher workfunction material at high photon energies, the MTE will be set by the lower threshold material at low photon energies and by the higher threshold material at high energies. This may lead to non-monotonic behaviour even when the MTE of each individual compound only rises with excess energy. A schematic of how this can happen is shown in Fig. 3.4.

For simplicity, we consider emission from multiple compounds (and crystalline orientations) with an assumed step function electron occupation, where their MTE and QE are given by the analytical expression due to Dowell and Schmerge [39]. The QE in the absence of reflectivity and scattering is given by

$$\mathrm{QE} = \frac{E_f + \hbar\omega}{2\hbar\omega}\left(1 - \sqrt{\frac{E_f + \phi}{E_f + \hbar\omega}}\right)^2, \tag{3.2}$$

and the MTE is

$$\mathrm{MTE} = \frac{\hbar\omega - \phi}{3}, \tag{3.3}$$

where E_f is the Fermi energy, $\hbar\omega$ is the photon energy, and ϕ is the workfunction. The free parameters are: the workfunctions of each component at each temperature (ϕ_i (80 K) and ϕ_i (300 K)), the component's Fermi energies ($E_{f,i}$), and the relative contribution of each component to the total photoemission. The workfunction is assumed to encompass a ~15 meV shift in the photocathode's threshold due to Schottky lowering in the instrument's 0.1 to 1 MV m^{-1} extraction field. The temperature dependence in this model is dealt with by a change in the workfunction of each material as a function of temperature which is known to occur from expansion of the crystal lattice [146] or from a surface dipole due to adsorption of molecules on the cooled surface.

A minimum of three components is needed to reproduce the experimental data. These can be attributed either to different compounds or to different crystalline orientations, since the workfunction of a material may also depend on the particular crystal face. Our parameters of best fit are listed in Tab. 3.1 and the predicted MTE as a function of temperature and photon energy is shown along with the underlying data in Fig. 3.3. In sample two, we only fit data at high temperature below a photon energy of 2.95 eV (418 nm) because the sudden drop in MTE observed there is likely due to the onset of photoemission from another compound which we do not consider here or possibly from the Cs_2Te itself which has a bandgap energy of the same value [131]. We do not place great physical significance on the Fermi energies returned by the fitting procedures, which are large in some cases. In the context of the Dowell-Schmerge formulas, the Fermi energy only shows up in the expression for QE and only affects a small change in the MTE of the multiple components model. Additionally, we are fitting a model designed principally for metals to a sample that may include semiconductors where the QE will also depend on band structure parameters.

We are motivated to consider the particular impurities Cs_5Te_3 and Cs from the direct evidence of their presence with Cs_2Te from diffraction data and AES/XPS data. We consider their photoemission properties in the context of the three step model. The electronic band structures of Cs and Cs_5Te_3 were calculated numerically using the density-functional theory (DFT) code JDFTx [153], GBRV ultrasoft pseudopotentials [59], and GGA-PBEsol exchange correlation functional [119]. The calculations used a plane-wave cutoff of 544 eV and a Brillouin zone sample mesh of 6x6x6. The lattice of Cs_5Te_3 was taken from powder x-ray diffraction data [142] and structural relaxation was performed before the electronic calculations. An optimal value of the lattice constants for the monoclinic crystal was found to be $a = 4.03\,\text{nm}$, $b = 1.35\,\text{nm}$, $c = 2.85\,\text{nm}$, and $\beta = 135.0°$. For both compounds, a set of maximally localized Wannier functions [92] (5 for Cs and 41 for Cs_5Te_3) was used to capture the band structure in a region ~6 eV wide surrounding the Fermi energy using the Wannier interpolation method [91].

Given the numerical band structure, a surface orientation, and workfunction, the probabilities of the three step model and therefore the desired photoemission properties may be calculated using the method described in Ref. [105]. The rate of direct transitions between states in the band structure is given by Fermi's golden rule weighted by the probability of the initial state being occupied and the final state being unoccupied. For the sake of simplicity, the Cs_5Te_3 is assumed to be undoped with the Fermi level in the middle of the bandgap. For a crystalline orientation whose surface has the normal vector $\vec{r}_s$, we require electrons excited to a final state with crystal momentum $\vec{k}_f$ to satisfy the condition

$$\vec{k}_f \cdot \vec{r}_s > 0, \tag{3.4}$$

if they will be transmitted to the surface in the absence of scattering. The electrons will escape from the crystal as long as their final state energy is large enough to satisfy the condition

$$T_\perp = E_{\vec{k}_f,b} - \frac{\hbar^2}{2m_e}|\vec{k}_{f,\parallel}|^2 - \phi > 0, \tag{3.5}$$

where $T_\perp$ represents the kinetic energy of an electron in a direction perpendicular to the surface once in vacuum. A weighted average of the escape probability and transverse energy of escaping electrons is computed for all direct transitions in the first Brillouin zone using a Monte-Carlo integrator to obtain the QE and MTE.

The weights of compounds, weights of crystal orientations, bandgap temperature dependence of Cs_5Te_3, and workfunctions of each compound were fit to the photoemission data using derivative-free global optimization [110]. The parameters of best fit for both samples are reported in Tab. 3.2 and the best fit curves are shown in Fig. 3.3. The sign of the work function's temperature dependence points to adsorption as a likely cause. The failure of the model to match the qualitative behaviour of the low temperature data in sample four could be due to us not accounting for all orientations of the compounds that are present. The Cs_5Te_3 could also be severely disordered, or other impurities may be present.

3.5 Conclusion

In this letter we have reported measurements of the MTE of Cs-Te for near threshold photoemission and at cryogenic and room temperatures. Our analysis of the measurements has shown that the near threshold behaviour of the

Table 3.1: The parameters of best fit for the multiple component model with Dowell-Schmerge photoemission formulas.

Parameter	Sample 3	Sample 4
Weight One	1%	5%
Weight Two	61%	88%
Weight Three	38%	7%
Workfunction One (80 K)	1.8 eV	1.8 eV
Workfunction Two (80 K)	2.9 eV	2.3 eV
Workfunction Three (80 K)	2.8 eV	2.4 eV
Workfunction One (300 K)	1.8 eV	2.0 eV
Workfunction Two (300 K)	3.4 eV	2.4 eV
Workfunction Three (300 K)	2.7 eV	2.2 eV
Fermi Energy One	4.9 eV	11.9 eV
Fermi Energy Two	5.5 eV	10.4 eV
Fermi Energy Three	4.2 eV	2.1 eV

photocathodes may be explained by emission from multiple compounds that emit below the threshold of pure Cs_2Te. Historical measurements suggest that the likely identity of the low workfunction compounds in Cs-Te are metallic Cs and the semiconductor Cs_5Te_3 which is known to show up in samples with a similar ratio of Cs and Te to what is used for photocathode growth. We were able to model the below threshold behaviour of the photocathodes by assuming that multiple compounds contribute to emission each of which is well described by the Dowell-Schmerge expressions for MTE and QE. Taking the compounds to be Cs and Cs_5Te_3 and computing their photoemission properties numerically, we were able to achieve good subjective agreement with the data in almost all cases.

Photoemission from the additional compounds may also help explain the measurement of two-photon photoemission at 800 nm (1.5 eV) reported in Ref. [116]. In that study, photocurrent was measured as a function of pulse

Table 3.2: The parameters of best fit for photoemission modeled with numerically computed band structures.

Compound	Parameter	Sample 3	Sample 4
Cs	Compound Weight	0.1%	3%
	[100] Surface Weight	30%	0%
	[110] Surface Weight	0%	0%
	[111] Surface Weight	70%	100%
	[100] Workfunction (80 K)	1.68 eV	-
	[110] Workfunction (80 K)	-	-
	[111] Workfunction (80 K)	2.03 eV	2.90 eV
	[100] Workfunction (300 K)	1.60 eV	-
	[110] Workfunction (300 K)	-	-
	[111] Workfunction (300 K)	1.95 eV	2.06 eV
Cs_5Te_3	Compound Weight	99.9%	97%
	Bandgap (80 K)	1.17 eV	1.12 eV
	Bandgap (300 K)	1.15 eV	1.20 eV
	[100] Surface Weight	88%	92%
	[110] Surface Weight	1%	8%
	[111] Surface Weight	11%	0%
	[100] Electron Affinity (80 K)	1.12 eV	1.26 eV
	[110] Electron Affinity (80 K)	1.08 eV	0.83 eV
	[111] Electron Affinity (80 K)	1.08 eV	-
	[100] Electron Affinity (300 K)	1.04 eV	1.28 eV
	[110] Electron Affinity (300 K)	0.98 eV	0.85 eV
	[111] Electron Affinity (300 K)	1.00 eV	-

energy under illumination with an ultrafast 800 nm (1.5 eV) light source. It was observed that emission scaled quadratically with pulse energy instead of the expected cubic dependence if the sample was pure Cs_2Te and had a threshold in the UV. The anomalous two photon photoemission may be explained if the electrons were being emitted from the low workfunction compounds observed here rather than the pure Cs_2Te assumed in the paper.

Low threshold compounds that are present alongside a high workfunction

photocathode may present a barrier to achieving low MTE even when those compounds are present in trace amounts. These compounds may show up as a shoulder in the cathode's spectral response. Indeed there are other alkali tellurides that have low level photoemission at long wavelengths similar to what we see in Cs-Te [154, 156]. Use of this family of photocathodes will likely require research into methods of growing phase pure samples. Some promising results are already coming from this area with reports that codeposition growth of Cs-Te is able to produce a more pure photocathode than the sequential deposition growth studied in this work [58]. Further studies on the near threshold MTE of photocathodes grown with this procedure and of other alkali metal photocathodes with a photoemission shoulder may be warranted.

CHAPTER 4

THERMALIZED CONDUCTION BAND ELECTRONS AS A SOURCE OF BRIGHT BEAMS

This chapter was originally published as reference [120][1].

4.1 Abstract

Low effective mass semiconductor photocathodes have historically failed to exhibit the sub-thermal mean transverse energies (MTEs) expected of them based on their band structure. However, conservation of transverse momentum across the vacuum interface, and therefore a low MTE in these materials, has been observed in time resolved ARPES. To help bridge this gap, we measured the MTE of the pump probe photoemitted electrons seen in the ARPES experiment using methods typical of accelerator physics. We compare the results of these measurements with those of both communities and discuss them in the context of photoemission physics.

4.2 Introduction

The discovery of new low MTE photocathodes is a requirement for those seeking to improve the brightness of photoinjectors operating at the charge extraction limit. In photoinjectors with a fixed electric field there is a minimum initial

[1]The following acknowledgment appeared in the original manuscript: This work was supported by the U.S. National Science Foundation under Award PHY-1549132, the Center for Bright Beams.

spot size $\sigma_{x,\mathrm{min}}$ for every bunch charge due to the virtual cathode instability. This is called the charge extraction limit. Since the charge extraction limit sets a maximum charge density in the spatial coordinate and cathode MTE sets the density in the momentum coordinate, the maximum brightness can be written as $B_{4\mathrm{D,max}} \propto (\sigma^2_{x,\mathrm{min}}\mathrm{MTE})^{-1}$. The only way to improve the brightness of photoinjectors operating at or near $\sigma_{x,\mathrm{min}}$ is to drive down the MTE of photocathodes.

4.2.1 Low Effective Mass Semiconductor Photocathodes

Low effective mass semiconductors offer a promising path towards new low MTE photocathodes. Conservation of transverse momentum across the photocathode's surface means that the transverse energy of electrons is scaled by the mass ratio m_e^*/m_e upon emission. For near threshold photoemission from a negative electron affinity (NEA) photocathode, the transverse energy of electrons comes from the Fermi tail and is k_BT. The MTE is then $(m_e^*/m_e)k_BT$ and makes us interested in candidate photocathodes with small m_e^*. Some semiconductors, such as GaAs, have an effective mass ratio as small as $m_e^*/m_e = 0.07$ and should have MTEs as low as 1.7 meV for near threshold photoemission at room temperature [159]. Compare this with the MTE of polycrystalline copper, a commonly used metallic photocathode, which has been measured at 85 meV near threshold [68].

The MTE of NEA GaAs near threshold has been consistently measured at more than 25 meV which is k_BT at room temperature [118, 112, 21, 40, 166, 15]. There is only one reported measurement of the expected 1.7 meV MTE and it has not been reproduced since [89]. There is currently no consensus on why the

MTE is so much larger than what the material's low effective mass would lead us to believe. Some proposed explanations include physical/chemical roughness of the surface, scattering of electrons in the Cs overlayer, and the effects of electron-phonon scattering [60, 106, 159].

The narrow dispersion of the GaAs conduction band is observed in time resolved ARPES (trARPES). In a trARPES measurement, electrons are excited into empty conduction band states by pump photons and emitted into the vacuum some time later with probe photons. These photoelectrons are filtered by angle of emission and longitudinal energy in a hemispherical analyzer. Kanasaki et al. measured a photoelectron distribution from GaAs which can be naively converted to a transverse energy distribution with 1.7 meV MTE [73]. Photoinjectors, however, do not have the energy filtering capabilities of an ARPES style detector. An accurate measurement of MTE for these applications must include the full photoelectron distribution, not a narrow subset of it.

4.3 Measurements of the Out of Equilibrium Photocathode

The photocathode was prepared by solvent cleaning and etching a p-type GaAs (110) wafer obtained from a commercial source. The wafer was Zn doped to a p-type carrier concentration of 10^{19} cm^{-3} and came polished to a surface roughness of better than 0.4 nm RMS. Before introduction to a vacuum chamber at better than 10^{-10} Torr pressure, the wafer was cleaned in acetone and etched in a 1% HF solution for 30 s. Inside the preparation chamber, the sample was annealed at 550 °C for 8 hours to remove surface oxides. The band gap was measured at 1.40 eV using photoluminescence spectroscopy with illumination at 633 nm. We

estimate the workfunction of the sample to be 4.6 eV based off of measurements of quantum efficiency (QE) as photon energy was changed. The data, in Fig. 4.1, was fit to a model with quadratic dependence of QE on excess photon energy.

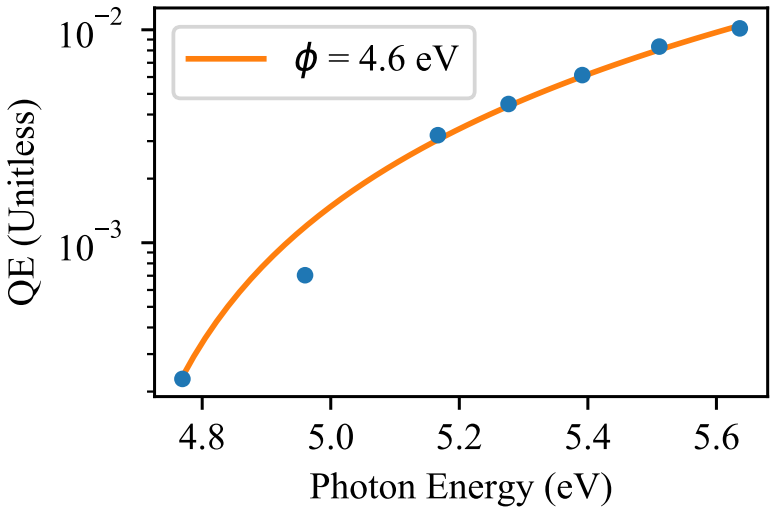

Figure 4.1: Quantum efficiency (QE) as a function of photon energy for the GaAs (110) sample. Photocurrent was measured at five intensities for each photon energy to accurately determine the QE and to ensure there was no multiphoton photoemission. A quadratic model, shown in orange, was fit to the data with workfunction (ϕ) as a fit parameter. The fit value of the workfunction was ϕ = 4.6 eV.

An optical parametric amplifier was used to generate the 750nm pump and some of the 1030 nm output of an Yb fiber laser driving it was diverted and frequency tripled for use as the probe. Both were overlapped at the sample and aligned in time of arrival. The intensity of the pulses was increased to the point that each caused multiphoton photoemission from the sample and those multiphoton beams were used to center the laser spots on the cathode and align them with each other. The cross correlation of the pulses was measured as less than 400 fs full width at half maximum by watching the coherent enhancement of multiphoton photoemission as the time delay of the pulses was varied.

4.3.1 Yield and Carrier Diffusion

We measured photocurrent as a function of pump probe delay and confirmed the presence of long lived carriers in the conduction band of the sample. Our measurement is shown in Fig. 4.2. The time axis is signed so that there is positive delay when the probe comes after the pump. Coherent multiphoton photoemission is seen in the few hundred femtoseconds around $\Delta t = 0$. Incoherent multiphoton photoemission follows that at positive values of Δt and extends beyond 100 ps. The number of electrons emitted in this process is proportional to how many excited carriers remain in the region of photoemission after the pump probe delay.

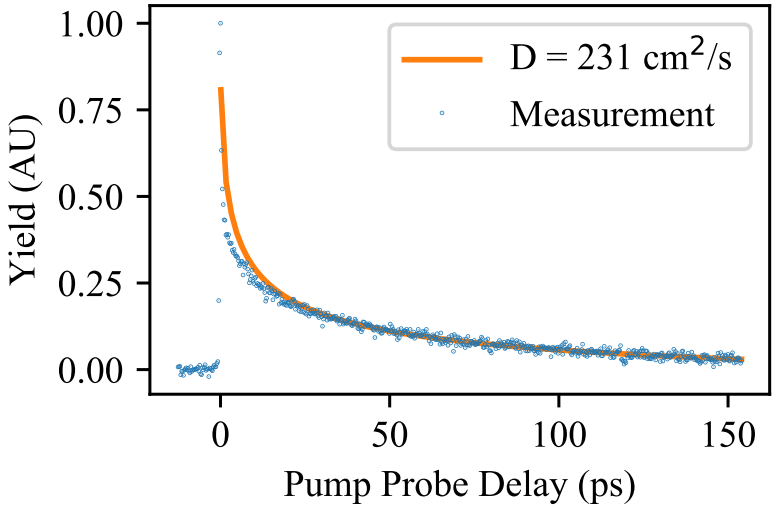

Figure 4.2: In blue, measurements of photocurrent are displayed as pump probe delay (Δt) is changed. The large peak at $\Delta t = 0$ is due to the coherent enhancement of multiphoton photoemission from the pump and probe. The long tail afterwards is 1+1 photoemission of electrons being excited into the GaAs conduction band. The curve in orange is a model including carrier recombination and diffusion with a fit value of the diffusion constant. We found an optimal value of the diffusion constant to be 231 cm^2/s. Values of the absorption length for the pump and probe are from the Handbook of Optical Constants of Solids [113]. A constant multiphoton background was subtracted from the signal and the result normalized to a peak value of one before fitting.

The time dependence of the yield curve is not explained by carrier recombination alone and an accurate description needs to include the effects of carrier diffusion. The minority carrier lifetime of p-type GaAs is 4 ns [109] and one would naively expect the lifetime of the 1+1 photoemission signal to be similar. Modeling the system to include the 1D diffusion of electrons away from the surface gives a more accurate time dependence when using literature values of the diffusion constant and of the absorption lengths for the pump and probe photons. The yield measurement as well as a fit with the diffusion constant as the free parameter are shown in Fig. 4.2. The fit value of the diffusion constant was 231 cm^2/s compared to other works which found it to be 200 cm^2/s [140].

4.3.2 Mean Transverse Energy

The MTE of the out of equilibrium photocathode was measured at 200 meV for large pump probe delays. Voltage scan measurements were performed using voltages between 2 kV and 10 kV as the pump probe delay was increased in 200 fs steps away from the overlap position up to a maximum delay of 20 ps. A custom microchannel plate and scintillator based detector was coupled with an intensified CCD camera to measure the size of the low current beam. Before MTE measurements were performed, the intensity of the pump and probe were decreased to the point that no multiphoton photoemission from the individual pulses was seen in beam images at negative pump probe delays. A 100 µm diameter pinhole in the path of the probe was imaged onto the cathode with unity magnification. The MTE, shown in Fig. 4.3 as a function of pump probe delay, relaxes on a picosecond timescale from nearly 400 meV in the overlap region to 200 meV at large delays. There was an asymmetry in the MTE measurement

between the X and Y projected values on the scale of 4% which is attributed to an artifact of performing a measurement of such a large MTE in an instrument designed for studying low MTE photocathodes.

We repeated the time resolved MTE measurement as the intensity of the pump and probe were varied with no change in MTE at large delays. Multiphoton excitation within the individual pump and probe pulses could inflate the observed MTE by exciting electrons into unwanted states with large transverse energy. The rate of this process depends on intensity in a non-linear way which makes the MTE change with intensity if multiphoton excitation is present. We measured no change in the MTE as pump intensity was varied and only a small change in MTE, as shown in Fig. 4.4, during the coherent overlap when the probe intensity was changed. The bunch charge of the emitted pulse also depends on pump and probe intensity and the fact that the measured value did not change with bunch charge indicates that the measurement was not affected by space charge.

The measurements were performed as the pump wavelength was changed between 700 nm and 800 nm with no change in MTE. The GaAs L valley is only 300 meV above the Γ valley and so excitation with wavelengths of light shorter than 725 nm can transition electrons into states with large transverse momentum. As our pump wavelength crossed the 725 nm threshold there was no change in MTE at any pump probe delay. This is evidence that L valley electrons are not contributing to the large MTE measured.

Adsorbates are not a likely cause of the observed large MTEs because the measurements were replicated immediately following annealing and were uniform across the cathode. The cathode was annealed at 550 °C for 8 hours to

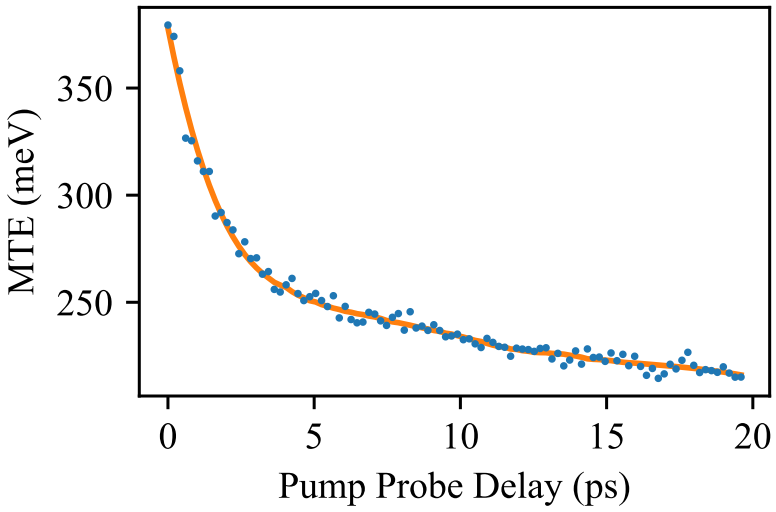

Figure 4.3: MTE of the pump probe photoemitted electrons as pump probe delay is changed. A smoothed curve, orange, is included to help guide the eye.

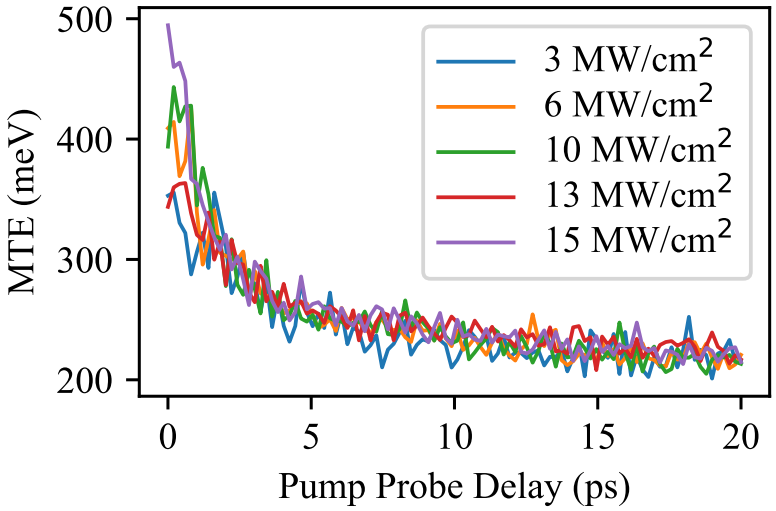

Figure 4.4: MTE as pump probe delay is changed at different probe intensity. Pump intensity was held at a constant 2 MW/cm^2. The MTE does change by a small amount, but only for delays where the pump and probe overlap each other.

remove adsorbates and immediately transferred to the MTE meter where measurements were performed within 15 minutes of shutting off the heater. The vacuum in the chamber was such that the time to form a monolayer of contaminants was several hours. Measurements were repeated in half hour increments

following transfer to the MTE meter with no change observed. The MTE was determined to be uniform across the cathode by repeating the time resolved measurement at ten different locations across the surface.

4.4 Discussion

We have measured the MTE of pump probe photoemission from the GaAs (110) surface to be two orders of magnitude larger than what the low effective mass argument would lead us to believe. Although the low effective mass dispersion was seen in trARPES, this does not contradict our new measurement. The trARPES experiment does not collect the full distribution of electrons emitted from the sample and there could be electrons outside of the narrow energy acceptance of the detector that contribute to a large MTE. We did observe relaxation of the transverse momentum distribution on a timescale that is longer than the overlap of the pump and the probe. This is likely thermalization of the electrons as they make their way to the bottom of their band by non-radiative transitions.

Estimates show that the dispersion of the GaAs (110) surface state is wide enough to be a potential cause of the larger than expected MTE we have observed. Ivanov et al. calculated the surface band structure of GaAs (110) and found it to have states immediately below the conduction band minimum of the bulk [71]. The probe used in our experiment has enough energy to emit electrons in these states and the wide dispersion of their band means that the photoelectrons can have large transverse momentum. These electrons would also have a small enough longitudinal momentum that they would not show

up in the trARPES experiment which only focused on emission from the conduction band. Confirmation of this theory would require an angle and energy resolved measurement of the full electron distribution.

CHAPTER 5

NONLINEAR PHOTOEMISSION ENHANCEMENT WITH NANOPATTERNED CATHODES

This chapter has been submitted for publication and is currently available as the preprint [123][1].

5.1 Abstract

Metal photocathodes are an important source of high brightness electron beams, ubiquitous in the operation of both large scale accelerators and table-top microscopes. When the surface of a metal is nano-engineered with patterns on the order of the optical wavelength, it can lead to the excitation and confinement of surface plasmon polariton waves. In this work, we demonstrate the use of plasmonic nanogrooves on gold photocathodes to obtain a tenfold enhancement in the efficiency of fourth-order photoemission with respect to the linear process. These cathodes reached sustained average currents in excess of 100 nA, and optical intensities larger than 2 GW cm^{-2} with no degradation of performance. A procedure for high precision fabrication of these cathodes is described in order to obtain repeatable performance. Multiple nano-structured surfaces are characterized, both optically and in electron yield, and show excellent agreement

[1]The following acknowledgment appeared in the original manuscript: C.M.P. acknowledges US NSF Award PHY-1549132, the Center for Bright Beams and the US DOE SCGSR program. D.F. acknowledges support from the Office of Science, Office of Basic Energy Sciences, of the U.S. Department of Energy, under Contract No. DE-AC02-05CH11231. Work at the Molecular Foundry was supported by the Office of Science, Office of Basic Energy Sciences, of the U.S. Department of Energy, under Contract No. DE-AC02-05CH11231. D.B.D. and A.M.M. acknowledge support from NSF Science and Technology Center on Real-Time Functional Imaging (STROBE) under Grant No. DMR-1548924, which included funds for building the laser transport line in the DC photoemission test stand used in this work.

with their designed properties. Finally, the brightness of the extracted electrons is analyzed by measurements of the cathode's mean transverse energy and the asymmetry we observe is explained in terms of roughness and compared with numerical calculations. These results demonstrate the use of nano-engineered surfaces as enhanced photocathodes, providing a robust, air-stable source of high average current electron beams with great potential for industrial and scientific applications.

5.2 Introduction

High brightness electron sources for ultrafast applications require prompt emission of high-charge electron beams and direct injection into areas of extreme electromagnetic field amplitudes. Photoemission from metal surfaces has been the primary means of electron bunch generation, used by the large majority of user facilities around the world [155, 1, 132], owing to their fast response time and robustness. Despite their broad use, metal cathodes have a few major disadvantages. First, the typical quantum efficiency for a metal exhibits values in the 10^{-5} region which, for high charge pulse extraction, requires laser pulse intensities close to the damage threshold of the material. With time and continuous operation, this has been shown to lead to partial ablation, increased surface roughness, and reduced brightness [4]. High intensities may also cause multi-photon absorption and photoemission, leading to the generation of unwanted halos, and an overall increase of beam thermal emittance [8]. Furthermore, a typical metal work function requires UV photons for linear photoemission. The two-stage UV conversion from the initial infrared laser pulses has a substantial impact on the size and complexity of the photocathode laser system. It may

also impact the quality of the final pulse, resulting in substantial loss of energy, degradation of transverse pulse shape, and limited control over longitudinal profile. Altogether, the low quantum efficiency and the high work function effectively limit the maximum average current that can be extracted by metal cathodes and, therefore, the range of applications of the relevant instrumentation.

High quantum efficiency semiconductor films provide a possible path towards higher performance photocathodes. Depending on the choice of the material, the quantum efficiency can be orders of magnitude larger for a work function in the visible or infrared region [15]. Unfortunately, such cathodes are chemically reactive, and the vacuum levels found in high field photoinjectors often greatly complicate their use as high brightness electron sources. Further, dark current may become an issue in those same systems for materials with an extremely low work function.

Nonlinear photoemission may offer another potential solution to avoid nonlinear wavelength conversion. Depending on the material and laser parameters, it becomes more efficient to extract electrons from the cathode directly via multi-photon photoemission using infrared light, rather than perform wavelength conversion to the UV [102]. However, as is the case for linear photoemission, the small nonlinear yield of most flat metallic surfaces demands laser fluence values close to the material's damage threshold (typically on the order of 0.1 to 1 J/cm^2 [79]).

One path forward in improving the nonlinear yield of metals is by fabricating plasmonic structures by surface nanopatterning. Nanoscale grooves formed on a gold photocathode have been shown to increase its nonlinear yield at

800 nm by up to six orders of magnitude [127]. A similar concept using a grid of nanoscale holes showed a dramatic increase in the nonlinear yield of gold and copper photocathodes [87, 61]. On the other hand many questions remain open before such cathodes could be effectively considered as a reliable source for ultrafast application: Can we produce nano-engineered cathodes with repeatable properties? How does the mean transverse energy of the extracted beam depend on the nanostructures? Can such structures provide stable high average currents for extended periods with no degradation?

In this work we provide a detailed characterization of nanogroove array photocathodes that demonstrates understanding of both the engineering and the physical aspects of this advanced class of electron photoemitters. First, in Sec. 5.3 we discuss the theory of plasmonic nanogroove photocathodes. In Sec. 5.4 we explain the fabrication process, and confirm the design dimensions by direct measurements of their optical properties. Nonlinear photoemission measurements performed on a 20 keV electron gun are reported in Sec. 5.5. We find the non-linear photoemission coefficient for the nanostructured surfaces and are able to correlate its spread in values with the groove dimensions. We then confirm the polarization dependence of the photoemission, and perform continuous measurement of average currents in excess of 100 nA to verify the enhanced electron yield and the photocathode stability. Lastly, in Sec. 5.6 the mean transverse energy of the photocathode is characterized for different energies and the values found compared with the cathode's behaviour at the surface. The article then concludes by discussing future prospects for nanopatterned photoemitters.

5.3 Principles of Plasmonic Nanogroove Photocathodes

The ideal nanogroove cathode consists of a periodic array of trenches with depth, d, that extend infinitely in one direction and have nanometric width, w, in the other direction. Focusing for the moment on a single groove and imagining very large depth, light incident on the grooves may be coupled into modes within the gap that are best described by surface plasmon polaritons (SPP) within a metal-insulator-metal waveguide [83] (the vacuum is the insulator in this case). These SPPs require additional momentum to couple with free space illumination, owing to their dispersion relationship lying at larger wavevector for the same energy than the light line. For the case of the nanogrooves, the sharp edges at the entrance to the trenches can effectively provide such coupling [126]. The corner's profile contains high spatial frequency components that allow light to diffract around it and onto the plasmon dispersion curve.

The finite depth of the groove acts to form a resonant Fabry-Perot-like cavity with the allowable modes determined by d. The cavity depth that meets the resonance condition may be surprisingly small, only tens of nm for infrared light. This is explained by the fact that for the same energy, plasmons traveling along the walls of the gap may have an order of magnitude smaller wavelength than light in a vacuum [83]. The localization of optical energy to a nanometric region has the effect of field enhancement near the gap, which can exceed factors of one hundred and favor nonlinear photoemission.

Fig. 5.1a shows an example of local optical field enhancement by a nanogroove cathode computed using a finite difference time domain (FDTD) code. The simulated cathode had grooves 14 nm wide, with a pitch of 680 nm,

and was excited by light with a wavelength of 770 nm; representative of the cathodes studied in this paper. The same picture also shows the computed local variation of a static externally applied electric field.

The fact that emission occurs only at the sharp edges of the grooves may have an impact on the emittance of generated electron beams [87] and high local optical intensity can damage the gold surface[128]. However, the specific pattern used, the type and materials used during nano-fabrication, such as the sharpness of the pattern have an enormous impact on all of the above aspects.

The high quality factor (and narrow bandwidth) of the plasmonic nanogroove also has consequences on the photocathode response time. When the resonance bandwidth of the grooves is narrower than the bandwidth of the driving ultrafast laser, the field will continue to oscillate in the nanocavity longer than the duration of the excitation, effectively broadening the temporal response time of the cathode. An example of this effect was computed for the nanogroove array photocathode in Fig 5.1a by calculating the time-dependent field in response to excitation by ultrafast laser using an FDTD code (Lumerical [2]). The laser was 15 fs full-width-at-half-max (FWHM) and the calculated response of the structure was about 42 fs or a factor of three longer (Fig. 5.1b). The approximate bandwidth ($\Delta\lambda$) and peak absorption wavelength (λ) were 15 nm and 770 nm FWHM. An estimate of the optical time response can be calculated from time-frequency uncertainty as

$$\Delta t_{\text{Response}} = \sqrt{\Delta t_{\text{Laser}}^2 + (a_1 a_2 \lambda^2/(4\pi c \Delta\lambda))^2}, \tag{5.1}$$

where a_1 and a_2 are conversions from RMS to FWHM values of the absorption bandwidth and nanogroove time response respectively. Assuming Gaussian profiles, both a_1 and a_2 in Eq. 5.1 are approximately equal to 2.35, leading to a fi-

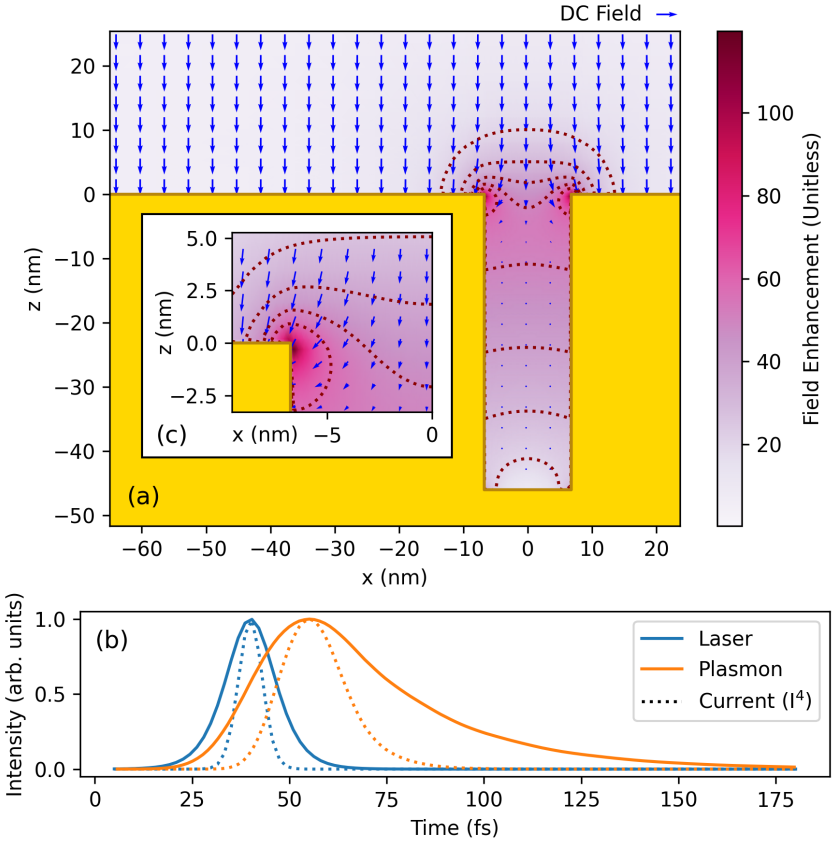

Figure 5.1: (a) Plot (with contours) of the field enhancement around a cross section of the nanogroove structure. Solution was computed with an FDTD code [2]. The DC accelerating field, computed independently using a finite difference code [96], is shown as the blue arrows. Inset (labeled c) shows a magnified view of the groove edge; (b) Time response of structure to a 15 fs excitation computed with FDTD (plasmon) compared with flat surface (laser). Estimated current profiles are shown as dotted lines.

nal cathode temporal response of ~50 fs FWHM. In order to obtain the extracted electron beam pulse duration, one would have to take into consideration the particular photoemission order used. In our case, the current density is proportional to the fourth-order of laser intensity, which suppresses the tails of the optical response and shrinks the final duration by a factor of two (for a Gaussian-like pulse). For ultrafast applications, other plasmonic cathode schemes that do not rely on resonant cavities may support higher bandwidths and allow use

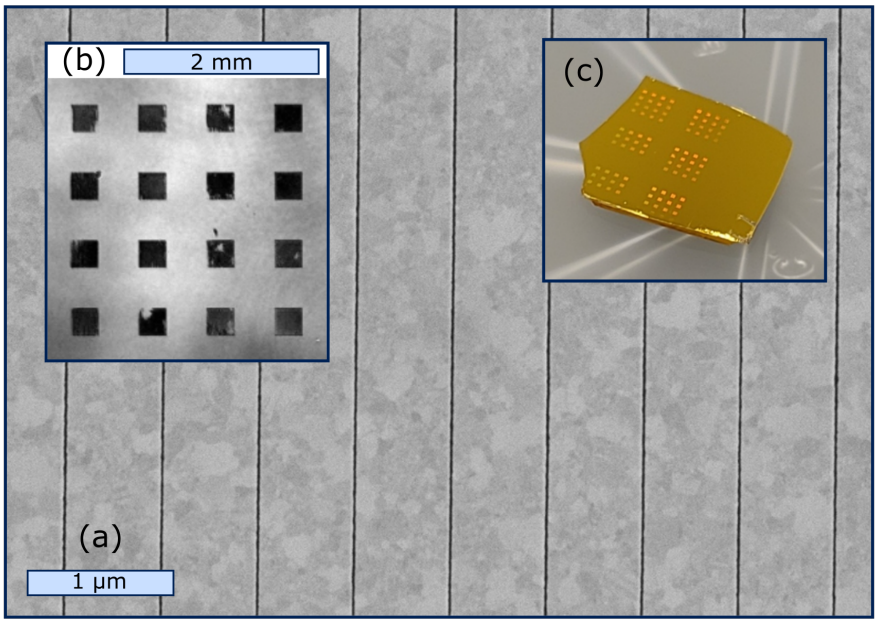

Figure 5.2: (a) Scanning electron micrograph of the nanopatterned cathode; (b) spatial image of reflectance of 16 plasmonic nanogroove photocathodes contained in a single square of the sample; (c) An image of the fabricated cathode.

with even shorter laser pulses [42].

5.4 Cathode Fabrication and Optical properties

Photocathodes were fabricated out of gold using the template stripping method [160, 129]. While plasmonic structures can be fabricated using other methods such as focused ion beam milling and the lift-off procedure, template stripping has been shown to yield superior surface roughness. Prior work has found RMS roughness of 0.2 nm RMS for template stripping compared to 1.4 nm for thermally evaporated metals [160]). A silicon wafer was UV/ozone cleaned for 5 minutes and spin coated with HSQ 2% resist. It was baked at 100 °C for 1 min and then patterned with electron beam lithography.

Cathodes with varying geometries are arranged in a square grids (a 4x4 pattern), and multiple grids are imprinted along a single wafer, with an edge-to-edge distance of about 1 mm (see Fig. 5.2b,c). The geometric dimensions of each of the 16 cathodes within a single square are varied, with a different groove pitch for each row, and a different width for each of the four columns. The groove width was varied in part by controlling the electron dose, leaving some calibration required for this dimension. The groove depth was fixed by the fabrication procedure at 50 nm. After exposing the resist, the template was cleaned using RIE oxygen plasma for 30 s and 150 nm of gold was deposited. UV curable epoxy was used to adhere a thin glass substrate to the gold and pressure caused this assembly (substrate, epoxy, and gold) to separate from the template revealing the nanopatterned cathode.

The quality of the fabrication was first verified by imaging the surface via scanning electron microscopy (Fig. 5.2a), and confirming the close match between the array dimensions and the target values. The most central square grid was then used for optical and photoemission measurement as it was the easiest to align along the axis of the photoemission setup.

We then performed reflectivity measurements, starting with near-IR imaging, of all the 16 patterns across the selected square in the sample. We used a 770 nm centered non-modelocked Ti:Sapphire laser oscillator as illumination source. The linear laser polarization was tuned to point in the direction across the grooves, while the laser pulse hit the cathode at normal incidence. As can be qualitatively seen in Fig. 5.2b, we observed strong suppression of the reflectivity in the regions that contain the nanopatterning.

The laser system was then mode-locked and its full bandwidth was used to

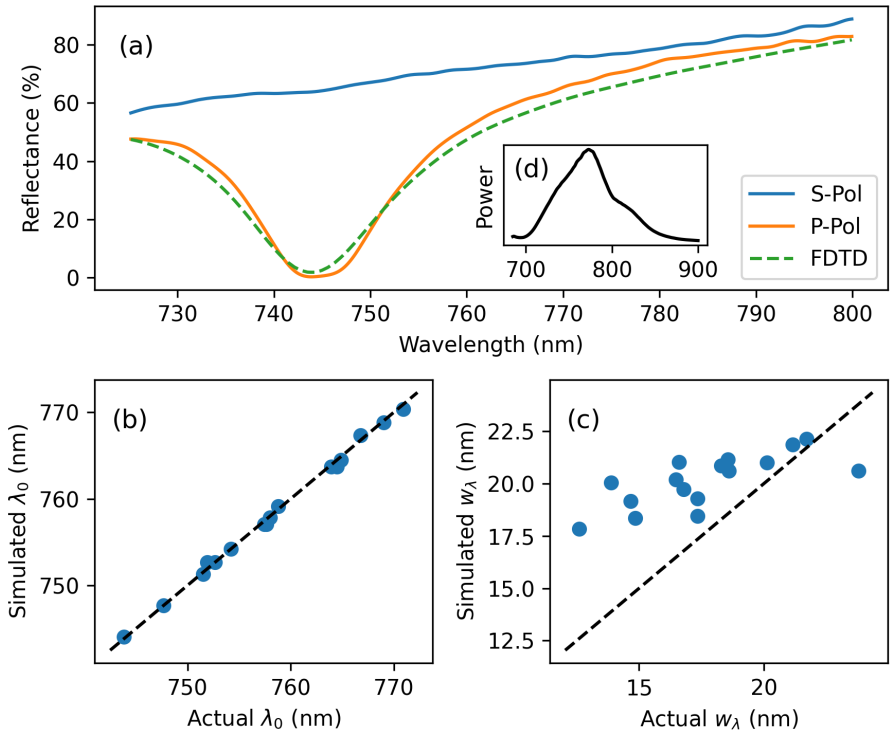

Figure 5.3: (a) An example of reflectance spectra measured from one of the cathodes (670 nm pitch, 17.1 nm width) with a fit to the FDTD model using groove width as the free parameter; (b) Peak absorption wavelength of model and measured grooves; (c) Full width at half max of absorption peak in model and fabricated sample. (d) Spectrum of the mode-locked driving laser.

measure the reflectance spectra of the nanogroove photocathodes (see Fig. 5.3d). Difference spectra were calculated using the beam reflected from the patterned surface against a reference pulse from an upstream 50-50 beamsplitter for both vertically and horizontally polarized light (cathode grooves run horizontal in this experiment). The reflected spectra for vertically polarized light was fit to FDTD calculations [2] using the groove width as the free parameter. Fig. 5.3a reports an example of fit result for one cathode, exemplifying the close match found between the simulated and measured reflectance. The groove widths extracted are reported in Tab. 5.1 (the fourth column) for all the cathodes in a square. From such results we are able to confirm our fabrication methodology,

Table 5.1: Dimensions of the nanogroove cathodes: pitch (p) and groove width extracted from the fit of the reflectance spectra (w). Measured effective nonlinear yield (a_4) and estimate of yield enhancement over flat gold.

Row	Col	p (nm)	w (nm)	a_4 $\left((\mathrm{cm}^2/\mathrm{A})^4\right)$	Enhancement
1	1	670	14.5	3.0×10^{-37}	3.0×10^{6}
1	2	670	14.5	4.0×10^{-38}	4.0×10^{5}
1	3	670	15.8	2.3×10^{-39}	2.3×10^{4}
1	4	670	17.1	1.6×10^{-38}	1.6×10^{5}
2	1	680	14.5	8.9×10^{-37}	8.9×10^{6}
2	2	680	14.5	1.3×10^{-37}	1.3×10^{6}
2	3	680	15.4	1.0×10^{-36}	1.0×10^{7}
2	4	680	16.2	2.9×10^{-37}	2.9×10^{6}
3	1	690	14.1	3.0×10^{-37}	3.0×10^{6}
3	2	690	14.1	2.2×10^{-37}	2.2×10^{6}
3	3	690	15.4	2.2×10^{-37}	2.2×10^{6}
3	4	690	15.8	6.4×10^{-39}	6.4×10^{4}
4	1	700	14.1	4.5×10^{-38}	4.5×10^{5}
4	2	700	13.7	1.8×10^{-37}	1.8×10^{6}
4	3	700	14.5	5.8×10^{-40}	5.8×10^{3}
4	4	700	15.4	3.7×10^{-39}	3.7×10^{4}

as width values increase with column indices, i.e. with electron beam lithography dose, matching our expectations.

Measured and simulated fit peak absorption wavelength and full width at half max of the peak are compared in Fig. 5.3b and c, showing excellent agreement. The slight deviation of the measured groove bandwidth (larger) with respect to the model (narrower) may be explained by small deviations in the laser angle of incidence between measurement and the FDTD calculation, or in differences in the sharpness of the edges of the grooves.

Overall, these measurements demonstrate an ability to fabricate nanopatterned photocathodes with engineered optical properties.

5.5 Nonlinear Photoemission from Nanopatterned Cathode

In this section we describe the measured non-linear electron yield and average current of the nanogroove arrays.

The generalized Fowler-DuBridge model of multi-photon photoemission gives the scaling of n-photon current density, J_n, with laser intensity as the following [102, 48].

$$J_n = a_n A_0 \left(\frac{e}{h\nu}(1 - R_\nu)I\right)^n T^2 F\left(\frac{nh\nu - e\phi}{k_B T}\right), \tag{5.2}$$

where a_n is a cathode dependent constant representing the chance of multiphoton excitation, h is Planck's constant, k_B is the Boltzmann constant, e is the fundamental charge, ν is the optical frequency, R_ν is the metal's reflectivity, ϕ is the work function, I is the optical intensity, T is temperature, and n is the order of emission. The value $A_0 = 4\pi m_e k_B^2 e/h^3 \approx 120\,\mathrm{A/cm^2/K^2}$ is the Richardson constant with m_e as the electron mass. The Fowler function can be written as $F(x) = \int_0^\infty \mathrm{d}y\ \ln(1 + \exp(-y - x))$.

The literature value of ϕ for gold is 5.4 eV [12]. Therefore we expect fourth order photoemission from the cathode when using 800 nm (1.54 eV) photons. Typical values for a_4 of flat gold [143] lie around $a_4 \approx 10^{-43}\,(\mathrm{cm^2/A})^4$. Previous work on nanopatterned gold has demonstrated non-linear electron yield enhancements of the order of 10^6 with pA-scale currents [129].

A schematic of our experimental setup for the measurement of electron beams from nanostructures is shown in Fig. 5.4. We transferred the nanopatterned wafers into a 20 kV electron gun, and used the 80 MHz repetition rate mode-locked Ti:Sapphire oscillator as the drive laser. The pulse was sent through a chirped pulse compressor to achieve a Fourier-transform-limited

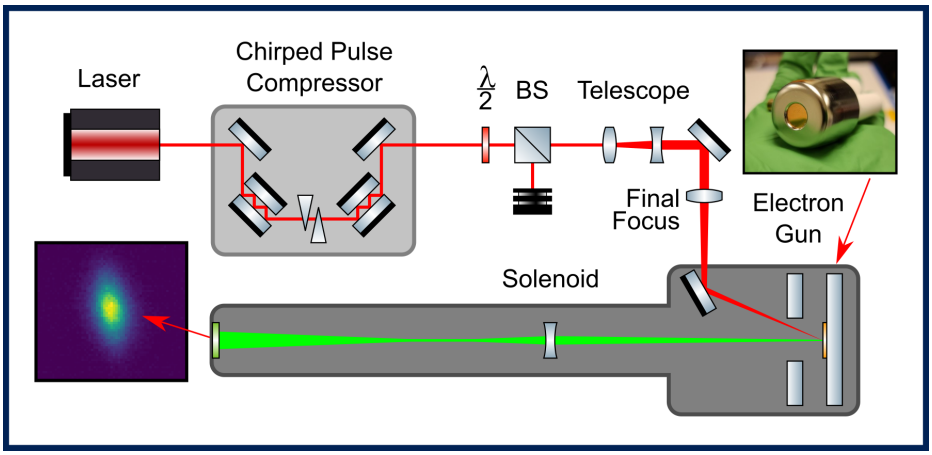

Figure 5.4: A schematic of the beamline used in the measurements. An 80 MHz Ti:Sapphire oscillator emits pulses centered around 770 nm. The light is sent through a chirped pulse compressor for temporal compression, and the beam is focused to a waist using a 600 mm focal length lens placed just before the window of the vacuum chamber. Intensity may be adjusted with a beamsplitter (BS) and half-waveplate ($\lambda/2$) pair. A telescope is used to expand the beam before hitting the lens to decrease its ultimate focused size. The electron beam emitted from the cathode is accelerated and sent through a solenoid lens before being imaged on a scintillator screen.

pulse length of ~15 fs at the sample, also confirmed by autocorrelation measurements. The pulse was then focused to an RMS spot size 40 µm at the cathode plane with a small angle of incidence of 4 degrees with respect to the surface normal. The intensity was varied using the combination of an achromatic half-wave plate and a polarizing beamsplitter. The maximum laser energy that could be sent to the cathode after transport, and longitudinal and transverse shaping was 1 nJ. In the electron gun, the grooves of the cathode run vertically.

To begin, the polarizing beamsplitter was temporarily removed and the half-wave plate was used to control the orientation of linear polarization of the laser. Photocurrent was measured from a single cathode using a lock-in amplifier and fit to the model $J(\theta) = A \cdot (\cos^2(\theta + \phi))^n + o$ where A is the amplitude, o is an offset, and ϕ is a phase to account for mis-positioning of the half-wave plate in its rota-

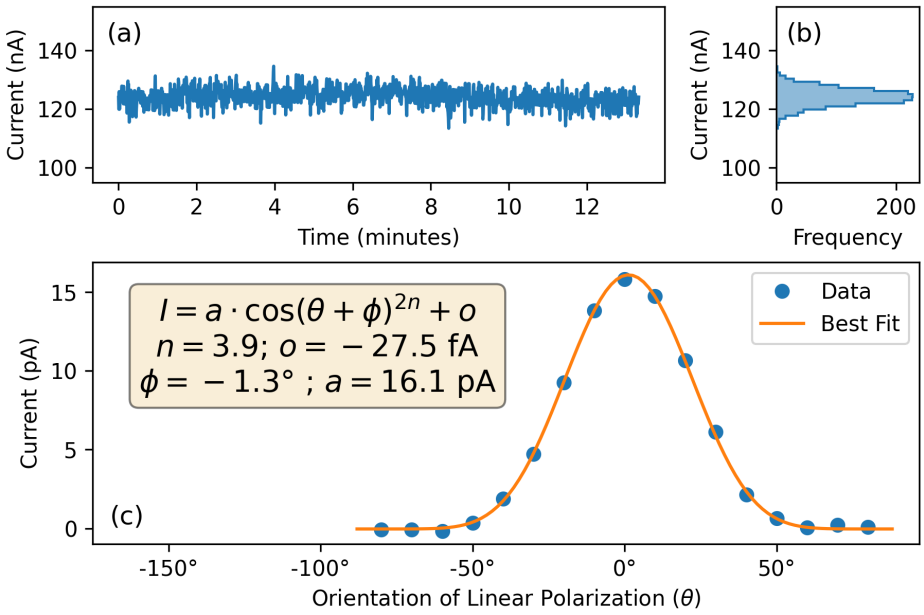

Figure 5.5: (a) Time series measurements of photocurrent from a nanopatterned photocathode; (b) Histogram of jitter in photocurrent; (c) Measurements of photocurrent as angle of linear polarization is changed with line of best fit.

tion mount. Our data and line of best fit are shown in Fig. 5.5c and we conclude from the goodness of fit that only the polarization of light running "against the grain" of the grooves is able to excite plasmons and cause multiphoton photoemission, as expected.

The polarizing beamsplitter was replaced and emitted electron photocurrent was measured as a function of optical intensity (Fig. 5.6a) for each of the cathodes in a square within the wafer. Eq. 5.2 was then used in a fit to find the nonlinear yield coefficient (a_4), using 98% [12] as the value of gold's reflectivity at 760 nm.

The distribution of measured non-linear yield exponents is shown in Fig. 5.6d. All of the measured behaviours are consistent with fourth order photoemission. The measured value of nonlinear yield coefficient varied from $a_4 = 3 \times 10^{-40}$ to 6×10^{-37} $(\text{cm}^2/\text{A})^4$. A representation of its value distribution across

the 16 cathodes in a square is shown in Fig. 5.6b.

One explanation for the variation in a_4 is the change in optical response of the grooves depending on their geometry (see Fig. 5.3a), that will change the overall coupling of the laser's power into the structure. Depending on the value of the peak absorption wavelength, the reflectance curve will align better or worse with the power spectrum of the laser (Fig. 5.3d), changing the amount of total absorbed intensity from the laser that then excites electrons in the metal. Indeed, if we calculate the absorbed intensity based on both the absorption spectra of the grooves and the laser's spectrum for each groove array, we observe a correlation (Fig. 5.6c). Other factors may need to be included in the analysis of the data to explain the spread of a_4 in full. For example, the effect of the plasmonic nearfield on the emitted electrons and the probability of electrons emitted inside the grooves escaping may contribute to the residual difference.

Current emission from the flat (non-patterned) gold surface was below our measurement sensitivity, owing to the limited available optical intensity in the setup. Nevertheless, with a maximum power density achievable of $\sim 2\,\mathrm{GW\,cm^{-2}}$, and a measurement system's noise floor of $\sim 50\,\mathrm{fA}$, we can calculate an upper bound for the nonlinear yield coefficient of $a_4 < 4 \times 10^{-43}\,(\mathrm{cm^2/A})^4$, with a yield enhancement from nanopatterning in excess of 10^6.

The current stability of the cathode performance is summarized in Fig. 5.5. A continuous acquisition of average electron current values over about 12 min was performed, with the laser pulses delivering the maximum available energy (Fig. 5.5a). A stable average current value of 120 nA was measured, with fluctuations measured to be 2.3% (see Fig. 5.5b).

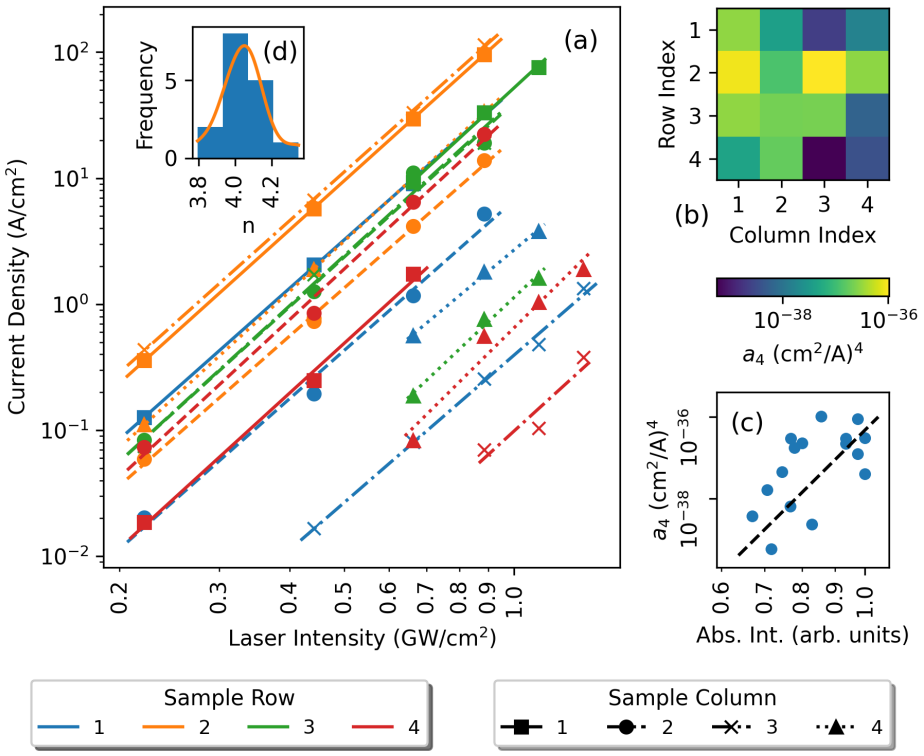

Figure 5.6: (a) Measurements of photocurrent as laser intensity is varied with power-law fits shown as lines; (b) Best fit yield (a_n in Eq. 5.2), laid out by location on the 4x4 grid of cathodes (Fig. 5.2b); (c) Scatter plot of yield (a_4) and estimated absorbed laser intensity; (d) The distribution of exponents in best fit curves (blue histogram, orange kernel density estimator).

This experiment exemplifies the disruptive potential of the technology in high average current electron sources. Indeed, assuming a gold UV quantum efficiency of 10^{-5} [52] and a typical conversion efficiency from NIR to UV of 7.5%, then linear photoemission would require a tenfold increase in laser power to generate the same average current, about 0.75 W in the NIR against the 80 mW used in the experiment.

5.6 Mean Transverse Energy of the Emitted Electron Beam

In this section we explore the mean transverse energy (MTE) [84] of the nanogroove cathodes. After showing that surface nanopatterning can lead to very large nonlinear yield enhancements in metals, we now seek to explore the effects of such enhancement on the beam's transverse brightness. Early work on nanopatterned photocathodes found larger emittance values than what is expected from a flat surface [87]. Since then, substantial work tailored at improving the photoemission properties of these cathodes has been carried out, for example by selecting and optimizing the fabrication technique for minimal roughness and sharp patterns, and by developing methods for in-situ optical characterization of the structures [42]. Owing to such developments, we are now able to relate photoemission properties such as the cathode electron beam MTE, to the surface mechanical and optical characteristics.

We investigate the transverse emittance of the grooves using the solenoid scan method. The electron gun is biased at high voltage to generate a beam from one of the cathodes in the square (row two and column one in Fig. 5.2b; 680 nm pitch and 14.5 nm width). The generated electron beam passes through a solenoid lens a few centimeters away from the cathode and hits a scintillator screen 60 cm away. Here the beam's RMS spot size was measured as function of strength of the solenoid lens. The experiment was repeated at 20 kV, 19 kV, and 18 kV (data shown in Fig. 5.7) and the beam sizes were fit using a linear model of transport including the accelerating electric field in the gun, following the procedure in [15, 67] to recover the initial phase space moments. The laser RMS spot size at the cathode was measured to be 20 µm. We find the cathode MTE to be asymmetric, with $\mathrm{MTE}_x = 510$ meV and $\mathrm{MTE}_y = 250$ meV. The x and y axes are

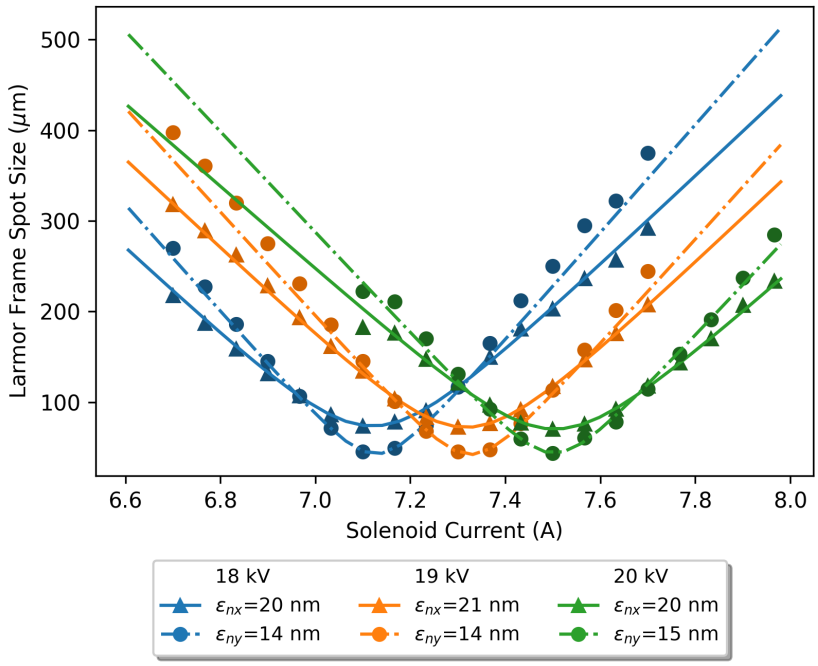

Figure 5.7: Solenoid scan measurements of the generated beam's normalized emittance. The beam's size (shown here in the Larmor frame) is measured as a function of current in the beamline's solenoid. Fits to a linear model of the beamline are shown as the curves with the best fit emittance in the legend.

aligned with respect to the cathode nanogrooves, which run along the vertical (y) direction. The MTE along this direction is close to what's typical for a flat metal with this excess energy [39]. On the other hand, the MTE in the horizontal (x) plane shows a substantial increase, which we attribute to geometric effects, as described below.

While nanopatterning has clear benefits for the non-linear yield of photocathodes, those same nanoscale features are a form of surface roughness. Surface roughness is well known to cause an increase in the MTE of the emitted electrons from a photocathode [21]. Two major effects contribute to this increase: the additional transverse momentum gained from the local distortions

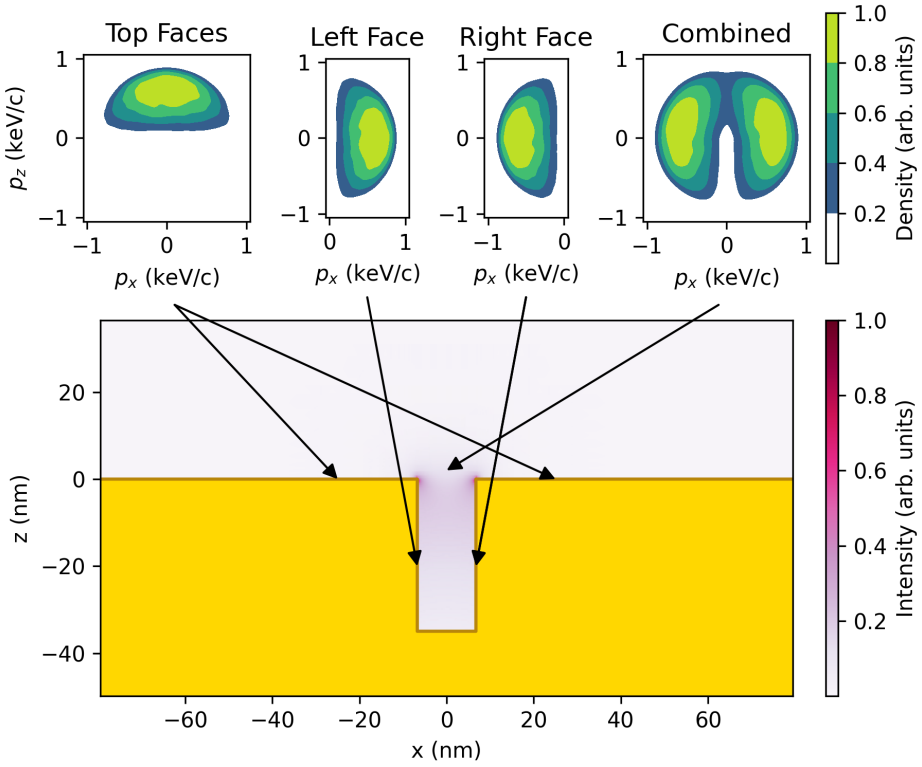

Figure 5.8: A schematic showing how the initial momentum distribution from each face of the nanogroove may be combined to form an estimate of MTE including roughness effects.

of electric fields around surface features (as in Fig. 5.1) and the local deviation of the average direction of photoemission with respect to the global beamline axis, which follows the surface normal. For nanogroove photocathodes, these effects will vanish in one direction (y in our setup), thanks to the structure's translational symmetry. To understand the increase of emittance on the horizontal (x) axis, we will now estimate the contribution of both effects in our setup.

For the first effect, we compute the value of the externally applied electric field around the nanogrooves using the finite difference method [96], assuming perfect edges (i.e. a radius of curvature equal to the simulation mesh size). This is shown as the blue arrows in Fig. 5.1a. We then compute the integral of the transverse field along the particle trajectory starting from the groove

edge to find the maximum transverse energy acquired by the electrons. For the max achievable cathode field in the gun (which will maximize this effect) of $7\,\mathrm{MV\,m^{-1}}$, this effect only adds $\sim$10 meV of transverse energy to the emitted electrons.

To estimate the effect of the local variations of the surface normal on the MTE, we start by randomly sampling the 3D momentum distribution of electrons emitted from a flat metallic surface [39], generating a set of 100k virtual particles. Assuming a work function for gold of 5.4 eV [97] and fourth order photoemission process, a numerical calculation of the MTE of these particles gives a value of 257 meV, in close accordance with our measurement in the vertical plane and the analytical expression MTE = $(nh\nu - \phi)/3$. Rotating the distribution following the local normal to the surface, and adding together all of the contributions, we can obtain an estimate of the total MTE including the effect of nanopatterning. The number of electrons emitted from each nanogroove face along the surface is weighted by the integral of the fourth power of the intensity along it, extracted by FDTD simulations (Fig. 5.1a). This gives a ratio of side wall to top emission of 6.9:1 and the total estimated MTE with normal vector effects included of 481 meV. Adding in the $\sim$10 meV calculated above due to the effects of the transverse fields, this approaches our measured value in the horizontal plane of 510 meV. A visual of how this estimate is made can be found in Fig. 5.8.

5.7 Conclusion

In this work we report the development and engineering of a novel metal photocathode for high brightness ultrafast electron generation. We demonstrate increased average current when using plasmon-assisted multiphoton photoemission with respect to linear photoemission in our setup, overcoming the major drawbacks of metal cathodes caused by their poor QE in the UV, and paving the way to their use in high average current-high brightness applications, such as X-FELs and UED setups.

Our fabricated cathodes closely match their designed optical performance. In particular, we are able to tune the peak absorption wavelength of the structure to the spectral peak of the driving laser.

Electron yield was strongly enhanced via surface nano-structuring, a factor in excess of 10^6 over fourth-order photoemission from flat gold, and a reduction in power by a factor of ~10 compared to linear photoemission for the intensities achieved in this work. Continuous operations at high average current showed no degradation (Fig. 5.5a). To showcase the potential impact of such nanopatterned cathodes, we compare their requirements with typical metal photocathodes used in large-scale facilities. As an example, The LCLS X-FEL at SLAC [45] uses linear photoemission from flat copper cathodes. By using the operational values for the laser, cathode QE, and beam charge [170, 169] (3 ps FWHM, 150 pC pulse from a 1 mm hard edge spot size, QE of 4×10^{-5}) and a typical operational conversion efficiency from IR to UV of 7.5%, a flat copper cathode requires about 240 µJ of energy in the IR pulse, compared to the 8 µJ necessary for the gold nanostructured photocathode presented here. The advantage of

nanopatterning becomes even more pronounced in applications requiring low charge and femtosecond-long pulses, such as UED setups [51]. The example shown in Fig. 5.5a, 1.5 fC electron beams are produced using only 1 nJ of IR energy extracted directly from an ultrafast laser oscillator.

The normalized transverse emittance of the photoemitted beam was measured systematically for different beam energies, providing a benchmark value for the transverse brightness of nanopatterned cathodes. The measured asymmetry in the emittance can be fully explained by the geometry of the structure, with its asymmetric roughness. These results suggests an interesting application of nanogroove arrays as a future platform for studying the effects of roughness on electron source brightness In these systems, the roughness can be engineered to take on certain profiles. Further, the fact that the cathode "acts flat" in one direction provides a control measurement to directly compare the effects of roughness against in each sample. For the application of cathodes in high brightness photoinjectors, although the emittance is increased in the direction normal to the grooves, it is still in line or better than typical values measured in ultrafast X-ray user facilities [4].

An interesting future application of emission from patterned surfaces is the possibility to obtain transverse electron beam density modulation and shaping. Since electrons are only emitted near the groove edges, structures could be engineered to generate nanoscale beamlets and density modulations. Using linear optics to perform an emittance exchange [107] this modulation can be transferred into time and used to drive temporal patterning in the beam which is of interest to coherent x-ray light sources [62]. Also, a round beam [33, 22] could be generated to average out the emittances in both directions.

To further reduce the emittance from plasmonic photocathodes, emission from a flat surface would be required, for example by using a plasmonic lens, as described in [42], where surface plasmon interference is used to produce large and instantaneous field enhancements in pattern-free areas well below one micrometer. The implementation of this design could improve the transverse brightness from metal cathodes even further over the state-of-the-art.

CHAPTER 6

FUTURE DIRECTIONS

In this thesis, several paths toward improving the brightness of photocathode-based electron sources have been reported. However, there are still many areas of this field left to explore. This chapter will briefly describe some of these promising future points of research.

In Chapter 5, nanopatterning was studied as a method of improving the nonlinear yield of metal photocathodes. A second interesting use of this technology is to form nanoscale lenses on the surface of a metal cathode [42]. Due to their high numerical aperture (compared to what is achievable from external optical elements in a photoinjector) these structures can achieve small spot sizes (<1 μm). Driving the cathode with fourth-order nonlinearity further decreases the initial electron beam spot size by a factor of two. This substantial reduction in spot size shrinks the initial emittance of the beam and improves its brightness. The extremely high fields around these cathodes may also be used to manipulate charged particle beams with applications in ultrafast physics.

Investigating the low-temperature properties of photocathodes is an important future direction for the field. Cold photocathodes may have better properties compared to those at room temperature. Cooling them reduces the size of the Fermi tail of the electron occupation function and some results [29] suggest that this can lower the MTE of photocathodes. Some work has pointed to electron-phonon scattering to be an important mechanism that affects the MTE of certain semiconductor photocathodes. Cooling the system also changes the occupation of phonon modes in the material and could change the cathode's properties. Work is concluding at Cornell on a cryogenically cooled electron

gun designed for the study of these materials.

Work on the growth of near atomically flat photocathodes holds promise in increasing the brightness of electron beams. Recent research [57] has shown that some semiconductors (specifically Cs_3Sb) can be grown epitaxially on a lattice-matched substrate. Through this process, the surface roughness, and therefore the increase in MTE due to geometric factors, is greatly reduced. Potential exists here for the growth of a variety of new materials with better quality than has been achieved before.

Machine learning is an interesting technology and has only just started to be adopted for the design and control of particle accelerators. These methods promise to greatly speed up simulations involving electron beams subject to space charge. Research into this area may also lead to the development of advanced control algorithms to aid in the real-time optimization of accelerator performance. This all benefits the practical use of high-brightness electron beams in applications where the transport of the beam is difficult. Further work may also improve the development of new photocathode concepts with faster computation of material properties.

As was pointed out in Chapter 2 of this thesis, even challenging real-world applications can benefit from reducing the MTE of photocathodes down to the level of 10 meV. That quality of photocathode is still far from being achieved practically. However, the future is promising for bright electron sources and with the right material research and accelerator designs to take advantage of these new technologies, improving the brightness of electron beams for users by as much as 100x may be possible. With such improvements, techniques only available at the national labs with billion-dollar budgets may become accessible

to university users. A new world of time-resolved experiments on complex systems could be opened up and let us venture further into the nature of large and dynamic molecular systems. The production of new brighter electron beams has the potential to transform the way science at the atomic scale is performed. Photocathodes are likely a key component of any route to that future.

BIBLIOGRAPHY

[1] XFEL, the European X-ray free-electron laser: technical design report. Technical Report DESY 2006-097, DESY XFEL Project Group, Hamburg, 2006. OCLC: 254657183.

[2] Lumerical, Finite difference time domain solutions, 2011.

[3] P. Abbamonte, F. Abild-Pederse, P. Adams, M. Ahmed, and F. Albert. New Science Opportunities Enabled by LCLS-II X-Ray Lasers. Technical Report SLAC-R-1053, SLAC, Menlo Park, CA (US), June 2015.

[4] R. Akre, D. Dowell, P. Emma, J. Frisch, S. Gilevich, G. Hays, Ph. Hering, R. Iverson, C. Limborg-Deprey, H. Loos, A. Miahnahri, J. Schmerge, J. Turner, J. Welch, W. White, and J. Wu. Commissioning the Linac Coherent Light Source injector. *Physical Review Special Topics - Accelerators and Beams*, 11(3):030703, March 2008.

[5] O A Anderson. Internal Dynamics and Emittance Growth in Space-Charge-Dominated Beams. *Particle Accelerators*, 21:30, 1987.

[6] S. G. Anderson and J. B. Rosenzweig. Nonequilibrium transverse motion and emittance growth in ultrarelativistic space-charge dominated beams. *Phys. Rev. ST Accel. Beams*, 3(9):094201, September 2000.

[7] A. Arnold and J. Teichert. Overview on superconducting photoinjectors. *Phys. Rev. ST Accel. Beams*, 14(2):024801, February 2011.

[8] Jai Kwan Bae, Ivan Bazarov, Pietro Musumeci, Siddharth Karkare, Howard Padmore, and Jared Maxson. Brightness of femtosecond nonequilibrium photoemission in metallic photocathodes at wavelengths near the photoemission threshold. *Journal of Applied Physics*, 124(24):244903, December 2018.

[9] Jai Kwan Bae, Luca Cultrera, Philip DiGiacomo, and Ivan Bazarov. Rugged spin-polarized electron sources based on negative electron affinity GaAs photocathode with robust Cs_2Te coating. *Applied Physics Letters*, 112(15):154101, April 2018.

[10] Jai Kwan Bae, Alice Galdi, Luca Cultrera, Frank Ikponmwen, Jared Maxson, and Ivan Bazarov. Improved lifetime of a high spin polarization su-

perlattice photocathode. *Journal of Applied Physics*, 127(12):124901, March 2020.

[11] K Baptiste, J Corlett, T M Huang, S Kwiatkowski, D Li, J Qiang, F Sannibale, J Staples, R Wells, L Yang, A Zholents, and J McKenzie. Status of the LBNL Normal-Conducting CW VHF Photo-Injector. In *Proceedings of the 2009 Particle Accelerator Conference*, page 4, Vancouver, BC, Canada, 2009.

[12] Michael Bass. *Handbook of Optics*. McGraw Hill Professional, October 2000.

[13] Ivan V. Bazarov. Synchrotron radiation representation in phase space. *Physical Review Special Topics - Accelerators and Beams*, 15(5), May 2012.

[14] Ivan V. Bazarov, Bruce M. Dunham, Colwyn Gulliford, Yulin Li, Xianghong Liu, Charles K. Sinclair, Ken Soong, and Fay Hannon. Benchmarking of 3D space charge codes using direct phase space measurements from photoemission high voltage dc gun. *Physical Review Special Topics - Accelerators and Beams*, 11(10):100703, October 2008.

[15] Ivan V. Bazarov, Bruce M. Dunham, Yulin Li, Xianghong Liu, Dimitre G. Ouzounov, Charles K. Sinclair, Fay Hannon, and Tsukasa Miyajima. Thermal emittance and response time measurements of negative electron affinity photocathodes. 103(5):054901.

[16] Ivan V. Bazarov, Bruce M. Dunham, and Charles K. Sinclair. Maximum Achievable Beam Brightness from Photoinjectors. *Phys. Rev. Lett.*, 102(10):104801, March 2009.

[17] Ivan V. Bazarov, Allen Kim, Manu N. Lakshmanan, and Jared M. Maxson. Comparison of dc and superconducting rf photoemission guns for high brightness high average current beam production. *Phys. Rev. ST Accel. Beams*, 14(7):072001, July 2011.

[18] Ivan V. Bazarov and Charles K. Sinclair. Multivariate optimization of a high brightness dc gun photoinjector. *Physical Review Special Topics - Accelerators and Beams*, 8(3), March 2005.

[19] C. N. Berglund and W. E. Spicer. Photoemission Studies of Copper and Silver: Theory. *Physical Review*, 136(4A):A1030–A1044, November 1964.

[20] C H Boulware and DESY Zeuthen. Latest Results at the Upgraded PITZ Facility. In *Proceedings of FEL08*, page 4, Korea, 2008. JACOW Publishing.

[21] D J Bradley, M B Allenson, and B R Holeman. The transverse energy of electrons emitted from GaAs photocathodes. 10(1):111–125.

[22] R. Brinkmann, Y. Derbenev, and K. Flöttmann. A low emittance, flat-beam electron source for linear colliders. *Physical Review Special Topics - Accelerators and Beams*, 4(5):053501, May 2001.

[23] A. D. Cahill, J. B. Rosenzweig, V. A. Dolgashev, S. G. Tantawi, and S. Weathersby. High gradient experiments with X -band cryogenic copper accelerating cavities. *Phys. Rev. Accel. Beams*, 21(10):102002, October 2018.

[24] B. Carlsten. New Photoelectric Injector Design for the Los Alamos National Laboratory XUV FEL Accelerator. Jerusalem, Israel, 1988.

[25] B. Carlsten. Space-Charge-Induced Emittance Compensation in High-Brightness Photoinjectors. *Particle Accelerators*, 17(1):27–65, January 1995.

[26] Jean-Pierre Causse. Status Report on the Development of the ASCOP Photomultipiers. *IRE Transactions on Nuclear Science*, 9(3):90–96, June 1962.

[27] W N Charman. Properties of photomultipliers with caesium telluride photocathodes. *Journal of Physics E: Scientific Instruments*, 2(2):157–161, February 1969.

[28] E Chevallay, S Hutchins, P Legros, G Suberlucq, and H Trautner. Production and Studies of Photocathodes for High Intensity Electron Beams. In *Proceedings of the 20th International Linac Conference*, page 3, Monterey, California, August 2000.

[29] L. Cultrera, S. Karkare, H. Lee, X. Liu, I. Bazarov, and B. Dunham. Cold electron beams from cryocooled, alkali antimonide photocathodes. *Phys. Rev. ST Accel. Beams*, 18(11):113401, November 2015.

[30] R. de Boer and E.H.P. Cordfunke. On the caesium-rich part of the Cs2Te phase diagram. *Journal of Alloys and Compounds*, 228(1):75–78, September 1995.

[31] K Deb. *Multi-Objective Optimization using Evolutionary Algorithms*, volume 16. John Wiley & Sons, 2001.

[32] K. Deb, A. Pratap, S. Agarwal, and T. Meyarivan. A fast and elitist multiobjective genetic algorithm: NSGA-II. *IEEE Transactions on Evolutionary Computation*, 6(2):182–197, April 2002.

[33] Ya Derbenev. Technical Report UMHE-98-04, University of Michigan, 1998.

[34] A. Descoeudres, T. Ramsvik, S. Calatroni, M. Taborelli, and W. Wuensch. dc breakdown conditioning and breakdown rate of metals and metallic alloys under ultrahigh vacuum. *Phys. Rev. ST Accel. Beams*, 12(3):032001, March 2009.

[35] S. Di Mitri and S. Spampinati. Estimate of free electron laser gain length in the presence of electron beam collective effects. *Physical Review Special Topics - Accelerators and Beams*, 17(11), November 2014.

[36] Y. Ding, A. Brachmann, F.-J. Decker, D. Dowell, P. Emma, J. Frisch, S. Gilevich, G. Hays, Ph. Hering, Z. Huang, R. Iverson, H. Loos, A. Miahnahri, H.-D. Nuhn, D. Ratner, J. Turner, J. Welch, W. White, and J. Wu. Measurements and Simulations of Ultralow Emittance and Ultrashort Electron Beams in the Linac Coherent Light Source. *Physical Review Letters*, 102(25), June 2009.

[37] Valery Dolgashev, Sami Tantawi, Yasuo Higashi, and Bruno Spataro. Geometric dependence of radio-frequency breakdown in normal conducting accelerating structures. *Appl. Phys. Lett.*, 97(17):171501, October 2010.

[38] David H. Dowell, John W. Lewellen, Dinh Nguyen, and Robert Rimmer. The status of normal conducting RF (NCRF) guns, a summary of the ERL2005 workshop. *Nuclear Instruments and Methods in Physics Research Section A: Accelerators, Spectrometers, Detectors and Associated Equipment*, 557(1):61–68, February 2006.

[39] David H. Dowell and John F. Schmerge. Quantum efficiency and thermal emittance of metal photocathodes. *Physical Review Special Topics - Accelerators and Beams*, 12(7):074201, July 2009.

[40] B. M. Dunham, L. S. Cardman, and C. K. Sinclair. Emittance measurements for the illinois/CEBAF polarized electron source. In *Proceedings Particle Accelerator Conference*, volume 2, pages 1030–1032 vol.2.

[41] B. M. Dunham, C. K. Sinclair, I. V. Bazarov, Y. Li, X. Liu, and K. W. Smolenski. Performance of a very high voltage photoemission electron gun for a high brightness, high average current erl injector. In *2007 IEEE Particle Accelerator Conference (PAC)*, pages 1224–1226, Albuquerque, NM, 2007. IEEE.

[42] Daniel B. Durham, Fabrizio Riminucci, Filippo Ciabattini, Andrea Mostacci, Andrew M. Minor, Stefano Cabrini, and Daniele Filippetto. Plasmonic lenses for tunable ultrafast electron emitters at the nanoscale. *Physical Review Applied*, 12(5):054057, November 2019.

[43] Jason R Dwyer, Christoph T Hebeisen, Ralph Ernstorfer, Maher Harb, Vatche B Deyirmenjian, Robert E Jordan, and R.J Dwayne Miller. Femtosecond electron diffraction: 'making the molecular movie'. *Philosophical Transactions of the Royal Society A: Mathematical, Physical and Engineering Sciences*, 364(1840):741–778, March 2006.

[44] L. Emery. Global Optimization of Damping Ring Designs Using A Multi-Objective Evolutionary Algorithm. In *Proceedings of the 2005 Particle Accelerator Conference*, pages 2962–2964, Knoxville, TN, USA, 2005. IEEE.

[45] P. Emma, R. Akre, J. Arthur, R. Bionta, C. Bostedt, J. Bozek, A. Brachmann, P. Bucksbaum, R. Coffee, F.-J. Decker, Y. Ding, D. Dowell, S. Edstrom, A. Fisher, J. Frisch, S. Gilevich, J. Hastings, G. Hays, Ph. Hering, Z. Huang, R. Iverson, H. Loos, M. Messerschmidt, A. Miahnahri, S. Moeller, H.-D. Nuhn, G. Pile, D. Ratner, J. Rzepiela, D. Schultz, T. Smith, P. Stefan, H. Tompkins, J. Turner, J. Welch, W. White, J. Wu, G. Yocky, and J. Galayda. First lasing and operation of an ångstrom-wavelength free-electron laser. *Nature Photonics*, 4(9):641–647, September 2010.

[46] Jun Feng, J. Nasiatka, Weishi Wan, Siddharth Karkare, John Smedley, and Howard A. Padmore. Thermal limit to the intrinsic emittance from metal photocathodes. *Appl. Phys. Lett.*, 107(13):134101, September 2015.

[47] M Ferrario, J E Clendenin, D T Palmer, J B Rosenzweig, and L Serafini. Homdyn Study for the LCLS RF Photo-Injector. Technical Report SLAC-PUB 8400, INFN, Frascati, Italy, 2000.

[48] Gabriele Ferrini, Francesco Banfi, Claudio Giannetti, and Fulvio Parmigiani. Non-linear electron photoemission from metals with ultrashort pulses. *Nuclear Instruments and Methods in Physics Research Section A: Accelerators, Spectrometers, Detectors and Associated Equipment*, 601(1-2):123–131, March 2009.

[49] D. Filippetto, P. Musumeci, M. Zolotorev, and G. Stupakov. Maximum current density and beam brightness achievable by laser-driven electron sources. *Phys. Rev. ST Accel. Beams*, 17(2):024201, February 2014.

[50] D Filippetto and H Qian. Design of a high-flux instrument for ultrafast electron diffraction and microscopy. *Journal of Physics B: Atomic, Molecular and Optical Physics*, 49(10):104003, May 2016.

[51] Daniele Filippetto, Pietro Musumeci, Renkai Li, Bradley John Siwick, Martin Otto, and Martin Centurion Joao Pedro Nunes. Ultrafast Electron Diffraction: Visualizing Dynamic States of Matter, June 2022. arXiv:2207.00080 [cond-mat, physics:physics].

[52] J Fischer and T Srinivasan-Rao. UV Photoemission Studies of Metal Photocathodes for Particle Accelerators. page 26, Erice, Italy, 1988.

[53] G B Fisher, W E Spicer, P C McKernan, V F Pereskok, and S J Wanner. A Standard for Ultraviolet Radiation. *Applied Optics*, 12(4):6, April 1973.

[54] Klaus Floettmann. ASTRA: A Space Charge Tracking Algorithm, 2017.

[55] Klaus Floettmann. Emittance compensation in split photoinjectors. *Phys. Rev. Accel. Beams*, 20(1):013401, January 2017.

[56] Cliff M. Fortgang, Gerald O. Bolme, Jody Lamoureux, and Don J. Liska. Cryogenic experiments on rf accelerating structures. *Nuclear Instruments and Methods in Physics Research Section A: Accelerators, Spectrometers, Detectors and Associated Equipment*, 262(2-3):197–199, December 1987.

[57] Alice Galdi, Jan Balajka, William J. I. DeBenedetti, Luca Cultrera, Ivan V. Bazarov, Melissa A. Hines, and Jared M. Maxson. Reduction of surface roughness emittance of Cs_3Sb photocathodes grown via codeposition on single crystal substrates. *Applied Physics Letters*, 118(24):244101, June 2021.

[58] M. Gaowei, J. Sinsheimer, D. Strom, J. Xie, J. Cen, J. Walsh, E. Muller, and J. Smedley. Codeposition of ultrasmooth and high quantum efficiency cesium telluride photocathodes. *Physical Review Accelerators and Beams*, 22(7):073401, July 2019.

[59] Kevin F. Garrity, Joseph W. Bennett, Karin M. Rabe, and David Vanderbilt. Pseudopotentials for high-throughput DFT calculations. *Computational Materials Science*, 81:446–452, January 2014.

[60] G. Gevorkyan, S. Karkare, S. Emamian, I. V. Bazarov, and H. A. Padmore. Effects of physical and chemical surface roughness on the brightness of electron beams from photocathodes. 21(9):093401.

[61] Y. Gong, Alan G. Joly, L.M. Kong, Patrick Z. El-Khoury, and Wayne P. Hess. High-Brightness Plasmon-Enhanced Nanostructured Gold Photoemitter. *Physical Review Applied*, 2(6):064012, December 2014.

[62] W. S. Graves, F. X. Kärtner, D. E. Moncton, and P. Piot. Intense Superradiant X Rays from a Compact Source Using a Nanocathode Array and Emittance Exchange. *Physical Review Letters*, 108(26):263904, June 2012.

[63] A. Grudiev, S. Calatroni, and W. Wuensch. New local field quantity describing the high gradient limit of accelerating structures. *Phys. Rev. ST Accel. Beams*, 12(10):102001, October 2009.

[64] Colwyn Gulliford, Adam Bartnik, and Ivan Bazarov. Multiobjective optimizations of a novel cryocooled dc gun based ultrafast electron diffraction beam line. *Physical Review Accelerators and Beams*, 19(9), September 2016.

[65] Colwyn Gulliford, Adam Bartnik, Ivan Bazarov, Luca Cultrera, John Dobbins, Bruce Dunham, Francisco Gonzalez, Siddharth Karkare, Hyeri Lee, Heng Li, Yulin Li, Xianghong Liu, Jared Maxson, Christian Nguyen, Karl Smolenski, and Zhi Zhao. Demonstration of low emittance in the Cornell energy recovery linac injector prototype. *Physical Review Special Topics - Accelerators and Beams*, 16(7), July 2013.

[66] Colwyn Gulliford, Adam Bartnik, Ivan Bazarov, and Jared Maxson. Multiobjective optimization design of an rf gun based electron diffraction beam line. *Physical Review Accelerators and Beams*, 20(3), March 2017.

[67] Colwyn Gulliford and Ivan Bazarov. New method for generating linear transfer matrices through combined rf and solenoid fields. *Physical Review Special Topics - Accelerators and Beams*, 15(2):024002, February 2012.

[68] C. P. Hauri, R. Ganter, F. Le Pimpec, A. Trisorio, C. Ruchert, and H. H. Braun. Intrinsic emittance reduction of an electron beam from metal photocathodes. 104(23):234802–1–234802–4.

[69] C Hessler. Lifetime Studies of Cs2 Te Cathodes at the Phin RF Photoinjector at CERN. In *Proceedings of IPAC12*, New Orleans, LA, 2012. Joint Accelerator Conferences Website.

[70] Yves Ineichen. *Massively Parallel Multi-Objective Optimization with Application to Particle Accelerators*. PhD thesis, ETH Zurich, Switzerland, 2013.

[71] I Ivanov, A Mazur, and J Pollmann. The ideal (111), (110) and (100) surfaces of si, ge, and GaAs; a comparison of their electronic structure. 92:365–384.

[72] Lee Jones, David Juarez-Lopez, Boris Militsyn, Tim Noakes, and Carsten Welsch. Transverse Energy Distribution Measurements for Polycrystalline and (100) Copper Photocathodes with Known Levels of Surface Roughness. *Proceedings of the 9th Int. Particle Accelerator Conf.*, IPAC2018:Canada–, 2018.

[73] Jun'ichi Kanasaki, Hiroshi Tanimura, and Katsumi Tanimura. Imaging energy-, momentum-, and time-resolved distributions of photoinjected hot electrons in GaAs. 113(23):237401.

[74] Siddharth Karkare. <10 meV MET from Cu, 2018.

[75] Siddharth Karkare, Gowri Adhikari, W. Andreas Schroeder, J. Kevin Nangoi, Tomas Arias, Jared Maxson, and Howard Padmore. Ultracold electrons via Near-Threshold Photoemission from Single-Crystal Cu(100). *Physical Review Letters*, 125(5):054801, July 2020. arXiv: 2002.11579.

[76] Siddharth Karkare and Ivan Bazarov. Effect of nano-scale surface roughness on transverse energy spread from GaAs photocathodes. *Appl. Phys. Lett.*, 98(9):094104, February 2011. arXiv: 1102.4764.

[77] K. Kim and R. G. Littlejohn. Entropy and emittance of particle and photon beams. In *Proceedings Particle Accelerator Conference*, volume 5, pages 3358–3360 vol.5, May 1995.

[78] T Konomi, Y Honda, E Kako, Y Kobayashi, S Michizono, T Miyajima, H Sakai, K Umemori, and S Yamaguchi. Development of High Intensity, High Brightness, CW SRF Gun with Bi-Alkali Photocathode. page 4, Dresden, Germany, 2019. JACOW Publishing.

[79] Jörg Krüger, Daniela Dufft, Robert Koter, and Andreas Hertwig. Femtosecond laser-induced damage of gold films. *Applied Surface Science*, 253(19):7815–7819, July 2007.

[80] Masao Kuriki, Shigeru Kashiwagi, Yuji Seimiya, and Kazuhide Uchida.

GaAs Photocathode Activation with CsTe Thin Film. *Proceedings of the 6th Int. Particle Accelerator Conf.*, IPAC2015:3 pages, 0.748 MB, 2015. Artwork Size: 3 pages, 0.748 MB ISBN: 9783954501687 Medium: PDF Publisher: JACoW, Geneva, Switzerland.

[81] PM Lapostolle. RMS Emittance. *IEEE Trans. Nucl. Sci.*, NS-18(3):1101, 1971.

[82] J D Lawson, P M Lapostolle, and R L Gluckstern. EMITTANCE, ENTROPY AND INFORMATION. *Particle Accelerators*, 5:5, 1973.

[83] J. Le Perchec, P. Quémerais, A. Barbara, and T. López-Ríos. Why Metallic Surfaces with Grooves a Few Nanometers Deep and Wide May Strongly Absorb Visible Light. *Physical Review Letters*, 100(6):066408, February 2008.

[84] Hyeri Lee, Siddharth Karkare, Luca Cultrera, Andrew Kim, and Ivan V. Bazarov. Review and demonstration of ultra-low-emittance photocathode measurements. *Review of Scientific Instruments*, 86(7):073309, July 2015.

[85] Hyeri Lee, Xianghong Liu, Luca Cultrera, Bruce Dunham, Vaclav O. Kostroun, and Ivan V. Bazarov. A cryogenically cooled high voltage DC photoemission electron source. *Review of Scientific Instruments*, 89(8):083303, August 2018.

[86] Derun Li, Hanqi Feng, Daniele Filippetto, Matthew Johnson, Andrew Lambert, Tianhuan Luo, Chad Mitchell, Ji Qiang, Fernando Sannibale, John Staples, Steve Virostek, and Russell Wells. Recent Progress on the Design of Normal Conducting APEX-II VHF CW Electron Gun. *Proceedings of the 10th Int. Particle Accelerator Conf.*, IPAC2019:4 pages, 0.928 MB, 2019. Artwork Size: 4 pages, 0.928 MB ISBN: 9783954502080 Medium: PDF Publisher: JACoW Publishing, Geneva, Switzerland.

[87] R. K. Li, H. To, G. Andonian, J. Feng, A. Polyakov, C. M. Scoby, K. Thompson, W. Wan, H. A. Padmore, and P. Musumeci. Surface-Plasmon Resonance-Enhanced Multiphoton Emission of High-Brightness Electron Beams from a Nanostructured Copper Cathode. *Physical Review Letters*, 110(7):074801, February 2013.

[88] M. Ligges, I. Rajkovic, P. Zhou, O. Posth, C. Hassel, G. Dumpich, and D. von der Linde. Observation of ultrafast lattice heating using time resolved electron diffraction. *Appl. Phys. Lett.*, 94(10):101910, March 2009.

[89] Zhi Liu, Yun Sun, P. Pianetta, and R. F. W. Pease. Narrow cone emission from negative electron affinity photocathodes. 23(6):2758.

[90] Roark A. Marsh, Michael A. Shapiro, Richard J. Temkin, Valery A. Dolgashev, Lisa L. Laurent, James R. Lewandowski, A. Dian Yeremian, and Sami G. Tantawi. X -band photonic band-gap accelerator structure breakdown experiment. *Phys. Rev. ST Accel. Beams*, 14(2):021301, February 2011.

[91] Nicola Marzari, Arash A. Mostofi, Jonathan R. Yates, Ivo Souza, and David Vanderbilt. Maximally localized Wannier functions: Theory and applications. *Reviews of Modern Physics*, 84(4):1419–1475, October 2012. arXiv: 1112.5411.

[92] Nicola Marzari and David Vanderbilt. Maximally-localized generalized Wannier functions for composite energy bands. *Physical Review B*, 56(20):12847–12865, November 1997. arXiv: cond-mat/9707145.

[93] J M Maxson, I V Bazarov, W Wan, H A Padmore, and C E Coleman-Smith. Fundamental photoemission brightness limit from disorder induced heating. *New Journal of Physics*, 15(10):103024, October 2013.

[94] Jared Maxson, David Cesar, Giacomo Calmasini, Alexander Ody, Pietro Musumeci, and David Alesini. Direct Measurement of Sub-10 fs Relativistic Electron Beams with Ultralow Emittance. *Physical Review Letters*, 118(15), April 2017.

[95] A. H. McEuen, P. Lui, E. Tanabe, and V. Vaguine. High-Power Operation of Accelerator Structures at Liquid Nitrogen Temperature. *IEEE Transactions on Nuclear Science*, 32(5):2972–2974, October 1985. Conference Name: IEEE Transactions on Nuclear Science.

[96] M.T. Menzel and H.K. Stokes. User's Guide for the POISSON/SUPERFISH Group of Codes. Technical Report L.A–UR–87–115, Los Alamos National Lab, New Mexico, January 1987.

[97] Herbert B Michaelson. The work function of the elements and its periodicity. *J. Appl. Phys.*, 48(11):6, 1977.

[98] P Michelato, C Pagan, D Sertorea, A di Bonab, and S Valerib. Characterization of Cs2Te photoemissive film: formation, spectral responses and pollution. *Nuclear Instruments and Methods in Physics Research A*, 393:5, 1997.

[99] P Michelato, C Pagani, F Sabary, D Sertore, and S Valeri. Formation of the Cs2Te Photocathode: Auger and Photoemission Spectroscopy Study. In *Proceedings of EPAC 1996*, page 3, Barcelona, June 1996. JACOW Publishing.

[100] V Miltchev and J W Baehr. Measurements of Thermal Emittance for Cesium Telluride Photocathodes at PITZ. In *Proceedings of the 27th International Free Electron Laser Conference*, page 4, 2005.

[101] D. Murphy, R. E. Scholten, and B. M. Sparkes. Increasing the Brightness of Cold Ion Beams by Suppressing Disorder-Induced Heating with Rydberg Blockade. *Phys. Rev. Lett.*, 115(21):214802, November 2015.

[102] P. Musumeci, L. Cultrera, M. Ferrario, D. Filippetto, G. Gatti, M. S. Gutierrez, J. T. Moody, N. Moore, J. B. Rosenzweig, C. M. Scoby, G. Travish, and C. Vicario. Multiphoton Photoemission from a Copper Cathode Illuminated by Ultrashort Laser Pulses in an rf Photoinjector. *Physical Review Letters*, 104(8):084801, February 2010.

[103] P. Musumeci, J. Giner Navarro, J.B. Rosenzweig, L. Cultrera, I. Bazarov, J. Maxson, S. Karkare, and H. Padmore. Advances in bright electron sources. *Nuclear Instruments and Methods in Physics Research Section A: Accelerators, Spectrometers, Detectors and Associated Equipment*, 907:209–220, November 2018.

[104] P Musumeci, M S Gutierrez, J T Moody, and C M Scoby. Time Resolved Relativistic Electron Diffraction. In *Proceedings of PAC09*, page 3, Vancouver, BC, Canada, 2009. JACOW Publishing.

[105] J. Kevin Nangoi, Siddharth Karkare, Ravishankar Sundararaman, Howard A. Padmore, and T. A. Arias. Ab initio many-body photoemission theory of transverse energy distribution of photoelectrons: PbTe(111) as a case study with experimental comparisons. *arXiv:2006.11924 [cond-mat, physics:physics]*, June 2020. arXiv: 2006.11924.

[106] Johannes Kevin Nangoi, Siddharth Karkare, Howard Padmore, and Tomas Arias. The important role of electron-phonon scattering in photoemission from PbTe(111). page R29.003.

[107] E.A. Nanni, W.S. Graves, and D.E. Moncton. Nanomodulated electron beams via electron diffraction and emittance exchange for coherent x-ray generation. *Physical Review Accelerators and Beams*, 21(1):014401, January 2018.

[108] R. B. Neal. The Stanford two mile accelerator. Technical Report SLAC-REPRINT-1968-001, Stanford Linear Accelerator Center, Menlo Park, CA (US), January 1968.

[109] M. Niemeyer, J. Ohlmann, A. W. Walker, P. Kleinschmidt, R. Lang, T. Hannappel, F. Dimroth, and D. Lackner. Minority carrier diffusion length, lifetime and mobility in p-type GaAs and GaInAs. 122(11):115702.

[110] Fernando Nogueira. Bayesian Optimization: Open source constrained global optimization tool for Python, 2014.

[111] K. Nordlund and F. Djurabekova. Defect model for the dependence of breakdown rate on external electric fields. *Phys. Rev. ST Accel. Beams*, 15(7):071002, July 2012.

[112] D. A. Orlov, M. Hoppe, U. Weigel, D. Schwalm, A. S. Terekhov, and A. Wolf. Energy distributions of electrons emitted from GaAs(cs, o). 78(18):2721–2723.

[113] Edward D. Palik. *Handbook of Optical Constants of Solids*. Academic Press.

[114] E Panofski, A Jankowiak, T Kamps, G Kourkafas, and S Eisebitt. MULTI-OBJECTIVE OPTIMIZATION OF AN SRF PHOTOINJECTOR FOR ERL AND UED APPLICATION. In *Proceedings of IPAC2017*, page 4, Copenhagen, Denmark, 2017.

[115] E Panofski, A Jankowiak, T Kamps, and A Neumann. Multi-Objective Optimization of an SRF Photoinjector with Booster Section for High Brightness Beam Performance. In *9th International Particle Accelerator Conference*, page 4, Vancouver, BC, Canada, 2018. JACOW Publishing.

[116] H. Panuganti and P. Piot. Observation of two-photon photoemission from cesium telluride photocathodes excited by a near-infrared laser. *Applied Physics Letters*, 110(9):093505, February 2017.

[117] C F Papadopoulos, J N Corlett, D Filippetto, J Qiang, F Sannibale, J W Staples, M Venturini, and M S Zolotorev. Multiobjective Optimization for the Advanced Photoinjector Experiment (APEX). In *Proceedings of FEL2010*, page 4, Malmo, Sweden, 2010. JACOW Publishing.

[118] S. Pastuszka, D. Kratzmann, D. Schwalm, A. Wolf, and A. S. Terekhov. Transverse energy spread of photoelectrons emitted from GaAs pho-

tocathodes with negative electron affinity. *Applied Physics Letters*, 71(20):2967–2969, November 1997.

[119] John P. Perdew, Kieron Burke, and Matthias Ernzerhof. Generalized Gradient Approximation Made Simple. *Physical Review Letters*, 77(18):3865–3868, October 1996.

[120] C M Pierce, I V Bazarov, L Cultrera, and J M Maxson. Measuring the Mean Transverse Energy of Pump-Probe Photoemitted Electrons. In *Proceedings of NAPAC2019*, page 4, Lansing, MI, USA, 2019. JACOW Publishing.

[121] Christopher M. Pierce, Matthew B. Andorf, Edmond Lu, Colwyn Gulliford, Ivan V. Bazarov, Jared M. Maxson, Matthew Gordon, Young-Kee Kim, Nora P. Norvell, Bruce M. Dunham, and Tor O. Raubenheimer. Low intrinsic emittance in modern photoinjector brightness. *Physical Review Accelerators and Beams*, 23(7):070101, July 2020. Publisher: American Physical Society.

[122] Christopher M. Pierce, Jai Kwan Bae, Alice Galdi, Luca Cultrera, Ivan Bazarov, and Jared Maxson. Beam brightness from Cs–Te near the photoemission threshold. *Applied Physics Letters*, 118(12):124101, March 2021. Publisher: American Institute of Physics.

[123] Christopher M. Pierce, Daniel B. Durham, Fabrizio Riminucci, Scott Dhuey, Ivan Bazarov, Jared Maxson, Andrew M. Minor, and Daniele Filippetto. Experimental characterization of photoemission from plasmonic nanogroove arrays, October 2022. arXiv:2210.05056 [physics].

[124] F. Le Pimpec, F. Ardana-Lamas, C. P. Hauri, and C. Milne. Quantum efficiency of technical metal photocathodes under laser irradiation of various wavelength. *Applied Physics A*, 112(3):647–661, September 2013. arXiv: 1202.0152.

[125] Igor Pinayev, Vladimir N. Litvinenko, Joseph Tuozzolo, Jean Clifford Brutus, Sergey Belomestnykh, Chase Boulware, Charles Folz, David Gassner, Terry Grimm, Yue Hao, James Jamilkowski, Yichao Jing, Dmitry Kayran, George Mahler, Michael Mapes, Toby Miller, Geetha Narayan, Brian Sheehy, Triveni Rao, John Skaritka, Kevin Smith, Louis Snydstrup, Yatming Than, Erdong Wang, Gang Wang, Binping Xiao, Tianmu Xin, Alexander Zaltsman, Z. Altinbas, Ilan Ben-Zvi, Anthony Curcio, Anthony Di Lieto, Wuzheng Meng, Michiko Minty, Paul Orfin, Jonathan Reich, Thomas Roser, Loralie A. Smart, Victor Soria, Charles Theisen, Wencan Xu, Yuan H. Wu, and Zhi Zhao. High-gradient High-charge CW

Superconducting RF gun with CsK2Sb photocathode. *arXiv:1511.05595 [physics]*, November 2015. arXiv: 1511.05595.

[126] A. Polyakov, S. Cabrini, S. Dhuey, B. Harteneck, P. J. Schuck, and H. A. Padmore. Plasmonic light trapping in nanostructured metal surfaces. *Applied Physics Letters*, 98(20):203104, May 2011.

[127] A. Polyakov, C. Senft, K. F. Thompson, J. Feng, S. Cabrini, P. J. Schuck, H. A. Padmore, S. J. Peppernick, and W. P. Hess. Plasmon-Enhanced Photocathode for High Brightness and High Repetition Rate X-Ray Sources. *Physical Review Letters*, 110(7):076802, February 2013.

[128] Aleksandr Polyakov. *Plasmon Enhanced Photoemission*. PhD thesis, UC Berkeley, Berkeley, CA, USA, May 2012.

[129] Aleksandr Polyakov, Howard A. Padmore, Xiaogan Liang, Scott Dhuey, Bruce Harteneck, James P. Schuck, and Stefano Cabrini. Light trapping in plasmonic nanocavities on metal surfaces. *Journal of Vacuum Science & Technology B, Nanotechnology and Microelectronics: Materials, Processing, Measurement, and Phenomena*, 29(6):06FF01, November 2011.

[130] Gisela Poplau, Ursula van Rienen, Marieke de Loos, and Bas van der Geer. Fast Calculation of Space Charge in Beam Line Tracking by Multigrid Techniques. In Hans-Georg Bock, Frank de Hoog, Avner Friedman, Arvind Gupta, William Langford, Helmut Neunzert, William R. Pulleyblank, Torgeir Rusten, Fadil Santosa, Anna-Karin Tornberg, Wilhelmus H. A. Schilders, E. Jan W. ter Maten, and Stephan H. M. J. Houben, editors, *Scientific Computing in Electrical Engineering*, volume 4, pages 329–336. Springer Berlin Heidelberg, Berlin, Heidelberg, 2004.

[131] R. A. Powell, W. E. Spicer, G. B. Fisher, and P. Gregory. Photoemission Studies of Cesium Telluride. *Physical Review B*, 8(8):3987–3995, October 1973.

[132] E Prat and S Bettoni. Thermal Emittance Measurements at the SwissFEL Injector Test Facility. In *Proceedings of FEL2014*, page 6, 2014.

[133] H J Qian, D Filippetto, and F Sannibale. S-Band Photoinjector Investigations by Multiobjective Genetic Optimizer. In *Proceedings of IPAC2016*, page 4, Busan, Korea, 2016. JACOW Publishing.

[134] X. Qiu, K. Batchelor, I. Ben-Zvi, and X-J. Wang. Demonstration of Emit-

tance Compensation through the Measurement of the Slice Emittance of a 10-ps Electron Bunch. *Phys. Rev. Lett.*, 76(20):3723–3726, May 1996.

[135] Omer Rahman, Jyoti Biswas, Mengjia Gaowei, Wei Liu, and Erdong Wang. New Activation Techniques for Higher Charge Lifetime from GaAs Photocathodes. *Proceedings of the 10th Int. Particle Accelerator Conf.*, IPAC2019:3 pages, 3.147 MB, 2019. Artwork Size: 3 pages, 3.147 MB ISBN: 9783954502080 Medium: PDF Publisher: JACoW Publishing, Geneva, Switzerland.

[136] Martin Reiser. *Theory and Design of Charged Particle Beams*.

[137] C. W. Roberson, Y. Y. Lau, and H. P. Freund. Emittance, Brightness, Free-Electron Laser Beam Quality, and the Scaled Thermal Velocity. In Anthony K. Hyder, M. Franklin Rose, and Arthur H. Guenther, editors, *High-Brightness Accelerators*, volume 178, pages 627–645. Springer US, Boston, MA, 1988.

[138] J. B. Rosenzweig, A. Cahill, V. Dolgashev, C. Emma, A. Fukasawa, R. Li, C. Limborg, J. Maxson, P. Musumeci, A. Nause, R. Pakter, R. Pompili, R. Roussel, B. Spataro, and S. Tantawi. Next generation high brightness electron beams from ultrahigh field cryogenic rf photocathode sources. *Phys. Rev. Accel. Beams*, 22(2):023403, February 2019.

[139] J.B. Rosenzweig, A. Cahill, B. Carlsten, G. Castorina, M. Croia, C. Emma, A. Fukusawa, B. Spataro, D. Alesini, V. Dolgashev, M. Ferrario, G. Lawler, R. Li, C. Limborg, J. Maxson, P. Musumeci, R. Pompili, S. Tantawi, and O. Williams. Ultra-high brightness electron beams from very-high field cryogenic radiofrequency photocathode sources. *Nuclear Instruments and Methods in Physics Research Section A: Accelerators, Spectrometers, Detectors and Associated Equipment*, 909:224–228, November 2018.

[140] J. G. Ruch and G. S. Kino. Transport properties of GaAs. 174(3):921–931.

[141] G. Rudolph. Convergence of evolutionary algorithms in general search spaces. In *Proceedings of IEEE International Conference on Evolutionary Computation*, pages 50–54, Nagoya, Japan, 1996. IEEE.

[142] I Schewe-Miller, H Borrmann, and A Simon. Synthesis and crystal structures of K5Se3, Cs5Te3 and Cs2Te. *Zeitschrift fur anorganische und allgemeine Chemie*, page 24, November 1991.

[143] Volker Schweikhard, Andrej Grubisic, Thomas A. Baker, and David J. Nesbitt. Multiphoton Scanning Photoionization Imaging Microscopy for Single-Particle Studies of Plasmonic Metal Nanostructures. *The Journal of Physical Chemistry C*, 115(1):83–91, January 2011.

[144] H. A. Schwettman, J. P. Turneaure, W. M. Fairbank, T. I. Smith, M. S. McAshan, P. B. Wilson, and E. E. Chambers. Low Temperature Aspects of a Cryogenic Accelerator. *IEEE Transactions on Nuclear Science*, 14(3):336–344, June 1967. Conference Name: IEEE Transactions on Nuclear Science.

[145] Germán Sciaini and R J Dwayne Miller. Femtosecond electron diffraction: heralding the era of atomically resolved dynamics. *Reports on Progress in Physics*, 74(9):096101, September 2011.

[146] Samuel Seely. Work Function and Temperature. *Physical Review*, 59(1):75–78, January 1941.

[147] Luca Serafini and James B Rosenzweig. Envelope analysis of intense relativistic quasilaminar beams in rf photoinjectors: A theory of emittance compensation. *Phys. Rev. E*, 55(6):26, 1997.

[148] D Sertore, D Favia, P Michelato, L Monaco, and P Pierini. Cesium Telluride and Metals Photoelectron Thermal Emittance Measurements Using a Time-of-flight Spectrometer. In *Proceedings of EPAC 2004*, page 3, Switzerland, 2004. JACOW Publishing.

[149] Georgii Shamuilov, Alan Mak, Kevin Pepitone, and Vitaliy Goryashko. Child-Langmuir law for photoinjectors. *Appl. Phys. Lett.*, 113(20):204103, November 2018.

[150] Bradley J. Siwick, Jason R. Dwyer, Robert E. Jordan, and R.J.Dwayne Miller. Femtosecond electron diffraction studies of strongly driven structural phase transitions. *Chem. Phys.*, 299(2):285–305, April 2004.

[151] William E. Spicer and Alberto Herrera-Gomez. Modern theory and applications of photocathodes. page 18, San Diego, CA, October 1993.

[152] Mark J. Stern, Laurent P. René de Cotret, Martin R. Otto, Robert P. Chatelain, Jean-Philippe Boisvert, Mark Sutton, and Bradley J. Siwick. Mapping momentum-dependent electron-phonon coupling and nonequilibrium phonon dynamics with ultrafast electron diffuse scattering. *Phys. Rev. B*, 97(16):165416, April 2018.

[153] Ravishankar Sundararaman, Kendra Letchworth-Weaver, Kathleen A. Schwarz, Deniz Gunceler, Yalcin Ozhabes, and T.A. Arias. JDFTx: Software for joint density-functional theory. *SoftwareX*, 6:278–284, 2017.

[154] E. Taft and L. Apker. Photoemission from Cesium and Rubidium Tellurides. *Journal of the Optical Society of America*, 43(2):81, February 1953.

[155] LCLS-II Project Team. LCLS-II Final Design Report. Technical Report LCLSII-1.1-DR-0251-R0, SLAC, September 2015.

[156] Heiko Trautner. *Spectral Response of Cesium Telluride and Rubidium Telluride Photocathodes for the Production of Highly Charged Electron Bunches*. PhD thesis, CERN, Geneva, March 2000.

[157] S. B. van der Geer, M. P. Reijnders, M. J. de Loos, E. J. D. Vredenbregt, P. H. A. Mutsaers, and O. J. Luiten. Simulated performance of an ultracold ion source. *Journal of Applied Physics*, 102(9):094312, November 2007.

[158] S.B. van der Geer and M.J. de Loos. Applications of the General Particle Tracer code. In *Proceedings of the 1997 Particle Accelerator Conference (Cat. No.97CH36167)*, volume 2, pages 2577–2579 vol.2, May 1997. ISSN: null.

[159] G. Vergara, A. Herrera-Gómez, and W. E. Spicer. Electron transverse energy distribution in GaAs negative electron affinity cathodes: Calculations compared to experiments. 80(3):1809–1815.

[160] Nicolas Vogel, Julius Zieleniecki, and Ingo Köper. As flat as it gets: ultrasmooth surfaces from template-stripping procedures. *Nanoscale*, 4(13):3820, 2012.

[161] X. J. Wang, M. Babzien, K. Batchelor, I. Ben-Zvi, R. I. Malone, X. Pogorelski, X. Qui, J. Sheehan, J. Sharitka, and T. Srinivasan-Rao. Experimental Characterization of High-Brightness Electron Photoinjector. New York, New York, 1995.

[162] Mark Warren, Adam Denchfield, Wei Gai, Noah Samuelson, Jiahang Shao, Linda Spentzouris, Eric Wisniewski, Zikri Yusof, and John Zasadzinski. Development of Hybrid Superconducting Photocathodes on Niobium Using High QE Coatings. *Proceedings of the 18th Int. Conf. on RF Superconductivity*, SRF2017:5 pages, 1.526 MB, 2018. Artwork Size: 5 pages, 1.526 MB ISBN: 9783954501915 Medium: PDF Publisher: JACoW, Geneva, Switzerland.

[163] S. P. Weathersby, G. Brown, M. Centurion, T. F. Chase, R. Coffee, J. Corbett, J. P. Eichner, J. C. Frisch, A. R. Fry, M. Gühr, N. Hartmann, C. Hast, R. Hettel, R. K. Jobe, E. N. Jongewaard, J. R. Lewandowski, R. K. Li, A. M. Lindenberg, I. Makasyuk, J. E. May, D. McCormick, M. N. Nguyen, A. H. Reid, X. Shen, K. Sokolowski-Tinten, T. Vecchione, S. L. Vetter, J. Wu, J. Yang, H. A. Dürr, and X. J. Wang. Mega-electron-volt ultrafast electron diffraction at SLAC National Accelerator Laboratory. *Review of Scientific Instruments*, 86(7):073702, July 2015.

[164] Eric Wisniewski, Sergey Antipov, Manoel Conde, Darrell Doran, Wei Gai, Chunguang Jing, Wanming Liu, John Power, and Charles Whiteford. Cs2Te Photocathode Performance in the AWA High-charge High-gradient Drive Gun. *Proceedings of the 6th Int. Particle Accelerator Conf.*, IPAC2015:3 pages, 0.397 MB, 2015. Artwork Size: 3 pages, 0.397 MB ISBN: 9783954501687 Medium: PDF Publisher: JACoW, Geneva, Switzerland.

[165] R Xiang, A Arnold, P Michel, P Murcek, and J Teichert. Thermal Emittance Measurement of the Cs2Te Photocathode in FZD Superconducting RF Gun. Technical report, EuCARD, October 2010.

[166] Naoto Yamamoto, Masahiro Yamamoto, Makoto Kuwahara, Ryosuke Sakai, Takanori Morino, Kuniaki Tamagaki, Atsushi Mano, Akira Utsu, Shouji Okumi, Tsutomu Nakanishi, Masao Kuriki, Chen Bo, Toru Ujihara, and Yoshikazu Takeda. Thermal emittance measurements for electron beams produced from bulk and superlattice negative electron affinity photocathodes. 102(2):024904.

[167] Jinfeng Yang, Koichi Kan, Nobuyasu Naruse, Yoichi Yoshida, Katsumi Tanimura, and Junji Urakawa. 100-femtosecond MeV electron source for ultrafast electron diffraction. *Radiation Physics and Chemistry*, 78(12):1106–1111, December 2009.

[168] Zikri Yusof, Adam Denchfield, Mark Warren, Javier Cardenas, Noah Samuelson, Linda Spentzouris, John Power, and John Zasadzinski. Photocathode quantum efficiency of ultrathin Cs 2 Te layers on Nb substrates. *Physical Review Accelerators and Beams*, 20(12):123401, December 2017.

[169] F. Zhou, J.C. Sheppard, T. Vecchione, E. Jongewaard, A. Brachmann, J. Corbett, S. Gilevich, and S. Weathersby. Establishing reliable good initial quantum efficiency and in-situ laser cleaning for the copper cathodes in the RF gun. *Nuclear Instruments and Methods in Physics Research Section A: Accelerators, Spectrometers, Detectors and Associated Equipment*, 783:51–57, May 2015.

[170] Feng Zhou, Axel Brachmann, Paul Emma, Sasha Gilevich, and Zhirong Huang. Impact of the spatial laser distribution on photocathode gun operation. *Physical Review Special Topics - Accelerators and Beams*, 15(9):090701, September 2012.

[171] Pengfei Zhu, J. Cao, Y. Zhu, J. Geck, Y. Hidaka, S. Pjerov, T. Ritschel, H. Berger, Y. Shen, R. Tobey, J. P. Hill, and X. J. Wang. Dynamic separation of electron excitation and lattice heating during the photoinduced melting of the periodic lattice distortion in 2H-TaSe2. *Appl. Phys. Lett.*, 103(7):071914, August 2013.

[172] Pengfei Zhu, Y Zhu, Y Hidaka, L Wu, J Cao, H Berger, J Geck, R Kraus, S Pjerov, Y Shen, R I Tobey, J P Hill, and X J Wang. Femtosecond time-resolved MeV electron diffraction. *New Journal of Physics*, 17(6):063004, June 2015.

[173] Eckart Zitzler, Marco Laumanns, and Lothar Thiele. SPEA2: Improving the Strength Pareto Evolutionary Algorithm. Technical Report TIK-Report 103, ETH Library, Zurich, 2001.